



**Optical Fibre Surface Plasmon Resonance
Sensors Based on a Metallic Array of
Sub-wavelength Apertures**

Huy Huynh Nguyen

A thesis submitted for the degree of

Doctor of Philosophy

Faculty of Health, Engineering and Science

Victoria University, Melbourne Australia

2012

Declaration

‘I, Huy Huynh Nguyen, declare that the PhD thesis entitled

“Optical fibre surface plasmon resonance sensors based on a metallic array of sub-wavelength apertures”

is no more than 100,000 words in length including quotes and exclusive of tables, figures, appendices, bibliography, references and footnotes. This thesis contains no material that has been submitted previously, in whole or in part, for the award of any other academic degree or diploma. Except where otherwise indicated, this thesis is my own work’.

.....

Huy Huynh Nguyen

Dated the 12th day of March, 2012

Acknowledgements

I would like to thank our Almighty God for everything.

I would like to thank my supervisor Professor Greg Baxter, who has given me unreserved support throughout my research with his patience, guidance and knowledge. The outcome of this research will never be possible without his encouragement and the freedom in research that he gave to me.

I am very grateful to Professor Stephen Collins for his guidance throughout this research and particularly during the process of writing this thesis. He was patient with questions and always available to answer them in a professional manner. His help and guidance are greatly appreciated.

I would like to thank Associate Professor Ann Roberts for many constructive discussions. I offer my gratitude to Dr. Fotios Sidiroglou for helping me in the laboratory with equipment preparations and troubleshooting any unforeseen problems that occurred during the experiments. I am grateful to Dr Ling Lin for spending time in the fabrication laboratory helping me with the fabrication and training me how to use the different equipment. The experimental process would have taken longer without her help.

I am thankful to Dr. Kumaravelu Ganesan and Dr. Sergey Rubanov for their help in the fabrication process. I am thankful to the Staff and Students at the Centre for Telecommunications and Microelectronics of Victoria University, in particular Dr. Think Nguyen, Dr. Nicoleta Dragomir, Julie Olsson, Shukonya Benka, Donald Ermel, Mohammadreza Pourakbar and many others.

I am very thankful to my mother-in-law, Mrs. Le Minh Nguyet who has passed away a few years ago. Her constant love and support will never be forgotten.

I am very thankful to my family, my parents, Mr. Huynh Nguyen and Mrs. Hien Nguyen, my sisters, Heather and Rachel, my brother-in-law, Adam, my nephews, Luke & Dean for their love, support and encouragement throughout my research.

I would like to dedicate this work to my wife, Kim Chi, and my daughter, Elizabeth. Without their constant love, support and understanding I would not have had the strength to finish this work.

Abstract

In this dissertation, optical fibre surface plasmon resonance sensors based on a metallic array of sub-wavelength apertures are investigated. Metallic sub-wavelength apertures may be designed to support surface plasmon resonances that are sensitive to the surrounding environment when embedded at the end-face of an optical fibre. Factors contributing to the liquid refractive index sensitivity are explored systematically through simulation, theory, and experiment. The optical fibre sensor (OFS) is a novel sensing device based on surface plasmon resonance technology and metallic nanostructure materials. The sensitivity of the sensor can be tailored by designing a suitable periodic array of sub-wavelength apertures. In the sensing mechanism, liquids such as water, acetone and iso-propyl alcohol were used to test the sensing surface of the optical fibre end-face. The identification of different refractive indices can be achieved by measuring the wavelength difference variations of spectral features and the light intensity from the reflection spectra of the OFS. The proposed sensor is compact in size and suitable for remote sensing. The sensor needs only a small volume of the liquid being tested and it is easy to use. It is evident that experimental results are in good agreement with theoretical results. However, the result of this study determined that it is unlikely that an OFS based on a periodic metallic nanostructure at the fibre end-face will produce a sensor with superior sensitivity to variations in liquid refractive index (RI) as compared to cheaper existing technologies.

List of Tables

Table 3.1 (a) and (b): Documented performance parameters of various optical fibre refractive index sensors. Note that $\Delta\lambda/\Delta n \Leftrightarrow$ nm/RIU and $\Delta n \Leftrightarrow$ RIU.	33
Table 4.1: A summary of typical characteristic of single apertures reported. Au \equiv gold, Ag \equiv silver, PEC \equiv perfect electrical conductor.	53
Table 4.2: A summary of currently investigated array of sub-wavelength apertures.....	54
Table 6.1: The difference in reflection spectra when the medium surrounding the single mode fibre end-face was changed from air to water, acetone and IPA.	82
Table 7.1: Metallic sub-wavelength apertures investigated in this thesis and their performance with respect to sensor sensitivity for an RI range 1.33 - 1.38.....	108
Table 7.2: Metallic sub-wavelength apertures investigated in this thesis and their performance with respect to sensor sensitivity for an RI range 1.33 - 1.47.....	109

List of Figures

Figure 1.1: The surface charge and electromagnetic field of the SPPs propagating on a surface in the x direction [3].	2
Figure 1.2: A commercial SPR sensing system from BIAcore Inc. [4].	2
Figure 1.3: Illustration of an array of sub-wavelength apertures embedded on the fibre end-face, which is integrated by analysis of reflected light.	3
Figure 2.1: Schematic of the key elements of an optical fibre.	7
Figure 2.2: Schematic of the propagation of light in an optical fibre launched into the core.	8
Figure 2.3: Schematic of the (a) refracting or leaky rays and (b) bound or guided rays in an optical fibre waveguide.	8
Figure 2.4: Illustration of the evanescent wave formed when light undergoes total internal reflection, showing the variation of the electric field with distance from the interface.	9
Figure 2.5: Schematic showing the general design scheme of (a) intrinsic and (b) extrinsic optical fibre sensors.	11
Figure 3.1: Data curves plotted for real metals (Au, Ag, and Cu) for their (a) refractive index n , (b) absorption constant K , (c) real, and (d) imaginary part of permittivity ϵ [79].	19
Figure 3.2: Geometry of a single interface between a metal and a dielectric for surface plasmon propagation.	20
Figure 3.3: Dispersion relation of SPs at interface between the dielectric ϵ_d and metal ϵ_m [2].	22
Figure 3.4: Schematic diagram of SPs propagating on a surface defined by the x - y plane at $z = 0$ along the x direction at (a) high and (b) low frequencies. Exponentially decaying electric field as a function of z shown in the x - z coordinate for both low and high frequencies, where $z > 0$ is inside the dielectric and $z < 0$ is inside the metal.	24
Figure 3.5: Kretschmann SPR configuration.	25
Figure 3.6: Reflectivity for a light wave exciting a surface plasmon in the geometry versus wavelength for two different refractive indices of the dielectric (angle of incidence is 54°)	

[83]. Note that $\Delta\lambda_r$ = change in reflectivity wavelength; ΔI_r = change in reflectivity intensity; n_D = refractive index of dielectric.	26
Figure 3.7: General SPR optical fibre sensors include (a) D-shape fibre, (b) cladding-off fibre, (c) end-reflection mirror, (d) angled fibre tip, and (e) tapered fibre [95].....	28
Figure 3.8: Various SPR optical fibre configurations. (a) long period grating (LPG), (b), fibre Bragg grating (FBG), (c) LPG pair, (d) tilted grating, (e) metal surface grating, and (f) side-polished fibre [95,96].....	29
Figure 3.9: Diagram showing fibre SPR sensors working in the transmission mode (a) and reflection mode (b) [5].	30
Figure 4.1: Schematic diagrams of (a) the excitation of the surface plasmon by the incident photon on a metallic grating surface and (b) the dispersion curves of the incident photon and the surface plasmon.....	37
Figure 4.2: 2D grating with incident photon having wave-vector k_l	38
Figure 4.3: Schematic diagram of: (a) a 5×5 array of nanoholes; (b) transmission mechanism in a sub-wavelength nanohole array: (1) excitation of surface plasmon by the incident photon on the front surface, (2) resonant coupling of surface plasmons of the front and back surfaces, (3) re-emission of photon from surface plasmon on the back surface.	40
Figure 4.4: (a) Schematic of the surface current I_s and accumulated charges along edge of the hole induced by normally incident plane wave. (b) The equivalent magnetic dipole of the hole. (c) The equivalent electric dipole of the hole.	42
Figure 4.5: Geometry of optical scattering by a hole in a real screen in (a) real space and (b) k-space for a range that k_x is close to zero [129].	44
Figure 4.6: Composite diffractive evanescent wave lateral field profile at the $z=0$ boundary, a plot of Equation (4.13) [152].	45
Figure 4.7: Schematic diagram showing: (a) a periodic corrugation around a single hole aperture; (b) the CDEW for an aperture with periodic corrugations on the input and output surfaces. Red arrows indicate the CDEWs generated on the input and output surfaces.	46
Figure 4.8: Schematic diagram of: (a) a 5 by 5 array of circular sub-wavelength apertures; (b) a CDEW for a periodic array of sub-wavelength apertures. Red arrows indicate the CDEWs generated on the input and output surfaces.....	47

Figure 4.9: Schematic diagrams showing Fano profile analysis. (a) formal representation of the Fano model for coupled channels and (b) physical properties of the scattering process through the nanohole array directly (straight arrows) or via SP excitation [133].	49
Figure 4.10: Schematic diagram of the non-resonant transmission (Bethe's contribution) and the resonant transmission (surface plasmon contribution) [156].	49
Figure 4.11: (a) Zero-order transmission spectrum of an Ag array. The lattice spacing a_0 was 900 nm, the nanoholes diameter was 150 nm and the thickness was 200nm. (b) Spectra for two identical Ag arrays with different thicknesses (Solid line: $t = 200$ nm; dashed line: $t = 500$ nm); for both arrays: period (a_0) = 0.6 μm ; diameter (d) = 150 nm. Images were taken from [8].	51
Figure 4.12: Distribution of electric field intensity around various apertures: (a) square, (b) rectangular, (c) L-shaped, (d) bowtie-shaped, (e) C-shaped, (f) I-shaped, (g) triangular, (h) annular, and (i) cross-shaped. Figures (a)-(f) were taken from [170] and (g) was taken from [160].	52
Figure 5.1: Function $f(x)$ at discrete points.	57
Figure 5.2: Positions of the electric and magnetic field vector components on a cubic unit cell of the Yee space lattice.	59
Figure 5.3: (a) An illustration of an incident plane wave travelling through an optical fibre to a flat gold film layer, and (b) the equivalent simulation set-up.	62
Figure 5.4: FDTD calculations of (a) transmission and (b) reflection of a flat (180 nm) thin gold film on an optical fibre end-face.	63
Figure 5.5: Comsol (FEM) calculations of (a) transmission and (b) reflection of a flat (180 nm) thin gold film on a optical fibre end-face.	63
Figure 5.6: Measured (a) transmission and (b) reflection of a layer (180 nm) thin gold film on multimode fibre end-face.	64
Figure 6.1: Schematic of the setup employed for evaluation of the spectrum of the array of nanoholes in a transmission-based configuration which included a sensor chamber (A), a liquid injection system (B), a sensing fibre (C), and a collecting fibre (D)[13].	66
Figure 6.2: An interpretation of a unit cell used in FDTD Solutions.	67

Figure 6.3: Screen shot from the FDTD Solutions of a unit cell of an array of circular nanoholes with periodicity of 600 nm in a 180 nm thick gold layer. The four individual frames depicted in the screen shot show (left to right, top to bottom), XY plane, Perspective view, XZ plane and XY plane.68

Figure 6.4: Measured transmission spectra of a 24 by 24 circular nanohole array in a gold film on the end-face of a multimode optical fibre, having a 100 μm core. The thickness of the gold film was 180 nm. The diameter of each nanohole was 200 nm. The spacing (periodicity) between the nanoholes was (a) 400 and (b) 600 nm. Graphs were taken from [13].69

Figure 6.5: FDTD simulated transmission spectra of a 24 by 24 circular nanohole array in a gold film on the end-face of a multimode optical fibre, having a 100 μm core. The thickness of the gold film was 180 nm. The diameter of the nanohole was 200 nm. The periodicity between the nanoholes was (a) 400 and (b) 600 nm.70

Figure 6.6: A reflection-based OFS experimental setup for determining RI.....71

Figure 6.7: (a) The cross-shaped structure simulated in FDTD; (b) The intensity of the electric field around the cross-shaped: the cross-shaped is centered at the origin and the film boundaries are outlined in dashed lines.72

Figure 6.8: Screen shot from the FDTD Solutions of a unit cell of an array of cross-shape apertures with periodicity, width and length of 400, 20 and 300 nm, respectively, in a 140 nm thick gold layer. The four individual frames depicted in the screen shot show (left to right, top to bottom), XY plane, Perspective view, XZ plane and YZ plane.73

Figure 6.9: Schematic illustration of a special optical fibre holder with (a), (c), (d) are the side, bottom, 3D views and (b) dimension of a fibre retainer.....74

Figure 6.10: (a) A Thermionics VE-180 e-beam/thermal vacuum evaporator [206], and (b) Schematic diagram of an evaporation process.....75

Figure 6.11: A QCad graphic software layout design - The black and white colour scheme of a 5 \times 5 cross-shaped array structure. The layout is scaled to the desired dimensions within the FIB milling software.76

Figure 6.12: xT FEI Nova Dualbeam FIB and SEM system [207].76

Figure 6.13: Schematic illustration of a dual-beam FIB-SEM instrument. Expanded view shows the electron and ion beam sample interaction [208]77

Figure 6.14: A special fibre holder mounted to a FIB vacuum chamber where a double sided tape (black band) is being used.....	78
Figure 6.15: A fabrication process of a cross-shaped apertures array on the end-face of a single mode fibre.....	78
Figure 6.16: (a) an SEM image of a 30×30 array of cross-apertures milled on the gold-coated end-face of the fibre; (b) a zoom-in image of the array; (c) actual fabrication dimensions of the cross-shaped apertures.....	79
Figure 6.17: FDTD simulated (---) and experimental (—) reflection spectra of the OFS when the medium surrounding the fibre end-face was air. The cross-shaped array parameters were: $h = 300$ nm, $w = 20$ nm, $P = 400$, and $T = 140$ nm.....	80
Figure 6.18: FDTD simulated (---) and experimental (—) reflection spectra of the OFS when the fibre end-face was immersed into water. The cross-shaped array parameters were: $h = 300$ nm, $w = 20$ nm, $P = 400$, and $T = 140$ nm.	80
Figure 6.19: FDTD simulated (---) and experimental (—) reflection spectra of the OFS when the fibre end-face was immersed into acetone. The cross-shaped array parameters were: $h = 300$ nm, $w = 20$ nm, $P = 400$, and $T = 140$ nm.	81
Figure 6.20: FDTD simulated (---) and experimental (—) reflection spectra of the OFS when the fibre end-face was immersed into isopropyl-alcohol (IPA). The cross-shaped array parameters were: $h = 300$ nm, $w = 20$ nm, $P = 400$, and $T = 140$ nm.	81
Figure 6.21: A plot of the measured SPR dip wavelengths versus the index of refraction of various liquids. The results of a linear fit are shown.	83
Figure 6.22: A plot of the FDTD simulated SPR dip wavelengths versus the index of refraction of various liquids. A Linear relationship between the minimum reflected wavelengths and the refractive indices is obtained with the indicated parameters.....	83
Figure 6.23: FDTD simulated (---) and experimental (—) reflection spectra of the SPR OFS by assuming that the water was not inside the apertures. The cross-shaped array parameters were: $h = 300$ nm, $w = 20$ nm, $P = 400$, and $T = 140$ nm.....	84
Figure 6.24: FDTD simulated (---) and experimental (—) reflection spectra of the SPR OFS by assuming that the acetone was not inside the apertures. The cross-shaped array parameters were: $h = 300$ nm, $w = 20$ nm, $P = 400$, and $T = 140$ nm.....	85

Figure 6.25: FDTD simulated (---) and experimental (—) reflection spectra of the SPR OFS by assuming that the isopropyl-alcohol (IPA) was not inside the apertures. The cross-shaped array parameters were: $h = 300$ nm, $w = 20$ nm, $P = 400$, and $T = 140$ nm.85

Figure 6.26: A plot of the FDTD simulated SPR dip wavelengths versus the index of refraction of various liquids which were not presented inside the apertures. A linear relationship between the minimum reflected wavelengths and the refractive indices is obtained with the indicated parameters.....86

Figure 7.1: A 15×15 gold array of sub-wavelength circular apertures.....88

Figure 7.2: (a) A unit cell of the fibre end-face sensor simulated in FDTD; (b) The intensity of the electric field ($|E|^2$) around the nanohole: the nanohole is centered at the origin and the film boundaries are outlined in dashed lines.....88

Figure 7.3: FDTD calculations of the reflectance intensity through a circular nanohole array with (a) the gold film thickness, T , varying from 140 to 220 nm while P and D remained at 500 and 300 nm, respectively; (b) the nanohole diameter, D , varying from 220 to 320 nm while P and T remained at 500 and 140 nm, respectively.89

Figure 7.4: FDTD calculations of the reflectance intensity through a circular nanohole array with the periodicity, P , varying from 440 to 520 nm while D and T remained at 300 and 140 nm, respectively.90

Figure 7.5: FDTD calculations of the reflected power spectra for the fibre sensor (circular apertures) in various liquids with the gold film thickness $T = 140$ nm, periodicity $P = 500$ nm and hole diameter $D = 300$ nm.....91

Figure 7.6: Dependence of SPR dip wavelength on the index of refraction of various liquids, showing the linear fit. The circular parameters: $T = 140$ nm, $P = 500$ nm and $D = 300$ nm..91

Figure 7.7: An illustration of a 15×15 cross-shaped array with a zoom-in 5×5 array.....92

Figure 7.8: A unit cell representation for cross-shaped apertures for simulation purposes.....92

Figure 7.9: FDTD calculations of the reflectance intensity through a cross-shaped array with (a) the length, h varying from 100 to 300 nm while w , T and P were kept constant at 20, 140 and 500 nm, respectively; (b) the width, w varying from 10 to 50 nm while h , T and P were kept constant at 300, 140 and 500 nm, respectively.93

Figure 7.10: Geometry of a 5 by 5 array of cross-shaped apertures used in analysis of the reflection profiles. The analysis considers a normally incident plane wave with either TE or TM polarization.	94
Figure 7.11: TE-polarization - (a) Electric field intensity versus position [x, y], (b) Electric field intensity versus position [y, z].	94
Figure 7.12: TM-polarization - (a) Electric field intensity versus position [x, y], (b) Electric field intensity versus position [y, z].	95
Figure 7.13: FDTD calculations of the reflectance intensity through a cross-shaped array with (a) the thickness, T varying from 140 to 220 nm while w, h and P were kept constant at 20, 300 and 500 nm, respectively; (b) the periodicity, P varying from 400 to 540 nm while w, h, and T were kept constant at 20, 300 and 140 nm, respectively.	96
Figure 7.14: FDTD calculations of the reflected power spectra for the fibre sensor in various liquids with the gold film thickness T = 140 nm, periodicity P = 400 nm, length h = 300 nm and width w = 20 nm	96
Figure 7.15: Dependence of SPR dip wavelength on the index of refraction of various liquids, showing the linear fit. The cross-shaped parameters: T = 140 nm, P = 400 nm, h = 300 nm and w = 20 nm.	97
Figure 7.16: (a) An illustration of the dimensioning system used in a cross-shaped array with rounded corners on the end-face of a single mode fibre, (b) A unit cell representation for the simulation purposes.	98
Figure 7.17: FDTD calculations of the reflected power spectra for the fibre sensor in various liquids of the rounded corners cross-shaped structure with T = 140 nm, periodicity P = 400 nm, length h = 300 nm and width w = 20 nm.	99
Figure 7.18: Dependence of SPR dip wavelength on the index of refraction of various liquids, showing the linear fit. The rounded corners cross-shaped parameters: T = 140 nm, P = 400 nm, h = 300 nm and w = 20 nm	99
Figure 7.19: (a) An illustration of the dimensioning system used in an array of annular apertures on the end-face of a single mode fibre, (b) A unit cell representation for the simulation purposes.	100
Figure 7.20: FDTD calculations of the reflectance intensity through an annular array with (a) the inner diameter, D_{in} , varying from 40 to 160 nm while P, D_{out} and T remained at 500, 200	

and 100 nm, respectively; (b) the outer diameter, D_{out} , varying from 200 nm to 320 nm while P , T and D_{in} remained at 500, 100 and 80 nm, respectively. 101

Figure 7.21: FDTD calculations of the reflectance intensity through an annular array with (a) the periodicity, P , varying from 350 to 600 nm while D_{in} , D_{out} and T remained at 80, 200 and 100 nm, respectively; (b) the thickness, T , varying from 100 to 220 nm while P , D_{out} and D_{in} remained at 500, 200 and 80 nm, respectively..... 102

Figure 7.22: FDTD calculations of the reflected power spectra for the fibre sensor in various liquids with the gold film thickness $T = 100$ nm, periodicity $P = 500$ nm, inner diameter $D_{in} = 100$ nm and outer diameter $D_{out} = 200$ nm..... 102

Figure 7.23: Dependence of SPR dip wavelength on the index of refraction of various liquids, showing the linear fit. The annular parameters: $T = 100$ nm, periodicity $P = 500$ nm, inner diameter $D_{in} = 100$ nm and outer diameter $D_{out} = 200$ nm..... 103

Figure 7.24: FDTD calculations of the reflected power spectra for the fibre sensor in various liquids with the following annular array parameters: $T = 100$ nm, $P = 500$ nm, $D_{in} = 120$ nm and $D_{out} = 200$ nm. 104

Figure 7.25: Dependence of SPR dip wavelength on the index of refraction of various liquids, showing the linear fit. The annular array parameters: $T = 100$ nm, $P = 500$ nm, $D_{in} = 120$ nm and $D_{out} = 200$ nm. 104

Figure 7.26: (a) An illustration of the geometry used in an array of rectangular apertures on the end-face of a single mode fibre, (b) A unit cell representation for simulation purposes. 105

Figure 7.27: FDTD calculations of the reflectance intensity through a cross-shaped array with the width, w varying from 10 to 60 nm while h , T and P were kept constant at 300, 140 and 500 nm, respectively. 105

Figure 7.28: FDTD calculations of the reflected power spectra for the fibre sensor in various liquids with the rectangular array parameters: $T = 140$ nm, $P = 400$ nm, $h = 300$ nm and $w = 20$ nm. 106

Figure 7.29: Dependence of SPR dip wavelength on the index of refraction of various liquids, showing the linear fit. The rectangular array parameters: $T = 140$ nm, $P = 400$ nm, $h = 300$ nm and $w = 20$ nm. 107

List of Symbols and Abbreviations

Units of Measure:

μm : micrometer

nm : nanometer

Mathematical Symbols:

\hat{i} : Unit vector in the x -direction in a Cartesian coordinate system

\hat{j} : Unit vector in the y -direction in a Cartesian coordinate system

Physical Constants:

c : Speed of light in a vacuum

\hbar : Planck's constant

e : Charge on an electron

μ_0 : Vacuum permeability, or permeability of free space

ϵ_0 : Vacuum permittivity, or permittivity of free space

m : Electron mass

Physical Symbols:

\mathbf{x} : Position vector

\mathbf{E} : Electric field

$|\mathbf{E}|^2$: Electric field intensity

$|\mathbf{E}_{\text{total}}|^2$: Total electric field intensity

$|\mathbf{E}_{\text{incident}}|^2$: Incident electric field intensity

\mathbf{H} : Magnetic field

μ : Permeability

ϵ : Permittivity (or dielectric constant)

ϵ_d : Dielectric constant of a dielectric material

ϵ_m : Dielectric constant of a metal

ϵ_p : Dielectric constant of a prism (glass)

ω : Angular frequency

\mathbf{k} : Wave-vector

\mathbf{k}_0 : Wave-vector of incident light

K : Absorption constant

λ : Wavelength

λ_0 : Wavelength of incident light

θ_a : Acceptance angle

θ_c : Critical angle

d_p : Penetration depth of the evanescent field

n : refractive index

N : Conduction electron density

ω_p : Plasma frequency

Γ_p : Collision frequency

τ : Average collision time of free electrons

δ : Skin depth

δ_1 : Skin depth in dielectric

δ_1 : Skin depth in metal

σ_s : Surface charge density

V : Coupling term

Chemical Symbols:

Ag: Silver (ω dependent)

Au: Gold (ω dependent)

Refractive index (25 °C) of common materials

Acetone: $n= 1.36$

Air: $n= 1.00$

Glass: $n= 1.50$

Iso-propyl alcohol: $n= 1.38$

Water: $n= 1.33$

Abbreviations:

2D: 2-dimensional

3D: 3-dimensional

FIB: Focused ion beam

CAD: Computer-aided design

CDEW: Composite diffractive evanescent wave

EM: Electromagnetic

EOT: Extraordinary optical transmission

FDTD: Finite-difference time-domain method

FBG: Fibre Bragg grating

FEM: Finite-element method

IPA: Iso-propyl alcohol

LPG: Long period grating

LSP: Localized surface plasmon

LSPP: Localized surface plasmon polariton

OFS: Optical fibre sensor

PDE: Partial differential equation

PEC: Perfect electric conductor

PML: Perfect matched layers

RF: Radio frequency

RI: Refractive index

RIU: Refractive index unit

SEM: Scanning electron microscope

SERS: Surface-enhanced Raman scattering

SNR: Signal to noise ratio

SP: Surface plasmon

SPP: Surface plasmon polariton

SPR: Surface plasmon resonance

TE: Transverse electric

TIR: Total internal reflection

TM: Transverse magnetic

Table of Contents

Declaration.....	ii
Acknowledgements	iii
Abstract.....	iv
List of Tables	v
List of Figures.....	vi
List of Symbols and Abbreviations	xiv
List of Publications	xxi
Chapter 1. Introduction	1
1.1. Motivation	1
1.2. Contributions to knowledge	4
1.3. Outline of this thesis	5
Chapter 2. Optical Fibre Sensors	7
2.1. Optical fibre wave guide principles	7
2.2. Optical fibres as sensors.....	10
2.2.1. Intrinsic sensors	11
2.2.2. Extrinsic sensors	12
2.2.3. Optical fibre sensing.....	12
2.2.3.1. Refractive index sensor	12
2.2.3.2. Microbend fibre optic sensors.....	13
2.2.3.3. Surface enhanced Raman scattering (SERS) fibre sensor.....	14
2.2.3.4. Surface Plasmon Resonance (SPR) fibre sensor.....	14
Chapter 3. Surface Plasmon Resonance (SPR) and SPR-Based Optical Fibre Sensors .	16
3.1. SPR theory and optical properties of metals	16
3.2. Properties of SPPs	19
3.2.1. Dispersion relation of surface plasmons on a smooth metal surface..	19
3.2.2. Propagation length and skin-depth of SPs on a smooth surface.....	22
3.3. Surface plasmons excitation by light	24
3.3.1. Prism configuration	24
3.3.2. Excitation of SPR in an optical fibre	27
Chapter 4. Metallic Sub-wavelength Apertures.....	35
4.1. Introduction	35

4.2. Surface plasmon excitation on a periodic array of sub-wavelength apertures.	36
4.3. Mechanism of transmission via surface plasmon coupling in a periodic nanohole array	39
4.4. Localized surface plasmon polaritons (LSPPs)	40
4.4.1. LSPPs of metallic nanoholes	41
4.5. Composite diffractive evanescent wave (CDEW)	42
4.5.1. The principle of the CDEW	43
4.5.2. The CDEW for an aperture with a periodic corrugation	46
4.5.3. The CDEW for an array of sub-wavelength apertures	47
4.6. Fano profile analysis	48
4.7. Fabry-Perot resonance on periodic arrays of sub-wavelength apertures	49
4.8. Types of metallic sub-wavelength apertures	50
Chapter 5. Numerical Modeling Techniques	55
5.1. Introduction	55
5.2. Finite-difference time-domain (FDTD)	55
5.2.1. Finite difference approximation	56
5.2.2. The Yee cell	58
5.2.3. Lumerical FDTD solutions	60
5.3. Finite element method (FEM)	60
5.3.1. Comsol Multiphysics	61
5.4. Lumerical FDTD solution TM versus Comsol Multiphysics TM	61
Chapter 6. Fabrication and Experimental Techniques	65
6.1. Introduction	65
6.2. Transmission-based configuration	65
6.2.1. Analytical solution	66
6.2.2. FDTD simulation	66
6.2.3. Experimental and simulation results comparison	69
6.3. Reflection-based configuration	70
6.3.1. Simulation	71
6.3.2. Fabrication	73
6.3.3. Experimental and simulation results comparison	79
6.3.4. Surface tension between liquids and sub-wavelength apertures	84
Chapter 7. Simulations, Comparison and Discussion	87

7.1. Introduction	87
7.2. Reflection spectra from an array of circular apertures (nanoholes)	87
7.3. Reflection spectra from an array of cross-shaped apertures	92
7.4. Reflection spectra from an array of cross-shaped apertures with rounded corners	98
7.5. Reflection spectra from an array of annular apertures	100
7.6. Reflection spectra from an array of rectangular apertures	104
Chapter 8. Conclusion and Outlook.....	111
Appendix A	113
Appendix B	114
Bibliography	115

List of Publications

The body of original research presented in this thesis has been published, in part, in the following:

1. Nguyen H, Sidiroglou F, Collins S F, Baxter G W, Roberts A and Davis T J, 2012, "Periodic array of nanoholes on gold-coated optical fiber end-faces for surface plasmon resonance liquid refractive index sensing", 3rd Asia Pacific Optical Sensors Conference, Sydney Australia, Proc. SPIE 8351, 835128 (6pp).
2. Nguyen H, Baxter G W, Collins S F and Roberts A, 2010, "Metallic nanostructures on optical fibre end-faces for refractive index sensing", 35th Australian Conference on Optical Fibre Technology (CD-ROM: 19th Australian Institute of Physics Congress, Australian Institute of Physics, Australian Optical Society & Engineers Australia, ISBN 978-0-9775657-6-4), paper no. 694.
3. Nguyen H, Milicevic M, Roberts A, Baxter G W, Collins S F and Davis T J, 2009, "Towards a refractive index sensor utilizing nanostructures surface plasmon resonance on the endface of an optical fibre", Proceedings of the Australasian Conference on Optics, Lasers and Spectroscopy and 34th Australian Conference on Optical Fibre Technology in association with the International Workshop on Dissipative Solitons 2009 (ACOFT ACOLS 09), Australian Optical Society & Engineers Australia (ISBN 1 876346 61 2), ACOFT paper 20, pp. 475-476.
4. Roberts A, Lin L, Goh X-M, Milicevic M, Nguyen H and Baxter G W, 2009, "Noughts and crosses: Resonances in nanometric apertures and hole arrays", 7th Asia-Pacific conference on Near-Field Optics. pp. 41.
5. Milicevic M, Roberts A, Lin L, Nguyen H and Baxter G W, 2009, "Angular dependence of localised surface plasmon modes", 7th Asia-Pacific conference on Near-Field Optics. pp. 161.

Chapter 1. Introduction

1.1. Motivation

During the last decades, the continuing need for faster and improved means of detection, communication, and data processing has encouraged rapid growth in the field of all-optical components. This has led to the development of a variety of new sensing optical devices able to detect, measure, and process data using electromagnetic radiation. In addition, materials technology and fabrication methods, particularly for semiconductors, have advanced, allowing devices to be built with fine structural details. In combination, these developments have brought technology to a point that new applications can be envisaged, where all-optical sensing components and circuits are replacing conventional mechanical and electrical sensors.

The motivation behind research and development activities in optical sensing relies on the expectation that properties of the optical sensing field are significantly advantageous over conventional sensing. Some of the advantages of optical over non-optical sensors are enhanced sensitivity, wide dynamic range, electrical passivity, insensitivity to electromagnetic interference, small size, and multiplexing capabilities [1]. In this context, surface plasmon resonance (SPR) based sensing possesses the majority of these advantages. Operation of these devices is based on the excitations of surface plasmons at a metal-sample interface [2]. Surface plasmons (SPs), also known as surface plasmon polaritons (SPPs) are surface modes that propagate at metal-dielectric interfaces and constitute an electromagnetic field coupled to oscillations of the conduction electrons at the metal surface as shown in Figure 1.1. The fields associated with the SPPs are enhanced at the surface and decay exponentially into the media on either side of the interface.

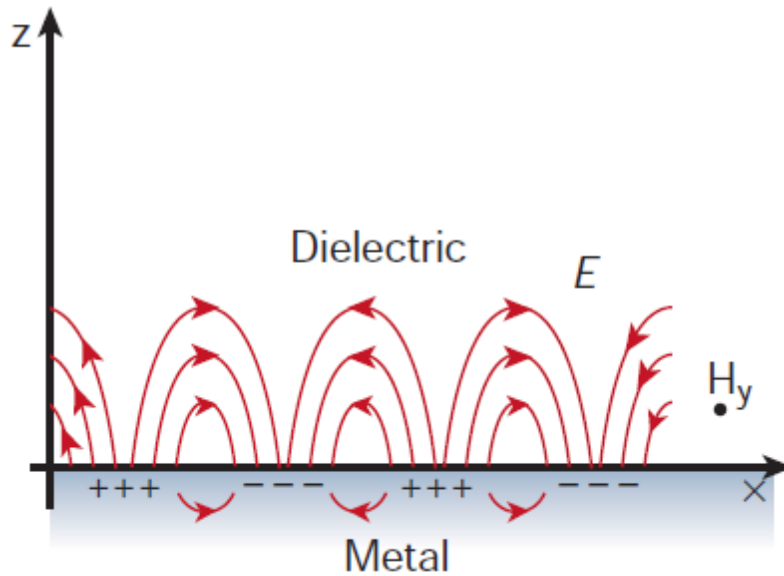


Figure 1.1: The surface charge and electromagnetic field of the SPPs propagating on a surface in the x direction [3].

The conventional excitation of surface plasmons using a prism requires a very sophisticated and bulky experimental setup, their large detection spot and the need of a coupling prism limits their effectiveness for probing nanovolumes and single cells. For example, a commercial SPR system from BIAcore [4] has a price of several hundred thousand US dollars, and weighs over 40 kg, and is shown in Figure 1.2.

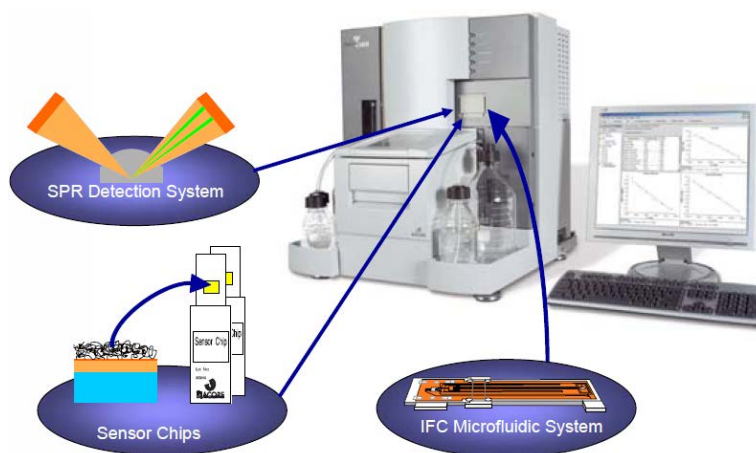


Figure 1.2: A commercial SPR sensing system from BIAcore Inc. [4].

Over the past few years, several types of optical fibre sensors based on the SPR effect have been proposed. Many researchers have used the core or end-face of an optical fibre in place of prism for the excitation of the surface plasmons [5-7].

In 1998, a group of researchers published the results of a crucial experimental on the transmission of light through sub-wavelength aperture arrays in thin metallic films [8]. Their experiment indicated that transmitted light through sub-wavelength aperture arrays at certain wavelengths had a much higher intensity than estimated by the classical theory [9]. Recently, due to the impressive progress in nano-fabrication technology [10] [11], many researchers have pursued this idea in a quest to create sensitive sensors by fabricating an array of nanostructures at the end-face of an optical fibre, for instance nanorods [12], nanoholes [13] and nanoparticles [14]. However, these early proposals offer preliminary designs with little theoretical or experimental evidence to show that the performance of optical fibre sensors would be enhanced by a metallic nanostructure.

The search for a thin film nanostructure that is situated at the optical fibre's end-face and possesses high refractive index (RI) sensitivity becomes a challenging task for design and fabrication technology and is the motivation behind this thesis. Due to the scope of the subject, this thesis investigates the effect of a periodic metallic sub-wavelength aperture array on the sensitivity of an SPR based OFS, including detailed simulations of light reflection and transmission from an array of sub-wavelength apertures. One of the advantages of inscribing an array of sub-wavelength apertures on a fibre end-face is that one can overcome the light focusing difficulty; i.e. a pre-focused plane wave can be directed to the metallic array. This offers the convenient approach of analyzing the wavelength properties of the reflected beam within the resonant reflection dip. Such, a reflection based sensor, which is considered to be simple, compact and useful for many applications, is presented in Figure 1.3.

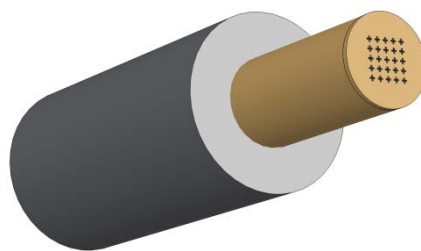


Figure 1.3: Illustration of an array of sub-wavelength apertures embedded on the fibre end-face, which is integrated by analysis of reflected light.

1.2. Contributions to knowledge

As outlined in the motivation section, the primary objective of this work was to explore the development of an optical fibre SPR sensor operating in reflection mode based on an array of sub-wavelength apertures embedded at the fibre's end-face hopefully demonstrating superior performance when compared to alternative techniques. The performance of the sensor in terms of its sensitivity to refractive index change was to be measured. In light of the objective of this research work, it is believed that the following contributions have been made:

The critical elements of the integration of metallic sub-wavelength apertures at the end-face of both single mode and multimode optical fibres were determined.

Design, fabrication, and optical characterization of gold sub-wavelength apertures deposited on the end-face of an optical fibre was achieved. Results obtained demonstrated the optical sensing capability of the device through the RI measurement of a known liquid.

A modeling and design methodology was developed to evaluate the influence of the critical metallic sub-wavelength aperture parameters of shape, size, and periodicity, on the optical properties of the metallic film when placed at the end-face of an optical fibre.

Details of the findings of a suitable numerical modeling technique show that there was excellent agreement between the experimental observation and the commercial software package Finite-Difference Time-Domain (FDTD) simulation.

A comparison of the sensitivity of various possibilities in using metallic sub-wavelength apertures (e.g. circular, rectangular, annular and cross-shaped) on the fibre end-faces was achieved.

When considering the experimental practicality of this sensor, an issue arose believed to be due to surface tension between the liquid and the metal. This caused a shift in the wavelength of the reflectance dip and may compromise the reliability of a developed sensor.

1.3. Outline of this thesis

This doctoral dissertation explores an exciting approach of integrating metallic sub-wavelength apertures with an optical fibre for sensing purposes. Specifically, this dissertation aims to exploit the multi-functionality of gold sub-wavelength apertures and nanostructures for liquid RI sensing based on surface plasmon and localized surface plasmon resonances.

This dissertation is structured as follows. A review of basic properties of an optical fibre with an emphasis on fibre sensing is presented in Chapter 2. In Chapter 3, an introduction to the SPR effect and available SPR techniques is given including information about SPR theory, the basic optical properties of metals and a review of the properties of propagating surface plasmon polaritons (SPPs) at a planar metal-dielectric interface by solving Maxwell's equations with the proper boundary conditions. In addition, the main techniques that are currently employed in the SPR field such as prism and fibre configurations are described and a review of the literature regarding available SPR fibre-based sensors is also presented.

In Chapter 4, the theory of surface plasmon excitation on periodic arrays of sub-wavelength apertures and the mechanism of transmission via surface plasmon coupling in a periodic apertures array are discussed. In addition, a brief overview of the composite diffractive evanescent wave method (CDEW), Fano and Fabry-Perot analysis is presented. In Chapter 5, the computational methods that are used to solve Maxwell's equations of electromagnetic are reviewed. Particular focus is on the finite-difference time-domain (FDTD) method and the finite-element method (FEM).

Chapter 6 discusses the fabrication, experiments and comparison with theory. Specific emphasis is placed on the sensor's sensitivity and a comparison between the measured and calculated transmission (and reflection) spectra of an array of gold sub-wavelength nanoholes (and cross-shaped) on a single mode fibre end-face. Chapter 7 presents in detail the simulations and comparison of an array of gold sub-wavelength apertures deposited on fibre end-faces with various aperture shapes and sizes.

Chapter 8 summarizes the study of optical fibre surface plasmon resonance sensors based on a metallic array of sub-wavelength apertures and comments on its application as a RI sensing platform.

Chapter 2. Optical Fibre Sensors

This chapter includes on the structure of optical fibres, light propagation principles, and the modification of the optical fibre structure to form different types of optical fibre sensors. This includes the evanescent mode, leaky mode and partial leaky mode sensing mechanisms based on the relative RI of the modified cladding and the core. This chapter also presents a brief review of optical fibre sensors with special emphasis on chemical sensors.

2.1. Optical fibre wave guide principles

An optical fibre is a cylindrical dielectric waveguide that transports energy at wavelengths in the visible and infrared portions of the electromagnetic spectrum, using the Total Internal Reflection (TIR) phenomenon occurring at the interface between two media with different refractive indices. Figure 2.1 is a schematic of the basic structure of an optical fibre. It consists of a cylindrical core, cladding, coating buffer, and outer jacket. A typical single mode fibre has a core diameter between 8 and 10 μm and a cladding diameter of 125 μm , whereas multimode fibres generally have large core diameters, e.g. 50 μm , 62.5 μm , or 100 μm .

Propagation of light in an optical fibre occurs through TIR, which is governed by the refractive indices of the core and cladding. The central core, in which light is guided, is embedded in an outer cladding which has a slightly lower RI. To form guided rays in the fibre, the ray should be incident on the core such that upon refraction into the core it makes an angle smaller than θ'_c with the fibre axis as shown in Figure 2.2, where θ_a is the acceptance angle and θ_c is the critical angle between the fibre core and cladding.

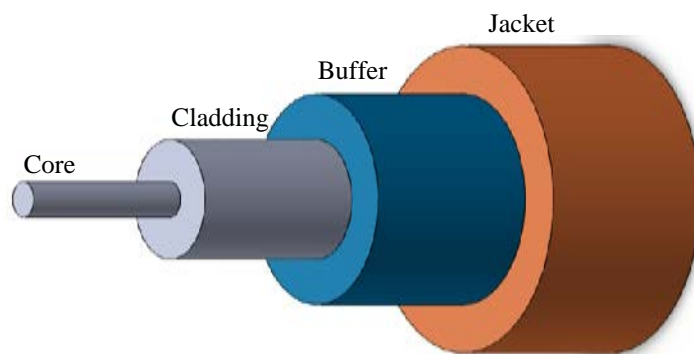


Figure 2.1: Schematic of the key elements of an optical fibre.

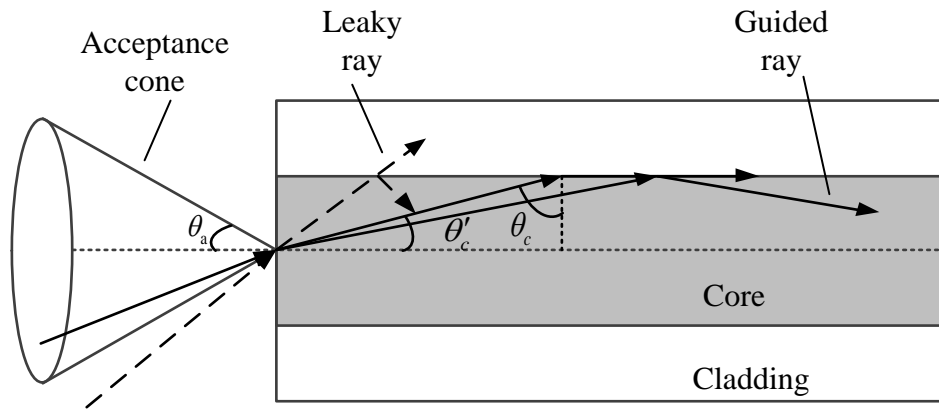


Figure 2.2: Schematic of the propagation of light in an optical fibre launched into the core.

The light ray incident outside of the acceptance cone loses part of its power to the cladding at each reflection and is not guided (a so-called “leaky” or “refracting” modes), as shown in Figure 2.3(a). For this refracting ray, a fraction of its power is lost and it attenuates as it propagates in the cladding.

If the path of a light ray is entirely confined within the core by TIR, this ray is referred to as a guided or bound ray, as shown in Figure 2.3(b). Since, a bound ray is contained completely within the core it can propagate indefinitely without loss of power in the absence of absorption and scattering losses in the core. These rays are categorized by a value of θ_z , according to the condition given below [15]:

$$\text{Bound or guided rays: } 0 \leq \theta_z \leq \theta_c,$$

$$\text{Refracting or leaky rays: } \theta_c \leq \theta_z \leq \pi/2.$$

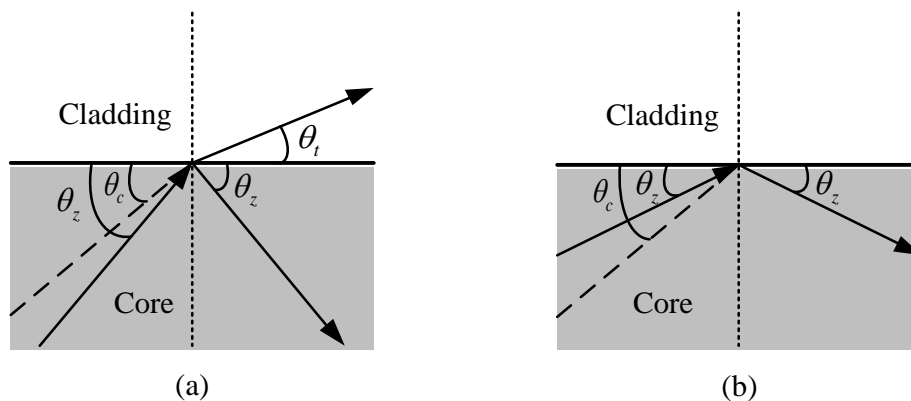


Figure 2.3: Schematic of the (a) refracting or leaky rays and (b) bound or guided rays in an optical fibre waveguide.

According to Maxwell's equations, when light undergoes total internal reflection, the electromagnetic field cannot be discontinuous at the boundary of two optical media. Consequently, a stationary wave is formed that extends into the cladding normal to the interface [16]. This is known as the evanescent wave, and the electric field strength decays exponentially away from the boundary as illustrated in Figure 2.4. The penetration depth of the evanescent field is given by:

$$d_p = \frac{\lambda_0}{2\pi \sqrt{(n_{core}^2 \sin^2 \theta - n_{cladding}^2)}},$$

where:

λ_0 : wavelength of light in free space

θ : angle of incident

n_{core} : refractive index of core

$n_{cladding}$: refractive index of cladding

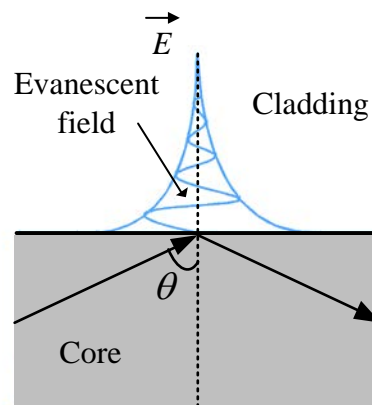


Figure 2.4: Illustration of the evanescent wave formed when light undergoes total internal reflection, showing the variation of the electric field with distance from the interface.

The evanescent field is part of the guided light that travels through a region that extends outward, ~ 100 nanometre, into the media surrounding the waveguide. When there is a

change in the optical characteristics of the outer medium (i.e. refractive index change), a modification in the optical properties of the guided wave (phase velocity) is induced via the evanescent field. Integrated optical sensors make use of the evanescent field detection principle extensively.

2.2. Optical fibres as sensors

In the modern world there is an ever increasing need to monitor environmental factors such as temperature, stress, humidity, the presence or concentration of a chemical or biological species.

Optical fibre sensing competes with other sensing technologies but it is attractive in applications due to:

1. Precision and sensitivity: because of the dielectric nature of glass, the OFS has high immunity to electromagnetic and radio frequency interference that affects the measurement accuracy and precision in most electrical sensors. An OFS is sensitive to small perturbations in its environment.
2. Remote sensing: it is possible to use a segment of the fibre as a sensor gauge with a long segment of another fibre (or the same fibre) conveying the sensing information to a remote station. Optical fibre transmission cables offer significantly lower signal loss, as compared to signal transmission in other sensors, and can maintain a high signal-to-noise ratio (SNR).
3. Distributed measurement: an optical fibre communication network allows the user to carry out measurements at different points along the transmission line without significant loss when the signal passes through it. This provides a method to monitor, control, and analyze the parameter being monitored over an extended length or area.
4. Operation in hazardous environments: optical fibre sensors have been proven to be able to work under extreme conditions, such as high temperature, high pressure, corrosive and toxic environments, high radiation, large electromagnetic fields and other harsh environments.
5. Compactness and flexibility: optical fibres are intrinsically small-size, which helps when building a compact measurement and acquisition system.

Furthermore they have been proven to be very adaptable because of their demonstrated ability to perform well in many types of measurement.

6. Easy transportation: optical fibres are very light weight; it is easy to transport them to remote locations.

With these advantages, optical fibre sensors have been employed to replace conventional sensors in some chemical sensing applications. They have also been used in experimental research as tools to provide accurate and stable measurements in the laboratory. The use of optical fibres to sense the chemical concentration of analytes has been reported in the literature since the 1960s. Optical fibre sensors have found applications in chemical [17-19], biochemical [20-23], biomedical and environmental [24-27] sensing. In general, optical fibre sensors are classified as intrinsic or extrinsic, as illustrated in Figure 2.5.

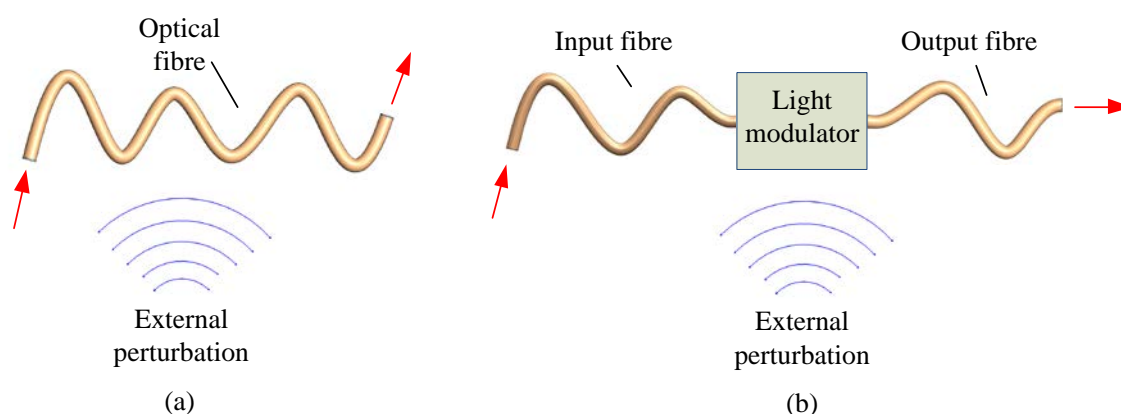


Figure 2.5: Schematic showing the general design scheme of (a) intrinsic and (b) extrinsic optical fibre sensors.

2.2.1. Intrinsic sensors

The intrinsic sensors operate on the principle that the sensing takes place within the fibre itself as shown in Figure 2.5(a). The propagating light never leaves the fibre and is altered in some way by an external phenomenon which can be tracked by changes in one or more features, i.e. intensity, phase, polarization, wavelength, etc. There are four general sensor designs for intrinsic optical fibre chemical sensors: fibre refractometer [28], evanescent-wave spectroscopic [29], active coating [30,31] and active core [32,33].

2.2.2. Extrinsic sensors

Extrinsic sensors are distinguished by the characteristic that the sensing takes place in a region outside the fibre as shown in Figure 2.5(b). The optical fibre is only used as the means of light delivery and collection. The propagating light leaves the fibre in a way that can be detected and collected back by another or the same fibre.

An optrode is a good example of an extrinsic OFS. The design consists of a source fibre and a receiver fibre connected to a third optical fibre by a special connector [34]. The end-face of the third fibre is coated with a sensitive material, e.g. applied by the dip coating procedure. The chemical to be sensed may interact with the sensitive end-face by changing the absorption, reflection, or scattering properties, or by changing the luminescence intensity, RI or polarization behaviour. The fibre in this case acts as a light pipe transporting light to and from the sensing region.

Another example of an extrinsic OFS is an optical fibre liquid level sensor that has been developed in recent years based on direct interaction between the light and liquid. The most common method in commercial products employs a prism attached to the ends of two single optical fibres [35].

In general, there are advantages and disadvantages to using either class of sensor. Extrinsic sensors are less sensitive, more easily multiplexed, and easier to use. However, they possess some connection problems (into and out of the light modulator), whereas, intrinsic sensors are more sensitive and therefore more difficult to shield from unwanted external disturbances [36].

2.2.3. Optical fibre sensing

2.2.3.1. Refractive index sensor

Various chemical substances as well as several different physical and biological parameters can be detected through the measurement of RI. This has motivated OFS researchers to put significant effort into developing optical fibre RI sensors. Optical fibre RI sensors have found applications in in-situ monitoring of chemical processes in harsh environments, as well as pollution monitoring in water supply and other public utilities. Many different RI related parameters and techniques such as interferometry

[37], fibre gratings [38-40], and specialty fibres [41-43] have been proposed as design elements for optical fibre RI sensors.

An interferometer-based RI sensor [37] consists of two beams; one beam is exposed to the external medium and thus serves as the sensing arm while the other beam is used as the reference. When these two arms are combined to generate an interference pattern, a change in the external RI alters the optical path length of the sensing arm and thus causes a shift in the interference pattern. These types of sensors require a mechanism to split the incoming light into two arms, with the advent of fibre optic couplers such systems have been greatly simplified and can result in a robust fibre optic sensor system.

Fibre Bragg grating (FBG) and long period grating (LPG) are commonly employed for RI measurement. RI changes are measured from the shifts of the transmission or reflection spectra due to the influence of the external RI on the coupling conditions of the fibre gratings. As an LPG sensor couples the light from the core mode to the cladding modes, its transmission spectrum is sensitive to changes of the external RI [38]. Compared to the LPG sensors, the FBG-based RI sensors are usually less sensitive. As a result, the cladding surrounding a FBG is usually etched or thinned in order to increase the sensitivity [39,40,44]. RI sensors based on fibre gratings can be expensive due to either the grating fabrication processes or the need for specialty fibres.

Specialty fibres such as D-shaped fibre [41,45], microstructured fibre [42], and cladding stripped fibre [43] have also been used for biochemical sensing. These types of optical fibre chemical sensors require accessing the evanescent field at the interface of the fibre core and the surrounding medium. Therefore, a precision micromachining is required to remove a part of the fibre cladding.

2.2.3.2. Microbend fibre optic sensors

Microbend fibre optic sensors operate on the principle of intensity loss through a curved section of an optical fibre [46-49]. The intensity loss changes when the fibre bend radius is changed making it possible to calibrate the applied force with the change in the transmitted intensity. Such intensity-modulation-based approaches are simple and inexpensive. A change in the bend radius by applied force, temperature, or any other parameter causes the transmitted laser intensity to change, which can be detected and

used in sensing. Existing applications of microbend sensors can be found in detection of stress, strain [50], cracks [49], pH in a solution [48], and chemical species [51]. Other reports of intensity modulation based sensors are found to be in measuring humidity [52,53], RI of a liquid [54], liquid level in a vessel [55], and noise in a combustion engine [56]. While this principle is simple and provides a robust sensor, the size of the sensor and complexities in maintaining close control over curvature still pose challenges.

2.2.3.3. Surface enhanced Raman scattering (SERS) fibre sensor

SERS is a form of Raman spectroscopy which involves the study of samples adsorbed to or interacting in some manner with metal surfaces. In the case of conventional Raman scattering, no metal particles are present and the target analyte interacts directly with the incident electromagnetic field. In surface enhanced Raman scattering the substrate is coated with metal colloids and the chemical to be examined is on the metal surface. This metal coating involves the creation of a surface plasmon on the substrate surface, which transfers energy through an electric field to the target molecules allowing otherwise inaccessible vibrational structures to be determined. The signal obtained is much enhanced in the case of SERS as compared to conventional Raman spectroscopy.

The effect of SERS has been exploited in an optical fibre for chemical sensing [57]. The sensor consists of a single optical fibre with its end-face coated with a thin layer of nanoparticles as a waveguide for the transmission of an excitation laser beam, resulting in a high quality SERS signal. A variety of fabrication techniques for optical fibre SERS sensors have been reported such as a long optical fibre made of side-polished and end-polished fibres [58], an angle-polishing technique of the fibre tip in which the signal can be enhanced by a factor of six [59], a unique optimized fibre tip geometry which helped to improve the sensor's detection limit [60,61] applied nanoimprint technology to copy nanostructures to the end-face of an optical fibre for SERS applications. Although the integration of SERS systems with optical fibre technology has been attracting many researchers it is still posing some issues with sensitivity and stability.

2.2.3.4. Surface Plasmon Resonance (SPR) fibre sensor

Over the past years, many fibre-based surface plasmon resonance (SPR) sensors were reported. For examples, SPR sensor configurations with multimode, single mode and

polarization maintaining fibres coated with a thin metallic layer have been proposed [62-65]. A surface plasmon resonance is an electromagnetic phenomenon which occurs when light is reflected off a thin metal film (e.g. Ag, Au) deposited on a substrate (e.g. glass, quartz, prism) when the angle of incidence is greater than the angle of total internal reflection (TIR). A fraction of this light energy interacts with the collective oscillation of free electrons in the metal film therefore reducing the reflected light intensity. SPR has been widely demonstrated to be an effective optical technique for many types of interface studies [66]. The unique physical properties of SPR have attracted a lot of attention in recent years in optical biosensing research communities. For instance, if analyte molecules bind to the immobilized target the local RI changes, leading to a change in SPR angle. This change can be monitored in real-time by detecting changes in the intensity of the reflected light.

Optical fibres provide an alternative to prism-based SPR sensors as discussed in Section 2.2. More details of the SPR phenomenon and fibre optic-based SPR sensors will be discussed in Chapter 3.

Chapter 3. Surface Plasmon Resonance (SPR) and SPR-Based Optical Fibre Sensors

In 1902, Wood observed narrow dark bands in the spectrum of the diffracted light that he referred to as anomalies, when he used a polychromatic light source to illuminate a metallic diffraction grating [67]. In 1941, Fano was the first to conclude that Wood's anomalies were related to the excitation of electromagnetic waves on the surface of the diffraction grating [68]. In 1959, Turbadar observed a large drop in the reflection intensity when illuminating thin metal films on a substrate but he did not relate this effect to surface plasmon resonance (SPR) [69]. It was the work of Otto [70,71], Kretschmann and Raether [72] in the late 1960s that brought understanding and showed the versatility of the SPR technique.

In the last two decades, SPR has advanced from a rather obscure physical phenomenon to an optical tool that is used extensively in physical, chemical and biological fields [62,73-76]. The main reason for SPR sensors to become a powerful tool for the characterization of biomolecules interaction is their capability for real-time monitoring and label-free sensing with high detection sensitivity and wide dynamic range. Recently, the field of SPR has been addressed using metallic sub-wavelength apertures (also called metallic nanostructures) which can be designed such that they can perform certain useful optical characteristics for a range of applications.

The objective of this chapter is to provide an introduction to the SPR effect and available SPR techniques. The first section includes information about SPR theory and the basic optical properties of metals. The second section reviews the properties of propagating surface plasmon polaritons (SPPs) or surface plasmons (SPs) at a planar metal-dielectric interface by solving Maxwell's equations with the proper boundary conditions. The last section describes the main techniques that are currently employed in the SPR field such as prism and fibre configurations. A literature review regarding available SPR fibre-based sensors is also presented.

3.1. SPR theory and optical properties of metals

SPR refers to the optical excitation of surface plasmons (SPs) at the interface between a metal (e.g. gold or silver) and a dielectric (e.g. gas, liquid or solid) [2]. A plasmon is a collection of electrons that collectively oscillate in a piece of conducting material. When electrons are

displaced, the positive charge exerts an attractive force on the electrons and tries to pull them back to their original positions. Such interactions make the plasmons oscillate once they are excited. The oscillation frequency of collective electrons in a volume metal is called the plasma frequency and is defined as [77]:

$$\omega_p = \sqrt{\frac{Ne^2}{\epsilon_0 m}} , \quad (3.1)$$

where N is the conduction electron density, e is the charge on the electron, m is the electron mass and ϵ_0 is the permittivity of free space.

Unlike bulk (or volume) plasmons, which oscillate through the metal volume, SPs are confined to the surface and interact strongly with light. Therefore, the SP field intensity at the metal/dielectric interface can be made very high, which is the main reason why SPR is such a powerful tool for many types of interface sensing studies.

Surface plasmons can be excited only along the interface between a metal and a dielectric, which is dependent upon the response of the metal interacting with the incident electromagnetic wave. Over a wide range of frequencies, the dielectric properties of metals are usually described by the model that was first proposed by Drude in 1900, which assumes the metal is a free electron gas [78]:

$$\epsilon(\omega) = 1 - \frac{\omega_p^2}{\omega^2 + i\Gamma_p \omega} . \quad (3.2)$$

where Γ_p is the collision frequency. Typical plasma frequencies, ω_p are equivalent to the frequencies of visible light (i.e $\sim 400 - 790$ THz). In the Drude model, interactions between electrons are not taken into account. The electrons oscillating in response to the applied electromagnetic field are damped via collisions with nuclei at a collision frequency $\Gamma_p = 1/\tau$, where τ is known as the average collision time of free electrons. At room temperature, the typical value of τ is in the order of 10^{-14} s, corresponding to $\Gamma_p \sim 10^{14}$ Hz. The real and imaginary parts of $\epsilon(\omega)$ can be expressed as [77]:

$$\epsilon_r = 1 - \frac{\omega_p^2}{(\omega^2 + \Gamma_p^2)} , \quad (3.3)$$

$$\varepsilon_i = \frac{\omega_p^2 \Gamma_p}{[\omega(\omega^2 + \Gamma_p^2)]} . \quad (3.4)$$

The frequencies discussed here are limited to $\omega < \omega_p$, where metals maintain their metallic characteristics. For high frequencies, i.e. $\omega \gg \Gamma_p$, which correspond to optical frequencies, damping can be ignored, and ε_r can be approximated as $1 - \omega_p^2/\omega^2$. Consequently, ε_r is negative and $\varepsilon_i \approx \Gamma_p \omega_p^2/\omega^3 \ll |\varepsilon_r|$. For low frequencies, i.e. $\omega \ll \Gamma_p$, such as in the terahertz regime, ε_r is still negative, whereas, $\varepsilon_i \gg |\varepsilon_r|$.

The complex refractive index of a metal can be defined as [77]:

$$n = \sqrt{\varepsilon} = n_r + in_i \quad (3.5)$$

where,

$$n_r = \left[\frac{1}{2} \left(\sqrt{\varepsilon_r^2 + \varepsilon_i^2} + \varepsilon_r \right) \right]^{\frac{1}{2}}, \quad (3.6)$$

$$n_i = \left[\frac{1}{2} \left(\sqrt{\varepsilon_r^2 + \varepsilon_i^2} - \varepsilon_r \right) \right]^{\frac{1}{2}}. \quad (3.7)$$

For $\omega < \omega_p$, n_i is larger than n_r , and the propagation of an electromagnetic wave in a metal is dominated by absorption, leading to rapidly exponential decay of electric field that could not penetrate through the metal. The distance through which the amplitude of an electromagnetic wave decreases by a factor of $1/e$, and is defined as the skin depth δ , which changes according to the frequency of applied electromagnetic waves.

In order to fully account for the interband transition in real metals, permittivity values obtained from direct measurements are preferred. Johnson and Christy in [79] obtained such data. From reflection and transmission measurements on vacuum-evaporated thin films, the authors obtained the refractive index n and the optical absorption constant K of noble metals such as gold, silver and copper for the visible and near-infrared portions of the electromagnetic spectrum. From the definitions of complex refractive index and permittivity and from Equation (3.5), thus,

$$n(\omega) = n + iK \quad (3.8)$$

$$\varepsilon(\omega) = \varepsilon'(\omega) + i\varepsilon''(\omega) = n^2 \quad (3.9)$$

the measured quantities can be readily translated into a complex permittivity via $\epsilon' = n^2 - K^2$ and $\epsilon'' = 2nK$. The permittivity for a range of wavelengths are plotted in Figure 3.1. The refractive index and the absorption constant are also shown.

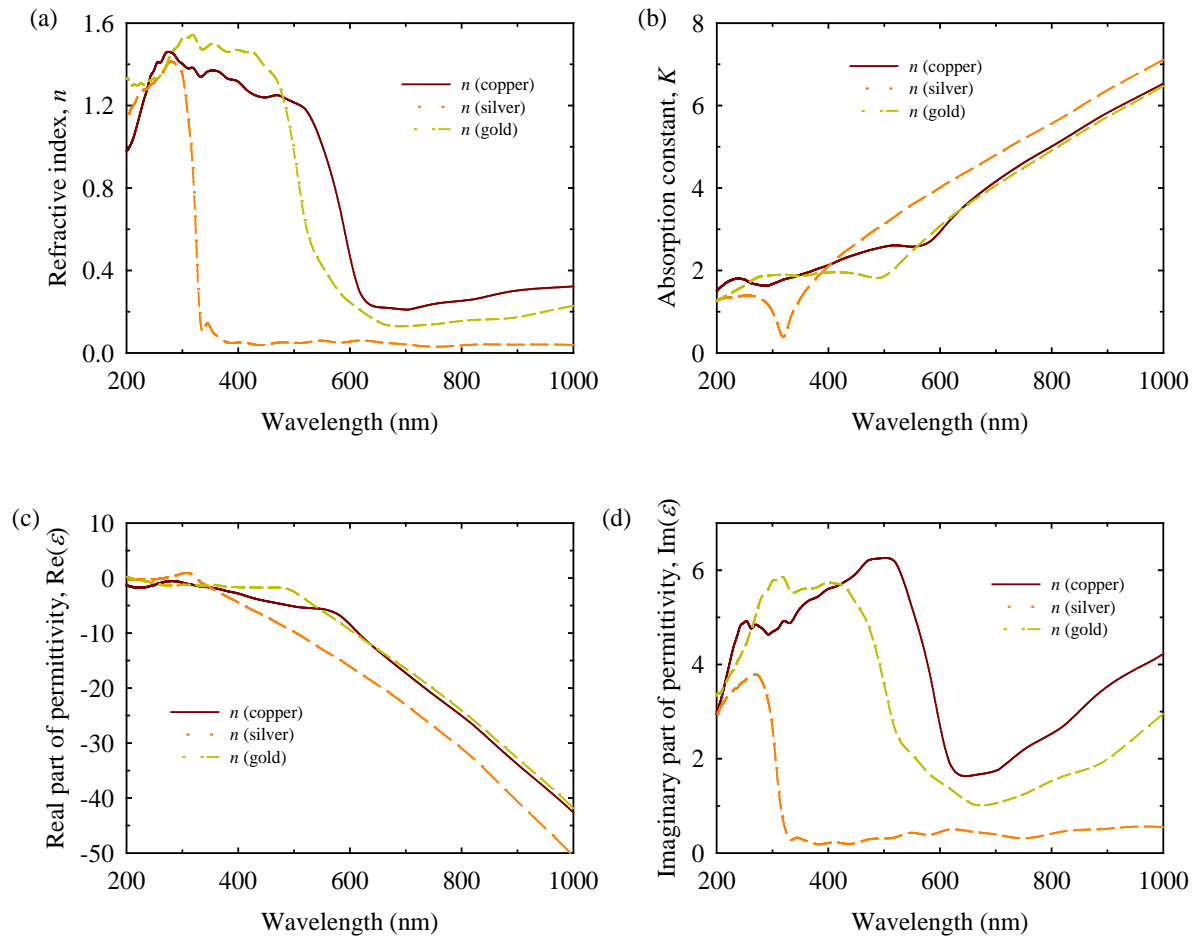


Figure 3.1: Data curves plotted for real metals (Au, Ag, and Cu) for their (a) refractive index n , (b) absorption constant K , (c) real, and (d) imaginary part of permittivity ϵ [79].

3.2. Properties of SPPs

3.2.1. Dispersion relation of surface plasmons on a smooth metal surface

Figure 3.2 shows a simple xy-plane geometry that sustains SPs in a single, flat interface between two half-infinite regions 1 and 2, which are composed of a dielectric, non-absorbing

half region ($z > 0$) with positive real dielectric constant $\epsilon_d(\omega)$ and an adjacent conducting half region ($z < 0$) described via a dielectric function $\epsilon_m(\omega)$, which can be described by the Drude model. The magnetic response is ignored and taken as $\mu_d = \mu_m = \mu_0$. When an incident electromagnetic wave travels from the dielectric region to the metal region, the electric field with a component normal to the interface is the primary condition of SP excitation, which induces a surface charge density σ_s along the interface as $\sigma_s \propto (\epsilon_d E_{z1} - \epsilon_m E_{z2})$. As a result, SPs have p-polarized (parallel to the plane of incidence) wave characteristics on the flat interface and only a transverse magnetic (TM) polarized wave can be excited; no surface modes exist for the transverse electric (TE) polarization.

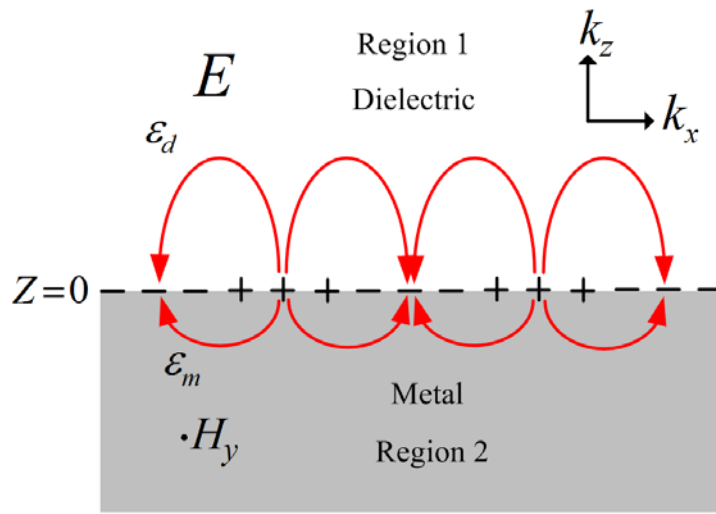


Figure 3.2: Geometry of a single interface between a metal and a dielectric for surface plasmon propagation.

Considering a TM wave incident from a dielectric region to a metal region, the fields in the two media have the following expressions [2]:

For the dielectric region where ($z > 0$),

$$\mathbf{H}_1 = (0, H_{y1}, 0)e^{ik_{z1}z}e^{i(k_x x - \omega t)}, \quad (3.10)$$

$$\mathbf{E}_1 = (E_{x1}, 0, E_{z1})e^{ik_{z1}z}e^{i(k_x x - \omega t)}. \quad (3.11)$$

For the metal region where ($z < 0$),

$$\mathbf{H}_2 = (0, H_{y2}, 0)e^{ik_{z2}z}e^{i(k_x x - \omega t)}, \quad (3.12)$$

$$\mathbf{E}_2 = (E_{x2}, 0, E_{z2})e^{ik_{z2}z}e^{i(k_x x - \omega t)}. \quad (3.13)$$

These fields must satisfy Maxwell's equations,

$$\nabla \times \mathbf{H} = \frac{\varepsilon}{c} \frac{\partial}{\partial t} \mathbf{E}, \quad (3.14)$$

$$\nabla \times \mathbf{E} = -\frac{1}{c} \frac{\partial}{\partial t} \mathbf{H}, \quad (3.15)$$

$$\nabla \cdot \varepsilon \mathbf{E} = 0, \quad (3.16)$$

$$\nabla \cdot \mathbf{H} = 0, \quad (3.17)$$

where c is the speed of light in vacuum;

together with the continuity relations,

$$E_{x1} = E_{x2}, \quad (3.18)$$

$$H_{y1} = H_{y2}, \quad (3.19)$$

$$\varepsilon_d E_{z1} = \varepsilon_m E_{z2}, \quad (3.20)$$

$$k_{x1} = k_{x2} = k_x. \quad (3.21)$$

enables the dispersion relation of SPPs in the system to be obtained:

$$\frac{k_{z1}}{\varepsilon_d} + \frac{k_{z2}}{\varepsilon_m} = 0. \quad (3.22)$$

This dispersion indicates that SPs can only be excited when the dielectric constants of the two media of the interface are of opposite signs.

Finally, the wave-number of SPs in the two media can be shown to be:

$$k_x = \frac{\omega}{c} \left[\frac{\varepsilon_d \varepsilon_m}{(\varepsilon_d + \varepsilon_m)} \right]^{\frac{1}{2}}, \quad (3.23)$$

$$k_{z1} = \frac{\omega}{c} \left[\frac{\varepsilon_d^2}{(\varepsilon_d + \varepsilon_m)} \right]^{\frac{1}{2}}, \quad (3.24)$$

$$k_{z2} = \frac{\omega}{c} \left[\frac{\varepsilon_m^2}{(\varepsilon_d + \varepsilon_m)} \right]^{\frac{1}{2}}. \quad (3.25)$$

The properties of SPs with an electric field propagating along the x-direction (parallel to the surface) and decaying along the z-direction (perpendicular to the surface) determine the complex value of k_x , as well as the purely imaginary values of k_{z1} and k_{z2} . As a result, the condition of $\epsilon_d > 0$, $\epsilon_m < 0$, and $\epsilon_d < |\epsilon_m|$ should be satisfied for SPP propagation. Also, the wave-number of SPs indicates that SPs possess both transverse and longitudinal components.

Figure 3.3 shows the dispersion relation of SPs along the interface between the dielectric medium ϵ_d and metal ϵ_m [2]. When $\omega < \omega_p/\sqrt{1+\epsilon_d}$, the propagation of SPs is bound to the surface, corresponding to non-radiative evanescent surface waves. When $\omega > \omega_p$, both k_x and k_z transform to real values, with SPs radiating out of the surface, which is called radiative SPs.

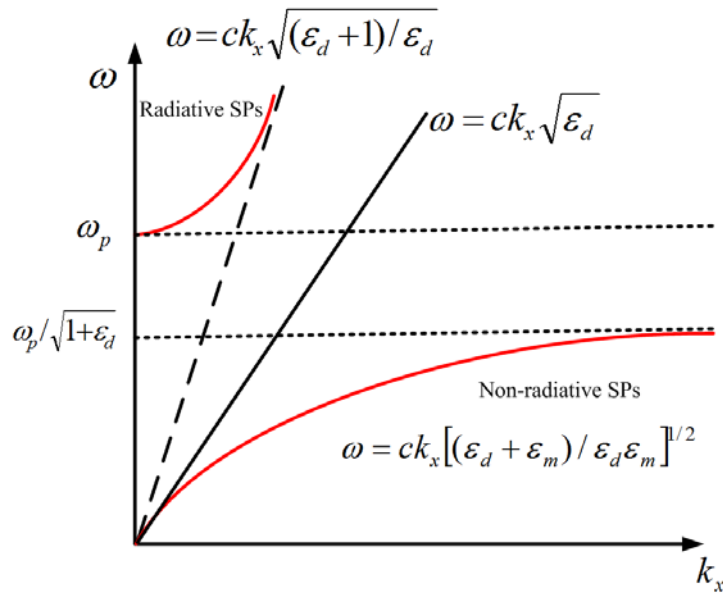


Figure 3.3: Dispersion relation of SPs at interface between the dielectric ϵ_d and metal ϵ_m [2].

3.2.2. Propagation length and skin-depth of SPs on a smooth surface

Since the dielectric constant of a metal is complex, $\epsilon_m = \epsilon_{mr} + i\epsilon_{mi}$, k_x is also complex, i.e. $k_x = k_{xr} + ik_{xi}$. As a consequence, SPs propagating along a metal/dielectric interface exhibit a finite propagation length, L_x , given by [2]:

$$L_x = (2k_{xi})^{-1} = \frac{c}{\omega} \left(\frac{\epsilon_{mr} + \epsilon_d}{\epsilon_{mr}\epsilon_d} \right)^{2/3} \frac{2\epsilon_{mr}^2}{\epsilon_{mi}} \quad (3.26)$$

Wave vectors k_{z1} and k_{z2} are imaginary due to the relations $\omega/c < k_x$ and $\epsilon_{mr} < 0$. The value of the skin depth at the field falls to $1/e$, becomes

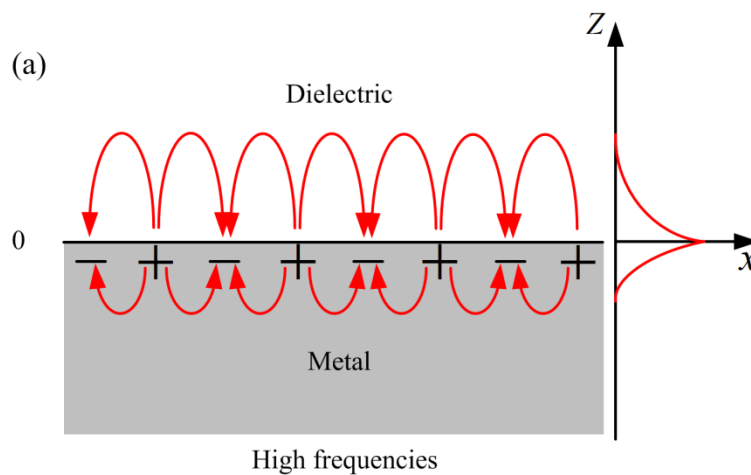
in the dielectric medium:

$$\delta_1 = \frac{1}{k_{z1}} = \frac{c}{\omega} \left(\frac{\epsilon_d + \epsilon_{mr}}{\epsilon_d^2} \right)^{\frac{1}{2}}, \quad (3.27)$$

in the metal medium:

$$\delta_2 = \frac{1}{k_{z2}} = \frac{c}{\omega} \left(\frac{\epsilon_d + \epsilon_{mr}}{\epsilon_{mr}^2} \right)^{\frac{1}{2}}. \quad (3.28)$$

The skin depth and propagation length show a strong dependence on frequency. As shown in Figure 3.4, in the visible regime, SPs exhibit large field confinement to the interface and a subsequent small propagation length due to increased damping. In the terahertz regime, however, SPs fields extend deeper into the dielectric region, which reveals small localization and a larger propagation length. In the terahertz and microwave regimes, SPP waves, which distribute along the surface loosely, are also known as Zenneck waves [80].



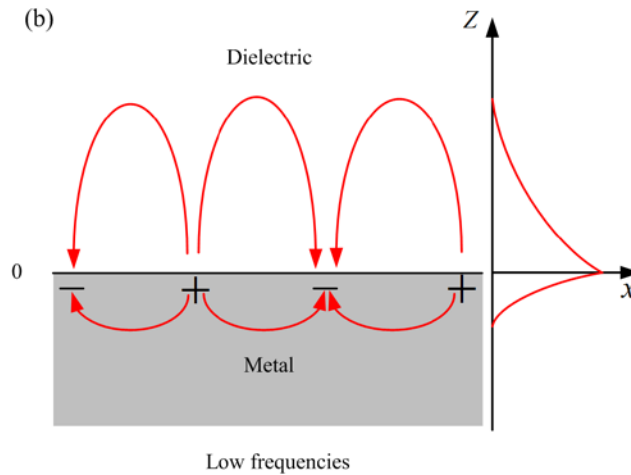


Figure 3.4: Schematic diagram of SPs propagating on a surface defined by the x - y plane at $z = 0$ along the x direction at (a) high and (b) low frequencies. Exponentially decaying electric field as a function of z shown in the x - z coordinate for both low and high frequencies, where $z > 0$ is inside the dielectric and $z < 0$ is inside the metal.

3.3. Surface plasmons excitation by light

In order to excite SPR by irradiation with light, a phase matching condition should be satisfied which states that the excitation of SPR is possible only if the propagation constant of the light vector matches the propagation constant of the SPs [81]. According to the plasmon dispersion relation [2] for any wavelength, SPs have a longer wave vector than light waves of the same frequency propagating at the surface. This condition makes it impossible to excite SPs directly by shining incident light onto a smooth metal surface. The wave vector of light can be adjusted to match the wave vector of the SP by launching it through the metal from a medium with a RI higher than the RI of medium at the boundary where a SP is going to be excited. Standard ways to excite a SPR are to couple light through a prism [72], grating [82] or waveguide [83]. However, in recent years there has been quite an interest to excite SPR on the surface of optical fibres and sub-wavelength holes [84]. Prism coupling is one of the first tested SPR configurations and is discussed in the subsequent section.

3.3.1. Prism configuration

One of the well documented prism configurations used to excite SPR, was first reported by Kretschmann and Raether in 1968 [72]. This configuration is shown in Figure 3.5, where the setup employs a high RI prism (glass) with a metal layer on the prism's bottom and a sample on the other side of the metal layer.

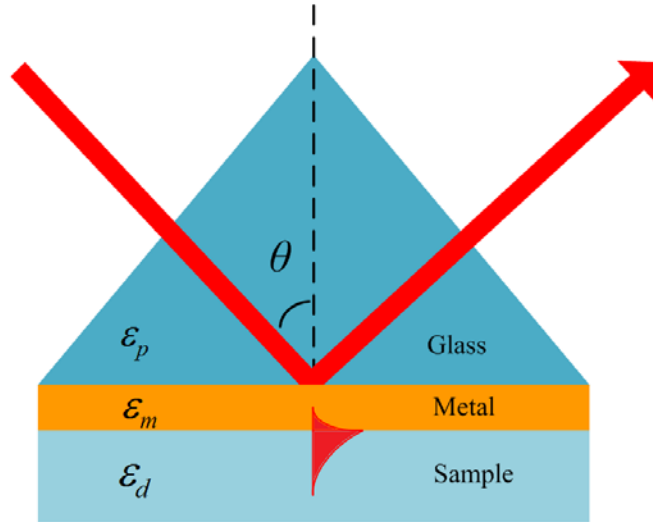


Figure 3.5: Kretschmann SPR configuration.

Light propagating in the prism is reflected at the prism-metal layer interface by means of total internal reflection. The evanescent field of the reflected light at the first interface penetrates into the metal, and if the thickness of the layer allows, it reaches the second metal-sample interface. If the RI of the second sample is smaller than the RI of the prism and also if the propagation constant of light propagating in the prism matches the propagation constant of the SP then a plasmon resonance occurs and a plasmon wave propagates at the second metal-sample interface.

The phase-matching condition that was mentioned in the previous paragraph is:

$$\sqrt{\varepsilon_p} \sin(\theta) = \text{Re} \left\{ \sqrt{\frac{\varepsilon_m \varepsilon_d}{\varepsilon_m + \varepsilon_d}} \right\}, \quad (3.29)$$

where θ is the angle of incidence, $\varepsilon_p, \varepsilon_m$ and ε_d are the frequency-dependent dielectric functions of prism (glass), metal and sample medium ($\varepsilon_p > \varepsilon_d$).

For specific refractive indices of the surrounding medium (sample medium ε_d) and specific wavelengths of light propagating in the prism, there is only one such angle θ when the phase matching condition is satisfied and SPR can be excited. By changing the angle θ at which light propagates in the prism, it is possible to change the parallel component of the light's wave vector, the propagation constant, and to find that the evanescent field at the metal-dielectric layer couples to the SP.

If coupling occurs and the SP interacts with the light wave, some of the light wave's parameters such as amplitude, phase, polarization, and spectral distribution can be altered. For instance, in the angle scanning mechanism, which is shown for the Kretschmann configuration, the SPR resonance will result in a strong decrease of the light reflected from the base of the prism.

The measurement of these parameters (intensity, phase, etc.) makes it possible to track changes of the RI of the dielectric on that side of the metal where the SPR occurs. According to which parameter is going to be measured, SPR sensors can be classified as angle, wavelength, intensity, phase or polarization-modulation sensors. For example, in wavelength-modulation based sensors, SPR can be measured by tracking the resonant wavelength at which SPR occurs at a fixed angle of incidence (Figure 3.6).

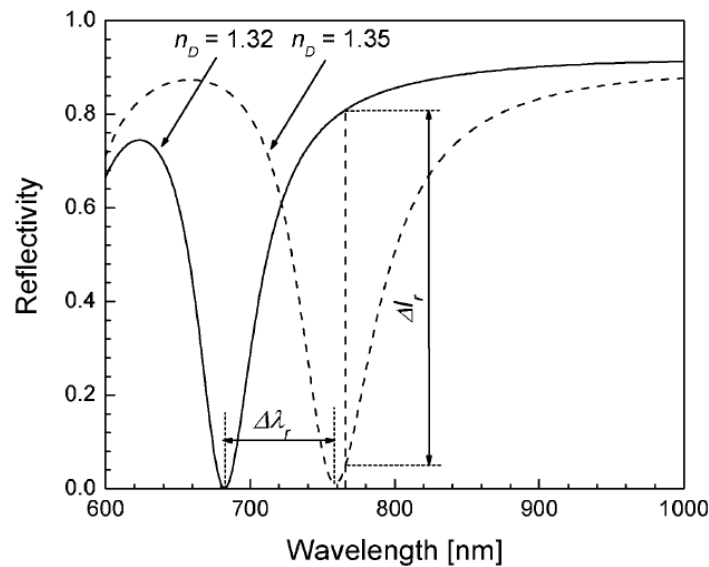


Figure 3.6: Reflectivity for a light wave exciting a surface plasmon in the geometry versus wavelength for two different refractive indices of the dielectric (angle of incidence is 54°) [83]. Note that $\Delta\lambda_r$ = change in reflectivity wavelength; ΔI_r = change in reflectivity intensity; n_D = refractive index of dielectric.

The SPR sensor with a prism configuration as a platform for sensing was commercialized by several companies including: Biacore [4], Texas Instruments [85], Autolab [86], IBIS [87], Reichert [88] and XanTec [89]. The first commercialized SPR biosensors were developed for laboratory measurements and were rather bulky but today's biosensing platforms based on the Kretschmann configuration can be compact, low cost and portable devices, which can

work not just in laboratories but also in the field [90]. The reported index resolution of the prism-based sensors is about $10^{-6} - 10^{-8}$ RIU (refractive index unit)[91,92].

3.3.2. Excitation of SPR in an optical fibre

Even though sensors currently based on the Kretschmann configuration can be relatively small, there has been an attempt to realize SPR in optical fibre to produce a more compact sensor with remote sensing capabilities. Excitation of SPR in optical fibres is similar to the excitation of SPR in the prism configuration. Light propagating in the fibre core and cladding in the form of modes experience TIR at the cladding-core and cladding-exterior medium interfaces. Different modes hit the cladding-core and cladding-exterior medium interfaces at different angles. Similarity between light propagation in the optical fibre via total internal reflection and in prism configuration have led to many successful attempts to realize SPR sensors in optical fibres.

Recently, remarkable progress has been made to SPR, localized SPR and photonic crystal fibre technologies, new types of optical fibre SPR-based sensors have attracted growing attention in the research community. Therefore, it is not feasible to review all information in these areas. The details and some excellent reviews on some of the studies can be found in the references [5,93-95]. Some of the general SPR fibre sensors are shown in Figures 3.7(a) - (e), and some of the currently used or explored SPR fibre sensors are shown in Figures 3.8(a) - (f).

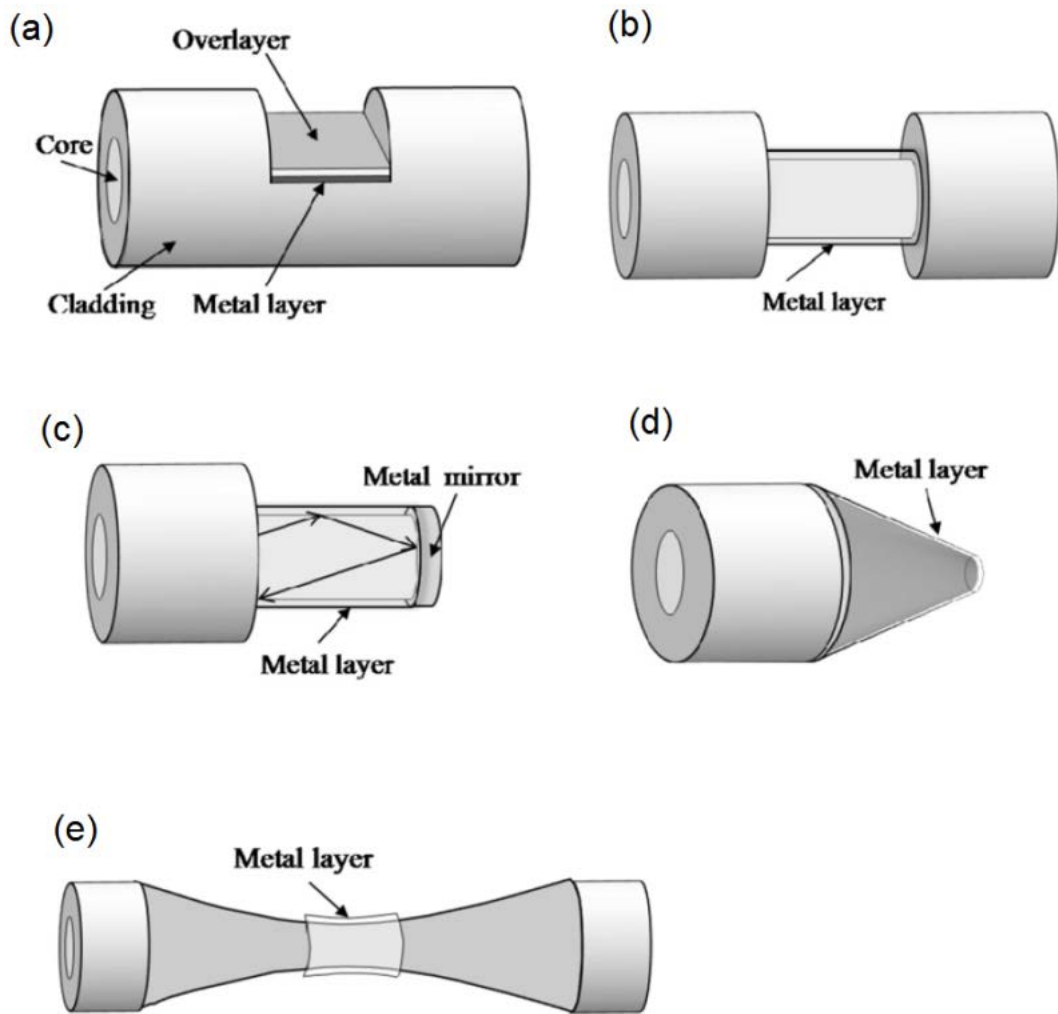


Figure 3.7: General SPR optical fibre sensors include (a) D-shape fibre, (b) cladding-off fibre, (c) end-reflection mirror, (d) angled fibre tip, and (e) tapered fibre [95].

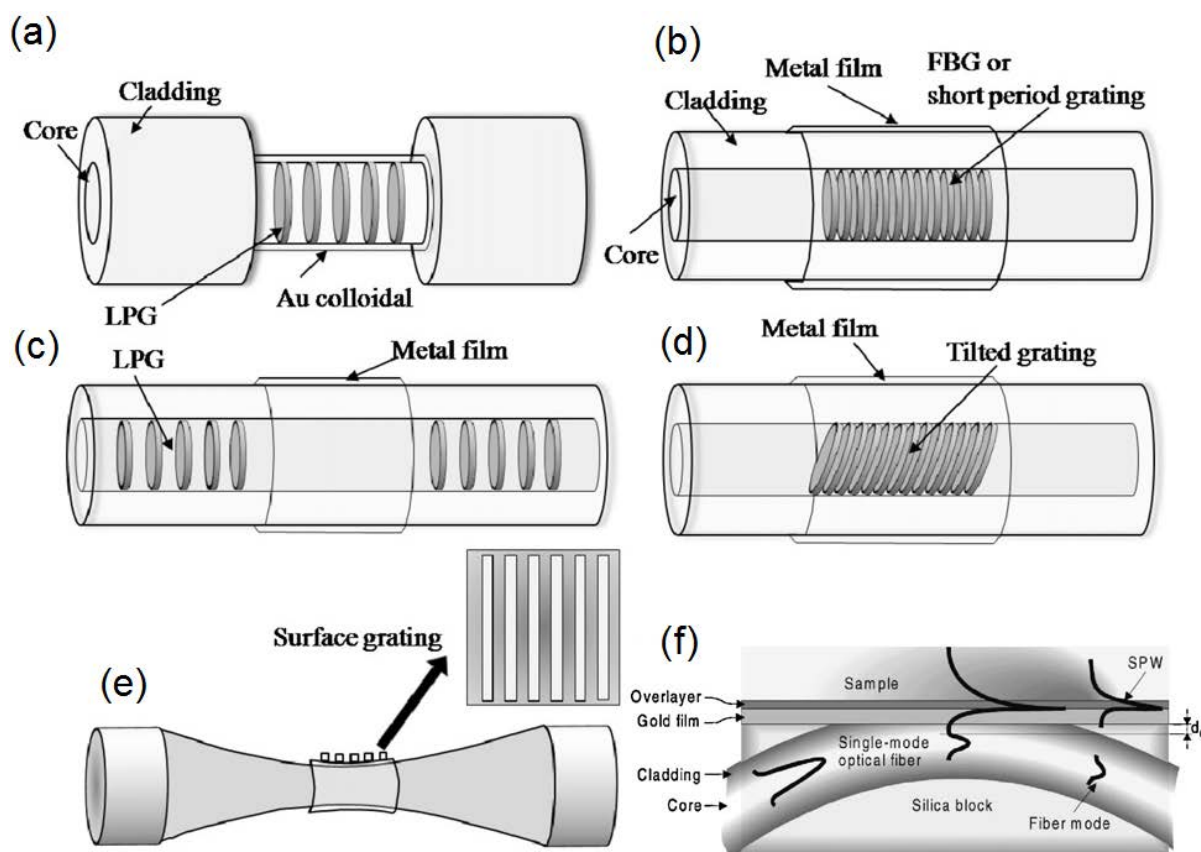


Figure 3.8: Various SPR optical fibre configurations. (a) long period grating (LPG), (b), fibre Bragg grating (FBG), (c) LPG pair, (d) tilted grating, (e) metal surface grating, and (f) side-polished fibre [95,96].

Most of the realized fibre-based SPR sensors work in the transmission regime where light from a broadband source is launched into one end of the fibre and is detected at the other end. This configuration is shown in Figure 3.9(a). If surface plasmon resonance occurs and one of the modes couples to the SP detected power at a wavelength of this mode, the power will decrease resulting in a spike in the spectrum. To date, fibre SPR sensors work as wavelength encoding, rather than as angle encoding which occurs in the prism configuration.

SPR fibre sensors can work in the reflection regime (fibre probe) as an alternative to the transmission regime. Figure 3.9(b) shows a sensor consisting of the fibre with a perfect cleave and a layer of gold or another reflecting material at one end of the fibre which reflects light back towards the detector at the opposite end. Light propagating in the fibre is being altered by coupling to the SP if SPR occurs. The reflected light from the cleaved side is detected when travelling back. The design of the probe allows the sensor to be extremely compact, user-friendly and practical for *in situ* measurements in small spatial volumes.

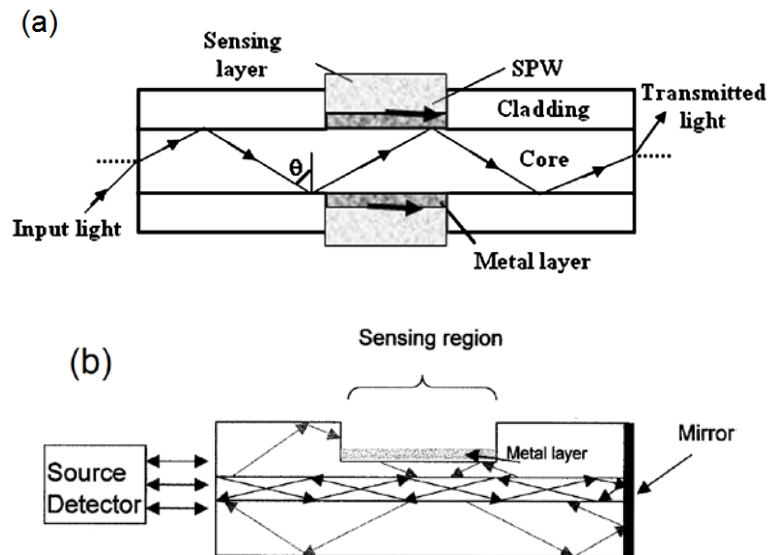


Figure 3.9: Diagram showing fibre SPR sensors working in the transmission mode (a) and reflection mode (b) [5].

Even though the sensors described here work in different modes, have different geometrical parameters and are suited for a variety of different applications, they have similar sensing mechanisms. The SPR sensing mechanism is the most important element of the sensor design and defines crucial sensing parameters such as sensitivity, compactness, and robustness.

Unfortunately in standard telecommunications fibre (SMF 28 from Corning), the coupling mechanism corresponding to the prism configuration is not strong enough to excite a surface plasmon resonance. If the standard fibre is coated with gold, or another SPR active metal and the phase matching condition is satisfied by the core mode, SPR will not be excited on the fibre surface because the strength of the resulting evanescent field from TIR at the core-cladding interface is too weak to cross the cladding and interact with the metal layer. Cladding modes can also be employed to excite SPR. However, a coupling mechanism must be provided to couple light from the core mode to cladding modes. Consequently, there are no SPR sensors based on the standard single mode fibre without deformations or modifications. Existing approaches are based on the excitation of SPR by means of enhancing the evanescent field near the metal layer and can be divided in two groups.

In the first group of approaches, the fibre is deformed in such a way that the metal layer is located in proximity to the core and core-cladding interface. The evanescent field resulting from the core mode reflection at the core-cladding interface can excite a SPR if it is strong enough to reach the metal layer. The metal layer can be located in proximity of the core-

cladding interface by partially or completely removing the cladding. Typically, this can be achieved by creating a deep cut in the cladding [62] or by bending the fibre and polishing one of the fibre's sides [97-101] or by use of a non-standard fibre such as D-type optical fibre [45]. Another accepted approach is to use a tapered fibre [65]. In some approaches, as is the case for this work, it has been suggested that the plain metal coating can be replaced by nanoparticle layers [102,103], which may improve the performance of SPR fibre sensors.

Primarily, the approaches mentioned here were proposed in the 1990s. The minimal detectable index resolution for these types of SPR sensors is in the range of 10^{-4} to 10^{-6} RIU, which is close to but does not exceed the resolution of prism-based SPR sensors. However, some researchers achieved extremely high resolution for fibre SPR sensors of approximately 10^{-7} RIU by precise control of the polarization of light and disturbances occurring during the experiment [104] and by precise control during metal deposition and the creation of semi-cylindrical metal coatings which are able to support different hybrid surface plasmon modes [105].

One of the disadvantages of the sensors mentioned here is the fact that the SPR is getting excited in both multimode and single mode based fibres by uncontrolled fields. As a result, experimental results show broad and ill-defined SPR resonances in the spectra that decrease the overall sensor performance. From another perspective, these sensors are based on modified, non-standard fibres that may result in a highly fragile sensor with possibly a higher cost compared to sensors made of unmodified standard fibres.

The second group of approaches is relatively new. Fibre gratings are being used to couple light to a specific mode that generates an evanescent field at the core-metal or cladding-metal interface strong enough to excite SPR. He *et al.* [106] proposed a LPG for coupling of the core mode to the co-propagating cladding mode with a specific value of the wave vector such that it can excite a SPR. Nemova and Kashyap [107] proposed to use a FBG to couple light to a back-propagating core mode in a hollow core fibre and in a fibre with non-standard geometrical parameters (core diameter is $26\ \mu\text{m}$ and cladding diameter is $30\ \mu\text{m}$). A small cladding coupled with a large core radius allows strong field overlap between the reflected back core mode and the SP.

Although these proposed approaches employing LPGs and FBGs show a promising level of sensitivity, predicting $\sim 10^{-5}$ - 10^{-6} RIUs [107], they have a few drawbacks. Firstly, in the case of both LPG and FBG based sensors SPR excitation occurs because of coupling of only one

certain mode to the SP that can either be a forward propagating cladding mode or a backward propagating core mode. Use of only one mode limits the operating range of the sensor; however, this can be overcome by multiple writings of the gratings with different periods, making the sensor design more complicated. Secondly, the sensor's design with a FBG requires a complicated fibre configuration. The length of FBGs in the proposed design by Nemova and Kashyap is long and can vary from 2 to 10 cm. Such parameters make the sensor's design not as compact and simple as it must be implemented with specialised optical fibres. Use of a tilted grating in the SPR sensor allows several (up to several hundred) cladding modes to be used for SPR excitation. This overcomes such problems occurring with LPGs and FBGs based sensors that have limited operating range and bulky sensor geometry. Experimental work [108] showed that a tilted FBG written in lapped fibre could achieve a high sensitivity of 3365 nm/RIU and wide operating range ($\Delta n_d = 0.8$ in aqueous media). Although this work is one of the most advanced in its field, it still possesses some disadvantages such as a wide SPR resonance (> 50 nm) and the use of a modified highly fragile fibre.

For the design and analysis of the sensor responses, the values for the electric permittivity of the metal films are needed. These values depend on the wavelength of light. Most of the studied SPR optical fibre sensors have wavelength range covering from 400 nm to 800 nm or are in the 2nd or 3rd telecom bands [95]. Listed in Table 3.1 are performance parameters of a variety of optical fibre and SPR-based optical fibre sensors documented in the literature.

(a)

Sensor type	Detection RI range	Sensitivity	Ref.
SPR MMF - bare core, Au coating	~ 1.33 - 1.37	~ 2×10^{-4} RIU	[109]
SPR SMF - side-polished, Au coating, Al mirror, Ta ₂ O ₅ overlayer	~ 1.328 - 1.338	~ 4×10^{-5} RIU	[110]
FBG - side-polished	~ 1.445, ~ 1.455	~ 1.4×10^{-5} RIU, ~ 4×10^{-6} RIU	[101]
PCF FBG - Ge-doped core	~ 1.33 - 1.44	~ 4×10^{-3} - ~ 2×10^{-5} RIU	[111]
PCF - tapered	> 1.440	~ 1×10^{-5} RIU	[112]
LPG	~ 1.330 - 1.426	~ 2.1×10^{-5} RIU	[113]
D-type - Au coating	~ 1.332 - 1.337	~ 1×10^{-5} RIU	[45]
SMF - thin cladding, Ta ₂ O ₅ overlayer	~ 1.329 - 1.353	~ 5×10^{-7} RIU	[104]
SMF - semi-cylindrical, Au coating	~ 1.444 - 1.454	~ 7×10^{-7} RIU	[105]
FBG - hollow core	~ 1.33 - 1.334	~ 10^{-5} - 10^{-6} RIU	[107]

(b)

Sensor type	Detection RI range	Sensitivity	Ref.
SPR SMF - cladding removed, Au coating	~ 1.35 - 1.42	~ 5000 nm/RIU	[95]
SPR MMF - cladding removed, Au-Ag alloy nanoparticle	~ 1.342 - 1.346	~ 3000 nm/RIU	[103]
SPR MMF - cladding removed, Au coating, surface roughness	~ 1.3335 - 1.4018	~ 1600 - 3000 nm/RIU	[6]
LPG - 3 μ m planar, Au coating	~ 1.329 - 1.340	~ 1100 nm/RIU	[114]
FBG - tilted grating, Au coating	~ 1.3 - 1.38	~ 3365 nm/RIU	[108]
MMF - modified end-face	~ 1.33 - 1.376	~ 533 nm/RIU	[13]
MMF - Tapered, Au coating	~ 1.333 - 1.343	~ 2700 - 4900 nm/RIU	[115]
MMF - Tapered, Au coating	~ 1.33 - 1.343	~ 2750 - 15000 nm/RIU	[116]
MMF - flat tip, Ag mirror, SiO layer	~ 1.3365, ~1.4126	~ 3800 nm/RIU	[117]

Table 3.1 (a) and (b): Documented performance parameters of various optical fibre refractive index sensors. Note that $\Delta\lambda/\Delta n \Leftrightarrow$ nm/RIU and $\Delta n \Leftrightarrow$ RIU.

Since the initial discovery of Extraordinary Optical Transmission (EOT) (Chapter 4), significant interest has arisen, both for potential applications in novel nanophotonic devices, and also for understanding the underlying physical mechanism. Various types of configurations for multimode fibre SPR sensors based on EOT have been proposed. At the time that this research was conducted, a report on nanostructures based on sub-wavelength apertures for chemical and biological sensing applications was presented by Dhawan *et al.* [13]. It describes experimentally the use of periodic arrays of nanostructures with sub-wavelength dimensions and submicron periodicity fabricated by focused ion beam milling on gold-coated tips of silica optical fibres. Nanoparticles attached to the fibre end-faces have also been used for RI sensing [14]. The optical properties of coupled metallic nanorods fabricated on the end-face of a fibre have also been reported [12].

In general, most of the proposed optical fibre SPR sensors based on metallic nanostructure technology do not have a proper theoretical understanding. Generally, the published experimental results were used to provide solutions for the optical fibre SPR sensors. Complications occurring during the manufacturing of sensors may result in changes to the SPR phase matching condition and possibly a widening of SPR and, as a consequence, a reduced sensitivity. The research conducted to date has shown that much has been accomplished in this field. However, more work can be done to develop new approaches and to improve the performance of the proposed sensors, in order to make them more robust and simplified.

This thesis investigates the current state of the art in the fields of surface plasmon resonance (SPR) and sub-wavelength apertures. Together, these can be used to apply on the end-face of an optical fibre to produce a liquid refractive index sensor. In the next Chapter, the various properties of metallic sub-wavelength apertures will be covered.

Chapter 4. Metallic Sub-wavelength Apertures

4.1. Introduction

The interaction of light with metal surfaces has become an exciting area of optics since the discovery of Enhanced Optical Transmission (EOT) through thin metallic films perforated with sub-wavelength apertures [8]. In this area of optics, the physical dimension of components for optical measurements is on a nanometre scale. Interestingly, the optical properties of sub-wavelength structures are different from classical electromagnetic theory [9]. This new field of research has enabled the possibility of controlling light via nanostructures. This capability of manipulating light attracts numerous applications in various fields of science and technology, for example, Raman spectroscopy, photonic circuits, display devices, nanolithography and biosensors [118-121].

The physical mechanism behind the EOT is still under investigation. Some authors have focused on the critical role of surface plasmon polaritons (SPPs) in EOT [84,122-127], while others have suggested that EOT is contributed by several diffractive and interference phenomena such as a composite diffractive evanescent wave (CDEW), Wood's anomalies, localized surface plasmons (LSPs), and quasi-bound modes [128-131]. The main reason for this debate is that the surface plasmon polariton model shows a discrepancy between calculated and measured data [122]. A transmission model explaining the enhanced transmission seeks to unify both the surface plasmon and the diffraction model [132,133]. This model proposes an analysis using a Fano profile in transmission spectra which is attributed to a superposition of the resonant process and non-resonant process. Borisov *et al.* [134] proposed a diffraction model for the enhanced transmission of sub-wavelength structures. This group suggested that the enhanced transmission of sub-wavelength hole arrays is due to interference of diffractive and resonant scattering. The contribution of the resonant scattering comes from the electromagnetic modes trapped in the vicinity of structures. This trapped electromagnetic mode is a long-lived quasi-stationary mode and gives an explanation of extraordinary resonant transmission. Recently, Jiang *et al.* [135] verified the effect of Wood's anomalies on the profile of extraordinary transmission spectra when the periodic metal arrays perforated with sub-wavelength rectangular holes was used. The group confirmed that Wood's anomalies play an important role in shaping the spectral profile of the transmission peak.

Most studies have focused on unusual high transmission resonances through a thin metallic film with sub-wavelength apertures arrays in the optical [130,136], microwave [137], infrared [138], and terahertz (THz) [139,140] regions. The high transmission can be affected by the RI of the adjacent medium [141], the shape and orientation of the apertures [142,143], lattice geometry [8,139] and film thickness [144]. As stated above, in all these measurements, the true influence of the shape of the apertures on the extraordinary transmission still remained unclear, particularly on the peak position shifts and changes associated with the intensity. This thesis is part of an Australian Research Council (ARC) project [145] to investigate the extraordinary light transmission through nanostructure materials and its application in sensing.

This chapter begins with the theory of surface plasmon excitation on periodic arrays of sub-wavelength apertures. Then, the mechanism of transmission via surface plasmon coupling in a periodic nanohole array is discussed. The chapter concludes with a brief discussion of the CDEW method, Fano analysis, an analysis of Fabry-Perot resonances in a cross-shaped array and a summary of the currently investigated sub-wavelength apertures.

4.2. Surface plasmon excitation on a periodic array of sub-wavelength apertures.

There are two ways to excite the SP optically on an interface of a dielectric and a metal. First, one can use a dielectric prism (Chapter 3) to make coupling between the incident photons and the surface plasmon on an interface between the prism and the metal. Second, one can use periodic structures (grating) on the metal surface. When light is incident on the grating surface, the incident light is scattered. The surface component of the scattered light gets additional "momentum" from the periodic grating structure. This additional momentum enables the surface component of the scattered light to excite the surface plasmon on the metal surface.

Consider a one dimensional gratings as shown in Figure 4.1(a). When light with a wave number k_0 is incident on a periodic grating on a metal surface with an incident angle θ_0 , the incident light excites the surface plasmon on the metal surface. The momentum conservation equation allows this surface plasmon to have a wave vector, k_{sp} , equal to a sum of the x -component of the incident wave vector and an additional wave vector which is the Bragg vector associated with the period of the structure:

$$k_{sp} = k_0 \sin \theta_0 + q \frac{2\pi}{P}, \quad k_0 = \frac{\omega}{c} \quad (4.1)$$

where k_0 is the wave number of the incident light, and P is the period of the grating structure, and q is an integer.

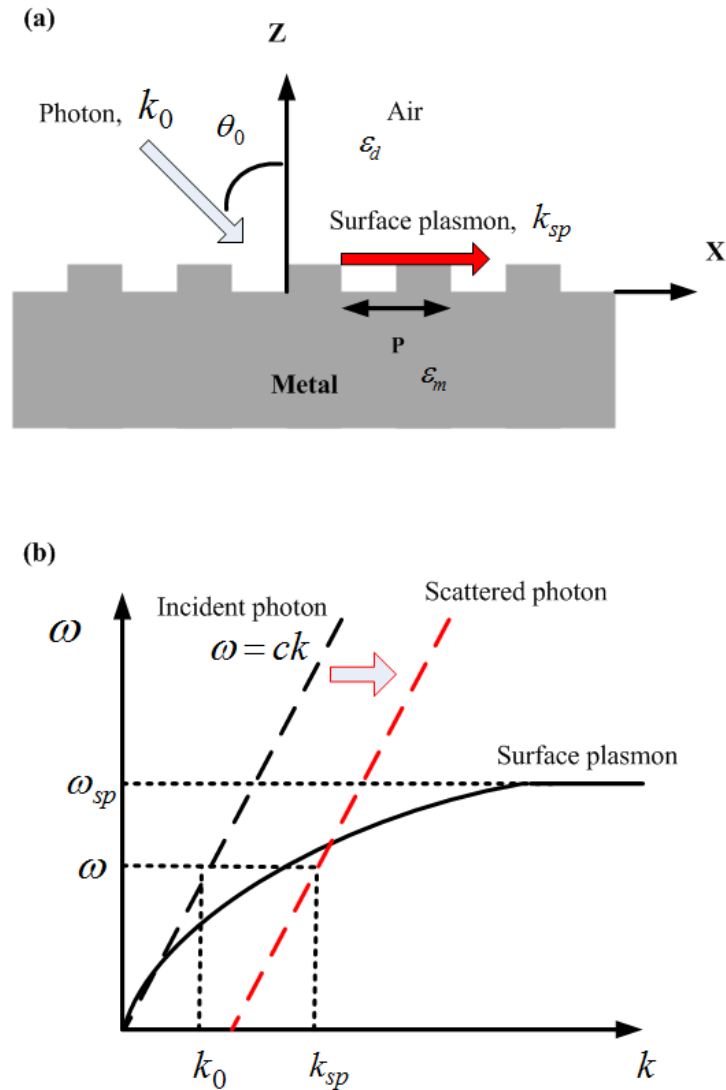


Figure 4.1: Schematic diagrams of (a) the excitation of the surface plasmon by the incident photon on a metallic grating surface and (b) the dispersion curves of the incident photon and the surface plasmon.

As shown in Figure 4.1(b), this additional wave vector shifts the dispersion line of the incident light to the dispersion line of the diffracted photon. This light line crosses the dispersion curve of the surface plasmon. This crossing means that the incident light couples with the surface plasmon on the metal grating surface.

Next, consider an incident beam of light on a 2D grating (metal with ϵ_m) surrounded by a dielectric medium ϵ_d (see Figure 4.2),

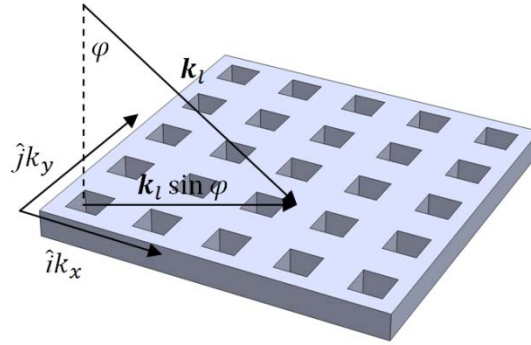


Figure 4.2: 2D grating with incident photon having wave-vector k_l .

where \hat{i} and \hat{j} are vectors along the coordinate axis, \vec{k}_x and \vec{k}_y are the reciprocal lattice wave-vectors for a square lattice with $k_x = k_y = 2\pi/P$ (P is periodicity of the array) and $k_l \sin \varphi$ is the in-plane component of the light's wave-vector.

The effective light's wave-vector due to the additional momentum that was gained by coupling to the grating's momentum is [122]:

$$\vec{k}_{eff} = \vec{k}_l \sin \varphi + \hat{i}k_x + \hat{j}k_y . \quad (4.2)$$

The condition (at resonance) for exciting the SPs requires, $\vec{k}_{sp} = \vec{k}_{eff}$, where \vec{k}_{sp} is the surface plasmon wave-vector. This yields,

$$\vec{k}_{sp} = \vec{k}_l \sin \varphi + \hat{i}k_x + \hat{j}k_y . \quad (4.3)$$

In particular, this thesis will mainly cover light at normal incidence, i.e. $\varphi = 0$. This gives,

$$\vec{k}_{sp} = \hat{i}k_x + \hat{j}k_y . \quad (4.4)$$

From Equation (3.20) gives,

$$k_{sp} = \frac{\omega}{c} \sqrt{\frac{\varepsilon_d \varepsilon_m}{\varepsilon_d + \varepsilon_m}} = \frac{2\pi}{\lambda} \sqrt{\frac{\varepsilon_d \varepsilon_m}{\varepsilon_d + \varepsilon_m}}, \quad (4.5)$$

where $\omega/c = 2\pi/\lambda$, is the wave-vector of light.

Combining Equations (4.4) and (4.5) while noting that $k_x = k_y = 2\pi/P$ gives,

$$\vec{k}_{sp} = (\hat{i} + \hat{j}) \frac{2\pi}{P} \Leftrightarrow \frac{2\pi}{\lambda} \sqrt{\frac{\varepsilon_d \varepsilon_m}{\varepsilon_d + \varepsilon_m}} = \sqrt{i^2 + j^2} \frac{2\pi}{P}. \quad (4.6)$$

Re-arranging Equation (4.6) and solving for λ_{\max} (the wavelength at which a transmission peak is observed) gives,

$$\lambda_{\max} = \frac{P}{\sqrt{i^2 + j^2}} \sqrt{\frac{\varepsilon_d \varepsilon_m}{\varepsilon_d + \varepsilon_m}}. \quad (4.7)$$

Equation (4.7) allows for the calculation of transmission peak positions, λ_{\max} , at normal incidence for light interacting with a periodic array of nanometre size apertures. Notice that by changing the periodicity, P , or the respective dielectric constants, ε_d or ε_m , one would change the observed transmission peak positions. This is an important equation for this thesis and will be considered in more detail in Sections 5.4 and 6.1.

4.3. Mechanism of transmission via surface plasmon coupling in a periodic nanohole array

As previously mentioned, the surface plasmon is a collective excitation of the free electrons at the interface between a metal and a dielectric. This surface plasmon can couple to photons incident on the interface of the metal and insulator if there exists a periodic grating structure on the metal surface. The coupling between photon and surface plasmon forms the surface plasmon modes on the interface. If both sides of the metallic film have the same periodic structure (i.e. an array of nanoholes, as shown in Figure 4.3(a)), the surface plasmon modes on the input and exit sides couple and transfer energy from the input side to the exit side. The surface plasmon modes on the exit side decouple the photons for re-emission. In this optical

transmission process, the energy transferred by the resonant coupling of the surface plasmon on the two sides is a tunnelling process through the sub-wavelength apertures. Therefore, the intensity of the transmitted light decays exponentially as the film thickness increases. A transmission mechanism in a sub-wavelength hole array is shown in Figure 4.3(b).

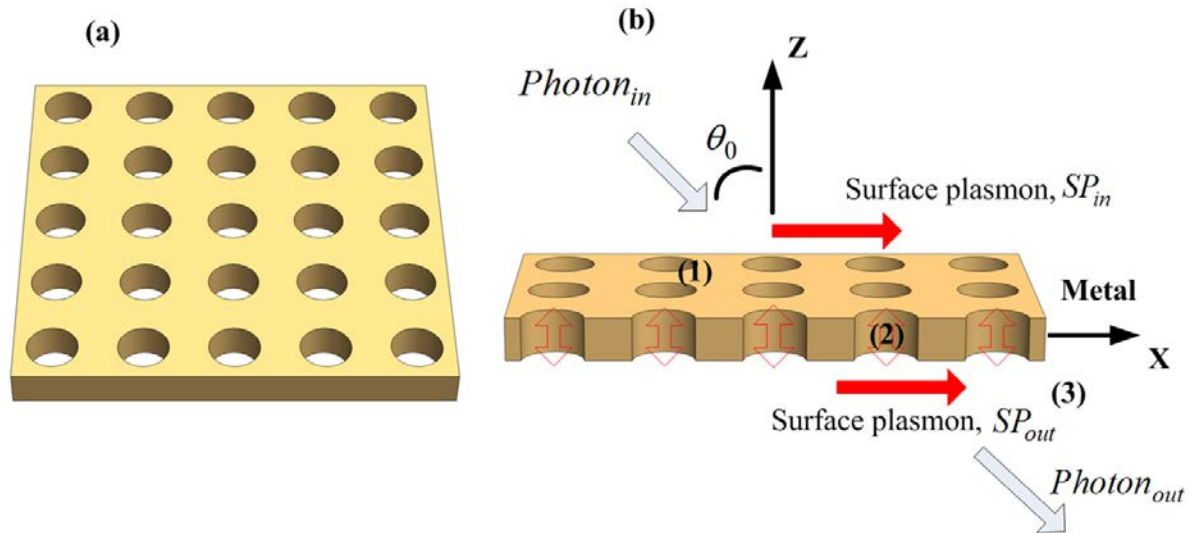


Figure 4.3: Schematic diagram of: (a) a 5×5 array of nanoholes; (b) transmission mechanism in a sub-wavelength nanohole array: (1) excitation of surface plasmon by the incident photon on the front surface, (2) resonant coupling of surface plasmons of the front and back surfaces, (3) re-emission of photon from surface plasmon on the back surface.

Further to the above, there is another element which is called the localized surface plasmon polariton (LSPP) or localized surface plasmon (LSP) [130,146,147] that plays an important role in this process. The LSPP is a dipole moment formed on the edges of a single aperture due to an electromagnetic field near the aperture and it depends mainly on the geometrical parameters of each hole. The LSPP makes a very high electromagnetic field in the aperture and increases the probability of transmission of the incident light. LSPPs will be discussed in the next section.

4.4. Localized surface plasmon polaritons (LSPPs)

In addition to the propagating SPs at the metal/dielectric interface, the geometries on the metal film, such as nanoparticles or nanoholes, will involve the localized surface plasmon polaritons (LSPPs), which are confined to the boundary of the metal structures of sub-wavelength dimensions. LSPPs, also called localized shape resonance, are non-propagating excitations and are characterized by discrete, complex frequencies depending on the size and

the shape of the objects and the dielectric constant of the constituent materials. Different from the propagating SPs, LSPPs only possess a longitudinal component, as the transverse component vanishes due to localization of the electrons around the edge of nanoparticles or nanoholes.

4.4.1. LSPPs of metallic nanoholes

When electromagnetic waves impinge on sub-wavelength nanoholes, electrons accumulating around the edge of the nanoholes enable excitation of LSPPs. Recent theoretical and experimental studies show that LSPPs, which depend on the dimensions and geometry of the nanoholes, also contribute to the enhanced transmission through a sub-wavelength metallic nanohole array in addition to SPs [148,149].

In order to exclude the effect of SPs excited in the periodic nanohole arrays, single nanohole and random hole arrays have been used to study the transmission properties of LSPPs [150,151]. In Figure 4.4(a), a plane wave is incident normally to a single sub-wavelength rectangular hole with $E \parallel y$ (long axis) and $H \parallel x$ (short axis). The surface current I_s is induced along the surface of the metal. In the vicinity of the hole, I_s distorts the current distribution to avoid the hole. Also, the induced charges accumulate at the opposite side along the y axis. In Figure 4.4(b), the magnetic field above the aperture, without the support of the underlying surface current, enters into the aperture on one side and emerges from the other side. The aperture can be regarded as an equivalent magnetic dipole that oscillates along the x axis. The equivalent electric dipole of the aperture is shown in Figure 4.4(c), which is induced by the accumulated charges confined at the edges of the aperture. As the parallel component of the electric field cannot exist on a conducting surface, the electric field in the vicinity of the aperture originates and terminates at the edge of the aperture. In the far field of the hole, the electric field along the z -axis plays an important role and can be regarded as equivalent to an electric dipole along the z -axis. When an incident plane wave impinges on the aperture, the incident magnetic field along the x -axis excites the magnetic dipole resonance. However, the electric dipole resonance does not exist due to the perpendicular incident electric field. As a result, the single sub-wavelength aperture can be regarded as a magnetic dipole resonance normal to the incident electric field direction [136,150].

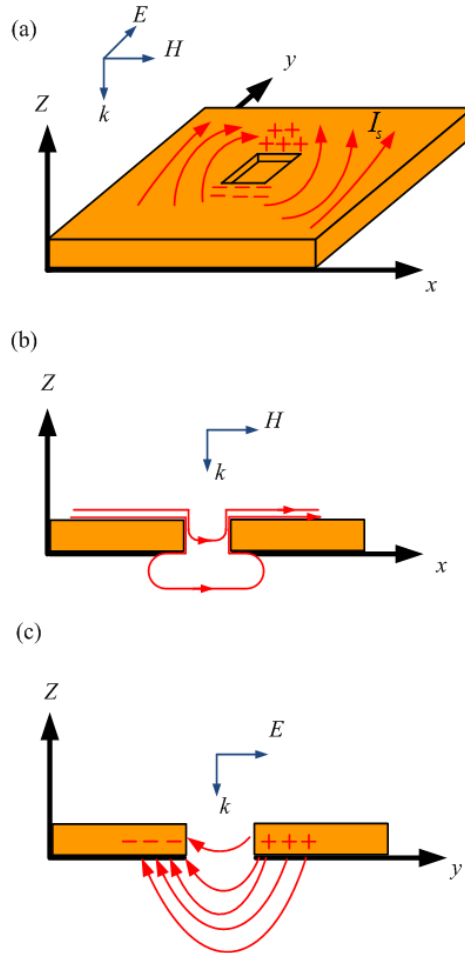


Figure 4.4: (a) Schematic of the surface current I_s and accumulated charges along edge of the hole induced by normally incident plane wave. (b) The equivalent magnetic dipole of the hole. (c) The equivalent electric dipole of the hole.

4.5. Composite diffractive evanescent wave (CDEW)

The CDEW [129,152-154] is a description that assists in explaining the enhanced transmission by periodic structures. The CDEW describes the constructive interference of electromagnetic waves diffracted by a periodic sub-wavelength structure which is considered responsible for the enhanced transmission phenomenon. This diffraction model can explain the enhanced transmission of an array of apertures in a perfect conductor or in non-metallic materials which the surface plasmon model cannot explain.

4.5.1. The principle of the CDEW

The CDEW method originates from scalar near-field diffraction. An electromagnetic wave diffracted by a two dimensional structure can be separated into two contributions: radiative (homogeneous) and evanescent (inhomogeneous) [155]. The diffracted wave equation for the two dimensional structure is based on the solution to the two dimensional Helmholtz equation:

$$(\nabla^2 + k^2)E(x, z) = 0 \quad (4.8)$$

where

$$\nabla^2 = \frac{\partial^2}{\partial x^2} + \frac{\partial^2}{\partial y^2}, \quad k = \frac{2\pi}{\lambda}$$

and

$$E(x, z) = E_0 e^{i(k_x x + k_z z)}$$

Consider an electromagnetic wave propagating in the x and z directions. As mentioned above, the diffracted wave is a sum of the radiative (homogeneous) and the evanescent (inhomogeneous) contributions:

$$E(x, z) = E_{ra}(x, z) + E_{ev}(x, z) \quad (4.9)$$

Note here that the radiative and the evanescent components separately satisfy the Helmholtz equation.

Consider an incident plane wave where a wave vector k_0 impinges on a single slit of width d in an opaque screen, as shown in Figure 4.5(a). The momentum conservation of the incident wave and the diffracted wave should satisfy:

$$k_z = \sqrt{k_0^2 - k_x^2} \quad (4.10)$$

where k_x and k_z are the wave vectors of the diffracted wave in the x and z directions. If k_x is real and if $k_x > k_0$, then

$$k_z = i\sqrt{k_x^2 - k_0^2} \quad (4.11)$$

This result means that the diffractive wave propagates in the x direction while being confined and evanescent in the z direction. This evanescent mode of the diffracted wave emerging from the aperture grows as d/λ becomes smaller. In contrast, for $k_x < k_0$, k_z remains a real quantity and the light is diffracted into a continuum of the radiative, homogeneous mode. In Figure 4.5, the diffraction by an aperture is described in real space (a) and k -space (b). The blue lines represent the radiative modes ($k_x < k_0$), whereas the red lines represent the evanescent mode ($k_x > k_0$). The surface plasmon mode in this picture is the green line which is one of the evanescent modes diffracted by the aperture.

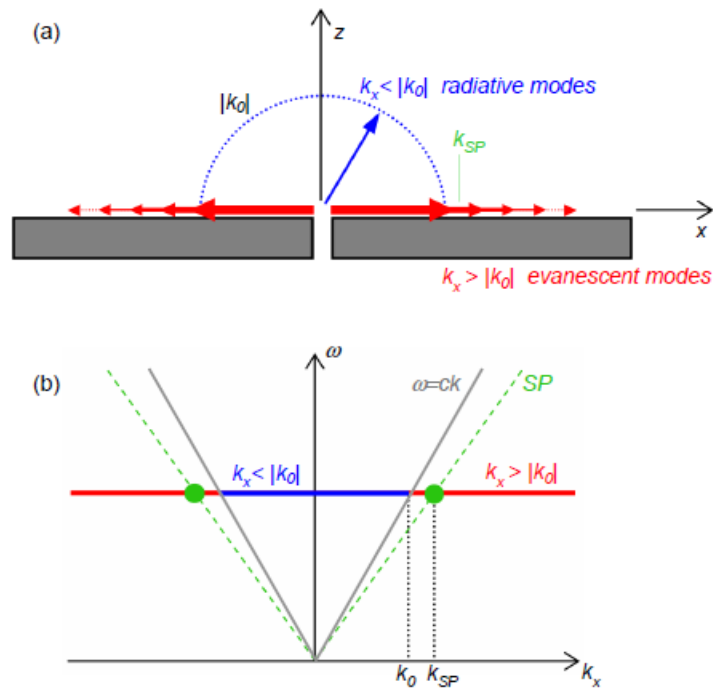


Figure 4.5: Geometry of optical scattering by a hole in a real screen in (a) real space and (b) k -space for a range that k_x is close to zero [129].

In order to find the specific solutions for the radiative and evanescent modes, one needs to solve Equation (4.8). The solution for E_{ev} at $z = 0$ is

$$E_{ev}(x, 0) = -\frac{E_0}{\pi} \left\{ \text{Si} \left[k_0 \left(x + \frac{d}{2} \right) \right] - \text{Si} \left[k_0 \left(x - \frac{d}{2} \right) \right] \right\} \quad \text{for } |x| > \frac{d}{2} \quad (4.12)$$

$$E_{ev}(x, 0) = \frac{E_0}{\pi} \left\{ \text{Si} \left[k_0 \left(x + \frac{d}{2} \right) \right] + \text{Si} \left[k_0 \left(x - \frac{d}{2} \right) \right] \right\} \quad \text{for } |x| \leq \frac{d}{2} \quad (4.13)$$

where E_0 is the amplitude of the incident plane wave and $\text{Si}(\beta) \equiv \int_0^\beta \frac{\sin t}{t} dt$.

The surface wave on the metallic film, Equation (4.12), can be simplified, to a good approximation, as [129],

$$E_{ev} \approx \frac{E_0 d}{\pi x} \cos \left(k_0 x + \frac{\pi}{2} \right) \quad (4.14)$$

From the expression of the CDEW in Equation (4.14), one should notice that the amplitude of the CDEW decreases as $1/x$ with the lateral distance, x , and its phase is shifted by $\pi/2$ from the propagating wave at the centre of the slit. These results are different to the surface plasmon results. The phase of the surface plasmon is equal to that of the incident wave and its amplitude is constant if absorption is not considered [129]. Figure 4.6 shows the lateral field profile of the CDEW.

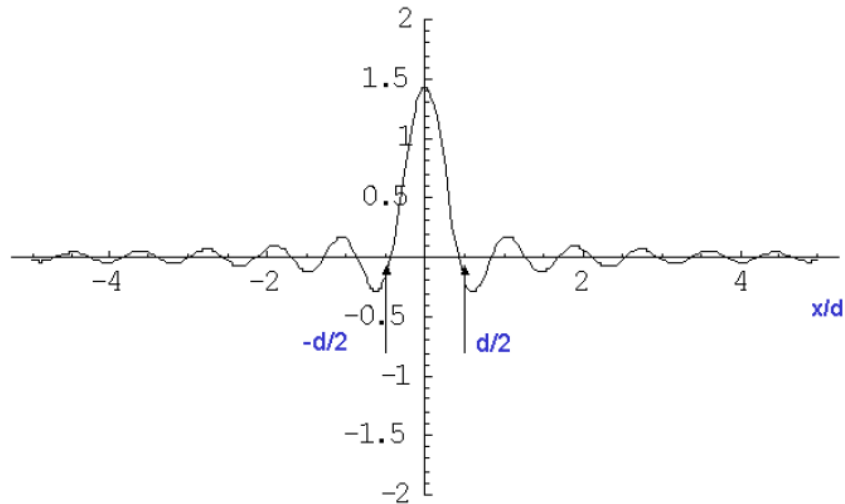


Figure 4.6: Composite diffractive evanescent wave lateral field profile at the $z=0$ boundary, a plot of Equation (4.13) [152].

4.5.2. The CDEW for an aperture with a periodic corrugation

Consider the periodic corrugation around a single aperture as shown in Figure 4.7(a). The corrugations are on both input and output surfaces and actually play a role as CDEW generating points. Each individual corrugation also becomes a radiating source.

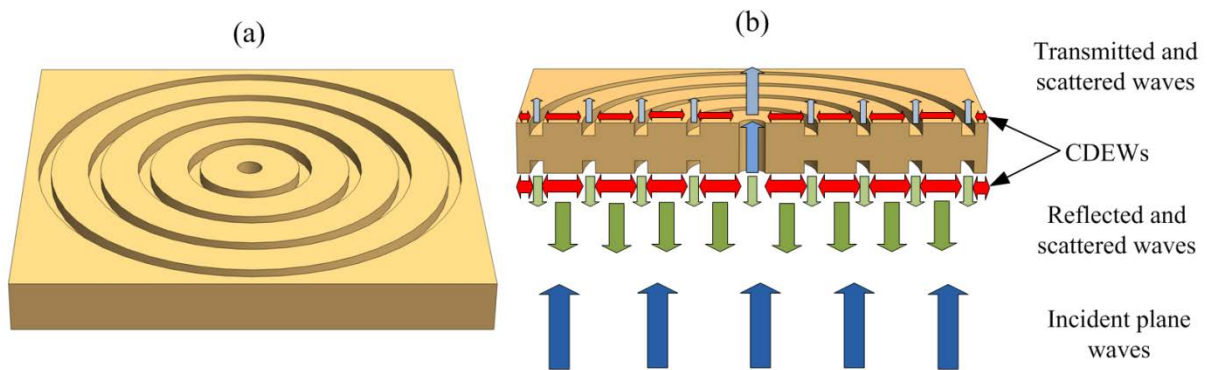


Figure 4.7: Schematic diagram showing: (a) a periodic corrugation around a single hole aperture; (b) the CDEW for an aperture with periodic corrugations on the input and output surfaces. Red arrows indicate the CDEWs generated on the input and output surfaces.

As is depicted in Figure 4.7(b), when a plane wave impinges on the periodically corrugated input surface with an aperture at the centre, only a small part of the incident light is directly transmitted through the aperture. Of the rest, part of incident light is directly reflected by the metal surface and part of the incident light is scattered by the corrugations. This scattering produces CDEWs on the input surface (red arrows). The CDEWs propagate on the input surface and are scattered by the corrugations. The corrugations on the input surface act as point sources for the scattered light which is radiating back to the space. Part of the CDEWs propagating on the input surface is scattered at the aperture and transmitted to the output surface along with the light directly transmitted through the aperture. When the transmitted light (directly transmitted light and CDEWs) arrives at the output surface, a small part of the light radiates directly into space and the rest of the light is scattered again by the aperture and corrugations on the output surface. The output surface CDEWs are now produced by the scattering of the transmitted light and it propagates on the output surface between the aperture and the corrugations. These propagating CDEWs on the output surface are scattered again by the corrugations and radiated into the front space. This means that each corrugation on the output surface also becomes a radiation source. Thus, the transmitted light can be observed

from all over the corrugation structure at the near field. At the far field, the radiation from the corrugations and the transmitted light from the aperture are superposed and interfere with each other. As discussed before, the CDEW has a $\pi/2$ -phase difference from the transmitted light. Therefore, the CDEWs and the directly transmitted light make an interference pattern. The interference pattern of these two waves at the far field has been observed experimentally, see [154].

4.5.3. The CDEW for an array of sub-wavelength apertures

The CDEW model for the periodic apertures array (Figure 4.8(a)) is similar to that of an aperture with periodic corrugations, except there are many apertures rather than one.

As depicted in Figure 4.8(b), a plane wave is incident on the input surface of a periodic aperture array. The incident wave is partially reflected, diffracted, and transmitted.

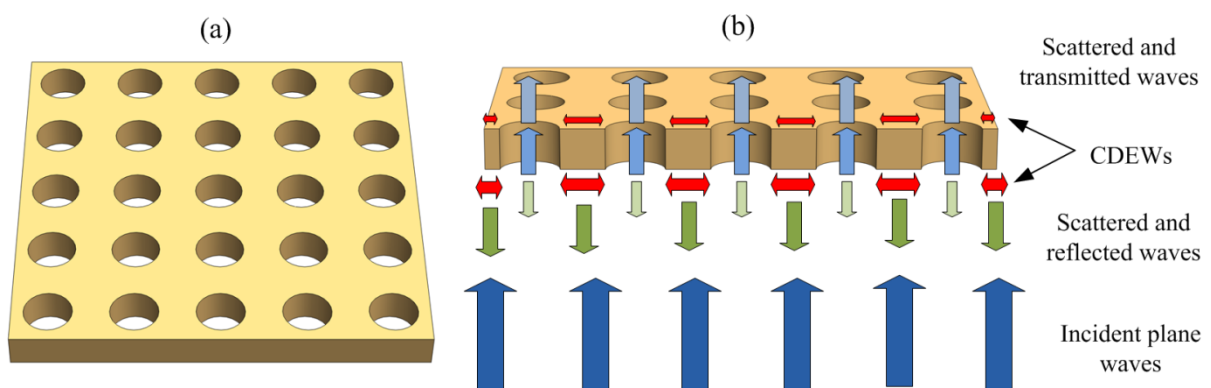


Figure 4.8: Schematic diagram of: (a) a 5 by 5 array of circular sub-wavelength apertures; (b) a CDEW for a periodic array of sub-wavelength apertures. Red arrows indicate the CDEWs generated on the input and output surfaces.

The reflected wave consists of a direct reflection by the metal surface and the back scattering from the aperture, similar to the case of the aperture with corrugations in the previous section. Like the corrugations in Figure 4.7(b), each aperture acts as a point for scattering and radiation of the CDEWs on the input surface. The CDEWs on the input surface are partially scattered back to space and partially transmitted along with the directly transmitted wave through the apertures to the output surface. Thus, the transmitted wave is a superposition of the CDEW and the wave directly transmitted through the apertures. When the transmitted light arrives at the output surface, it is partially scattered (generates CDEWs on the output

surface) and partially radiated into space. The CDEWs generated on the output surface propagate on the surface, and are partially scattered and radiated into space. In the front space, the directly transmitted wave from the apertures and the radiation from the CDEWs are superposed to be the total transmission of the aperture array for detection at the far field observation point .

4.6. Fano profile analysis

Genet *et al.* [133] proposed that the Fano line shape in transmittance of a periodic sub-wavelength aperture array is strong evidence of an interference between a resonant and a non-resonant process. Figure 4.9 shows schematic diagrams for the coupling of the resonant and non-resonant processes in a sub-wavelength aperture array. In Figure 4.9, the period of the array is a_0 , the thickness is h and the hole radius is r . As shown in this figure, there are two different scattering channels: one open channel ψ_1 corresponding to the continuum of states and one closed channel ψ_2 with a resonant state which is coupled to the open channel which is called “direct” or “non-resonant” scattering process. The other possible transition is that the input state transits to the resonant state (sometimes called quasibound state) of the closed channel and then couples to the open channel via the coupling term V . The “non-resonant” scattering process simply means the direct scattering of the input wave by the sub-wavelength hole array. This scattering can be called Bethe’s contribution. Bethe’s contribution is the direct transmission through the holes in the array which is proportional to $(d/\lambda)^4$ and will be detected as a background in transmittance. In contrast, the “resonant” scattering process is a contribution from the surface plasmon excitation. This resonant scattering process basically consists of two steps:

(1) the excitation of the surface plasmon on the periodic structure of metal surface by the input wave,

and

(2) the scattering of the surface plasmon wave by the periodic structure.

The surface plasmon wave can be scattered into free space (reflection) or into the nanoholes in the array (transmission). A simple transmission diagram of this model can be described via Figure 4.10. The total transmission amplitude is decided with the interference of the non-

resonant contribution (Bethe's contribution) and the resonant contribution (surface plasmon contribution).

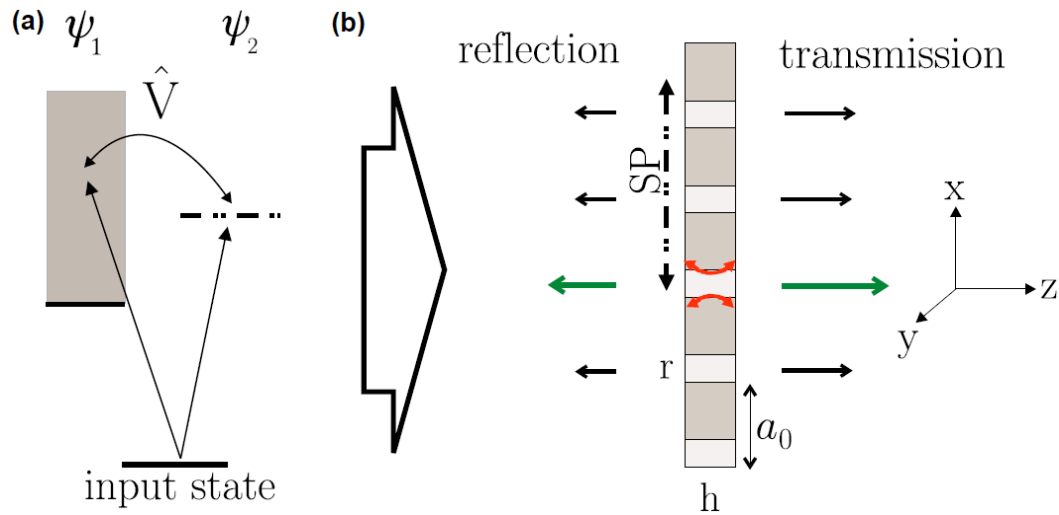


Figure 4.9: Schematic diagrams showing Fano profile analysis. (a) formal representation of the Fano model for coupled channels and (b) physical properties of the scattering process through the nanohole array directly (straight arrows) or via SP excitation [133].

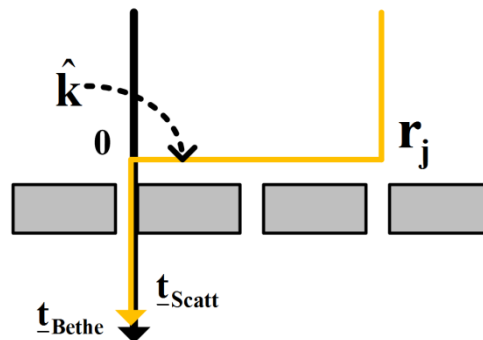


Figure 4.10: Schematic diagram of the non-resonant transmission (Bethe's contribution) and the resonant transmission (surface plasmon contribution) [156].

4.7. Fabry-Perot resonance on periodic arrays of sub-wavelength apertures

An array of cross-shaped structures [157] was employed to investigate the Fabry-Perot like cavity effect from the metallic structures due to the refractive index at the exits forming reflectors.

The model of the light propagating through these sub-wavelength aperture arrays can be described in three steps, (as follows):

Firstly, the impinge plane wave is trapped on the metal film as a localized surface plasmon by the sub-wavelength apertures; secondly, these localized surface plasmon polaritons (LSPPs) propagate in the sub-wavelength apertures; the process of surface plasmons propagating in these sub-wavelength apertures is as some SPs pass through them and some SPs are reflected back to the aperture at the exit surfaces, due to the RI difference of the aperture and that of the two surfaces of the metal film, therefore, the two surfaces of the metal can be viewed as two reflectors of the apertures, as a result, the sub-wavelength apertures of the metal film form Fabry-Perot like cavities; Finally, light emits from the other side of the metal film.

4.8. Types of metallic sub-wavelength apertures

As stated previously, many researchers have studied the transmission properties of sub-wavelength aperture arrays in metal films by changing the film material, film thickness, geometry symmetry, lattice constant, aperture size, and aperture shape, in the visible, near infrared, and terahertz range. Many interesting phenomena have been discovered and the underlying physical mechanisms have been explored. A considerable amount of literature has been published concerning the physics of light transmission through either a single sub-wavelength aperture or an array of sub-wavelength apertures in a metal film. Due to the scope of the subject, this section aims to provide a summary of various aperture shapes and the physical explanations which have appeared in the literature.

The first metallic sub-wavelength apertures that were investigated for the study of extraordinary optical transmission (EOT) were arrays of periodic circular or square apertures [8], as shown in Figure 4.11(a) and (b).

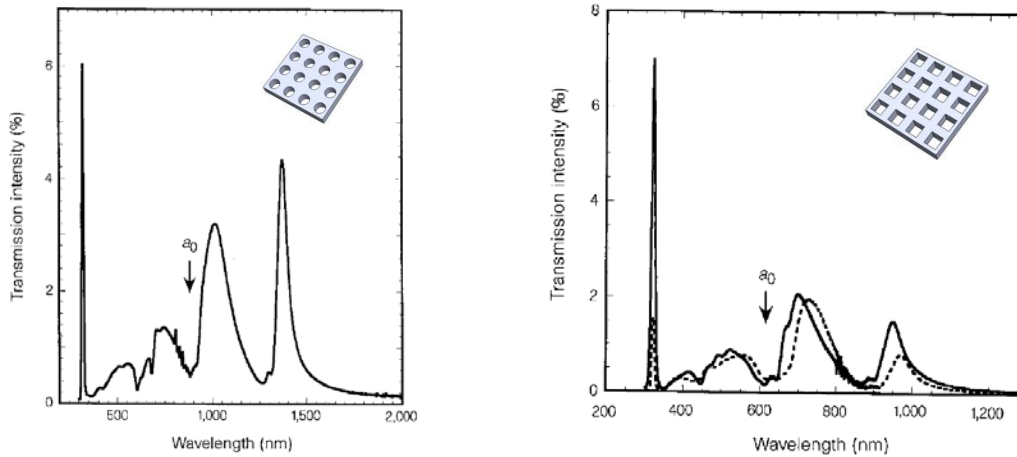


Figure 4.11: (a) Zero-order transmission spectrum of an Ag array. The lattice spacing a_0 was 900 nm, the nanoholes diameter was 150 nm and the thickness was 200nm. (b) Spectra for two identical Ag arrays with different thicknesses (Solid line: $t = 200$ nm; dashed line: $t = 500$ nm); for both arrays: period (a_0) = 0.6 μm ; diameter (d) = 150 nm. Images were taken from [8].

Figure 4.11(a) shows a typical zero-order transmission spectrum for an array of silver nanoholes with a diameter of 150 nm, a period a_0 of 900 nm and a 200 nm film thickness. The spectrum shows a number of distinct features. The narrow peak observed at $\lambda \sim 326$ nm comes from the bulk silver plasmons which disappears as the film becomes thicker. The remaining peaks originate from the transmission enhancement associated with the nanohole array. For a square array, the thickness dependence of the spectra is displayed in Figure 4.11(b) for 200 and 500 nm thick silver film. While the intensity of the bulk silver plasmon peak decreases rapidly in this range, that of the longer-wavelength peaks decreases approximately linearly with thickness.

Other sub-wavelength apertures, such as rectangular [158,159], triangular [160], annular [161-163], C-shaped [164], bowtie-shaped [165], I-shaped [166], cross-shaped [167-169], etc. have also been studied in a single aperture or an array of apertures. The distribution of electric field intensity for the single apertures are shown in Figure 4.12

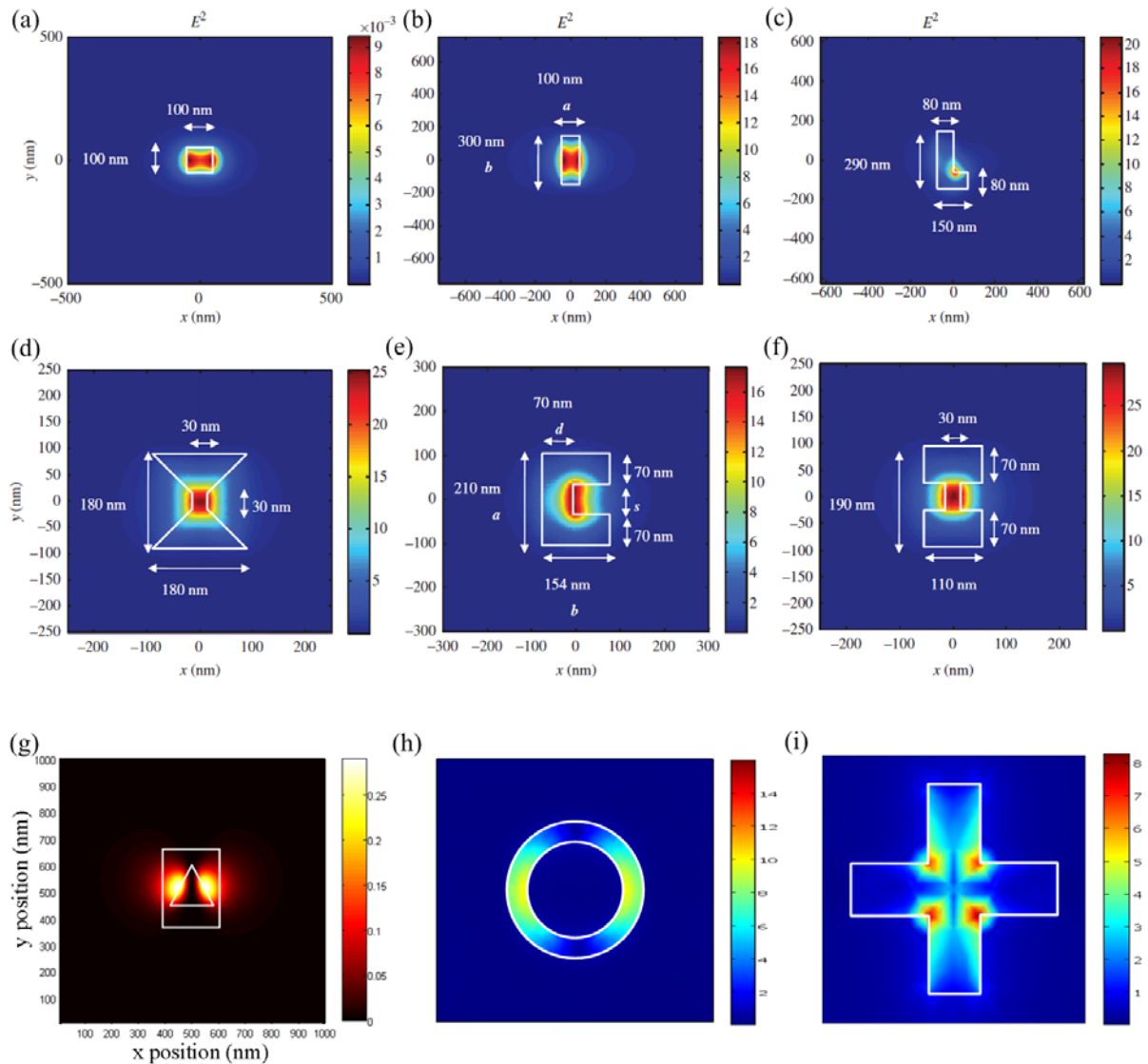


Figure 4.12: Distribution of electric field intensity around various apertures: (a) square, (b) rectangular, (c) L-shaped, (d) bowtie-shaped, (e) C-shaped, (f) I-shaped, (g) triangular, (h) annular, and (i) cross-shaped. Figures (a)-(f) were taken from [170] and (g) was taken from [160].

As pointed out by Lee *et. al.* [170] it is very difficult to compare the characteristics of the sub-wavelength apertures accurately for the following reasons: different aperture shapes, and the same aperture shapes with different parameters (i.e. length, width, etc.), have different longitudinal (z -directional, i.e. along the light propagation direction) locations for the beam minimum spot and peak intensity. Most of the studies in the literature assume free-standing metals with apertures but in reality the performance of these apertures change with factors such as the existence of a substrate, its thickness, dielectric constant, and the existence of

filling material within the aperture and its dielectric constant. Table 4.1 provides a summary of some sub-wavelength apertures reported recently. This table shows a good guideline concept on how much the light intensity can be enhanced. The power throughput is defined as the total power measured divided by the input power of a plane wave corresponding to the aperture cavity area. The power throughput should be larger than 1 for applications. The normalized peak intensity is the time-averaged maximum intensity of light at an appropriate point after the aperture, normalized to the input light intensity. For a more in depth discussion on the topic, readers can refer to [170].

Aperture	Wavelength (nm)	Metal Type	Power throughput	Normalized peak intensity	Ref.
Circular	700	Ag		>1	[144] ^a
Square	1000	PEC	0.0078	0.19	[164]
C	1000	PEC	4.41	36	[164]
Rectangular	780	Ag	4.5 - 4.7		[171]
Bow-tie	633	Au	1.3	801	[170]
L	633	Au		568	[170]
H	488	PEC	2.14	3.39	[172]

^aThis result is for an array of circular apertures, not for a single circular aperture.

Table 4.1: A summary of typical characteristic of single apertures reported. Au ≡ gold, Ag ≡ silver, PEC ≡ perfect electrical conductor.

In conjunction with the single sub-wavelength apertures, arrays of sub-wavelength apertures have also been studied. Wang *et. al.* [173] employed a cross-shaped array to study the interplay between surface plasmon polaritons (SPPs) and localized surface plasmon resonances as a promising photo-coupler for a GaAs quantum well photodetector. Arrays of rectangular, circular and trapezoidal apertures have been investigated recently for their influence on enhanced optical transmission [159]. An ultrasensitive label-free biodetection device achieved a figure of merit (refractive index sensitivity/the resonance width) as high as 162 with an array of circular apertures [174]. Listed in table 4.2 are some of the currently used arrays of sub-wavelength apertures in the literature and their details of investigation.

Aperture	Details of investigation	Ref.
Cross-shaped	A plasmonic coupler in optoelectronic devices.	[173]
Rectangular, circular and trapezoidal	Transmission peak and dip in the near-infrared wavelength.	[159]
Circular	Label free biodetection devices with figures of merits (FOMs) ~ 162.	[174]
Circular	SPR sensor - Sensitivity resolution of ~ 6.4×10^{-6} RIU.	[175]
Rectangular	Transmission spectra exhibit strong polarization-sensitive enhancement.	[176]
Annular	A colour filter - wavelength: visible regime	[163]
Annular	Localized surface plasmon resonance enhancement.	[177]

Table 4.2: A summary of currently investigated array of sub-wavelength apertures

Although there are indeed a variety of apertures that have been fabricated and tested it is believed that analysis of a limited set of aperture types can be relied on to adequately analyse the potential of the technique as applied to optical fibre sensors.

Consequently this thesis focused on cross-shaped, circular, annular and rectangular array of apertures.

Chapter 5. Numerical Modeling Techniques

5.1. Introduction

In order to fully appreciate the physics of extraordinary optical transmission and reflection in metallic sub-wavelength structures and how they could be embedded into the end-face of an optical fibre to get the best sensitivity, a systematic study was investigated. There are many parameters that may be varied, including the type of metal film and its thickness, the aperture shape, size and the periodicity of the array of apertures. It is not feasible to explore all possible combinations in a single thesis. However, with the help of the field of computational electromagnetics it is possible to make a significant contribution to our current knowledge. Numerical modeling is a fast and cost-effective method for designing metallic sub-wavelength structures and optimizing their performance. There are a number of different numerical approaches to explore optical transmission and reflection from the metallic sub-wavelength structures each with unique advantages and disadvantages. This chapter briefly describes and compares the two commercially available software that were used in this thesis, finite-domain time-difference FDTD (Lumerical FDTD) and finite element method FEM (COMSOL Multiphysics).

5.2. Finite-difference time-domain (FDTD)

The FDTD method solves Maxwell's time-dependent curl equations by initially converting them into finite-difference equations. The equations are then solved in a time-marching sequence by alternately calculating the electric and the magnetic fields in an interlaced spatial grid. The FDTD method was first proposed in 1966 by Yee [178] for the analysis of the scattering of an electromagnetic pulse by a perfectly conducting cylinder. It has since become a useful tool in electromagnetic waves, interference, radiation and surface plasmon modeling [179-186]. Recently, interest has been growing in applications of the technique to the analysis of dielectric optical devices [187-189]. The primary reasons for the expansion of interest in FDTD for solving Maxwell's equations can be summarized as follows [190]. FDTD:

1. Uses no linear algebra. Being a fully explicit computation, FDTD avoids difficulties with linear algebra.

2. Is accurate and robust. The sources of error in FDTD calculations are well understood, and can be bounded to permit accurate modeling for a very large variety of electromagnetic wave interaction problems.
3. Treats impulsive behaviour naturally. A single FDTD simulation can provide either ultra wideband temporal waveforms or the sinusoidal steady state response at any frequency within the excitation spectrum.
4. Treats nonlinear behaviour naturally. Being a time domain technique, FDTD directly calculates the nonlinear response of an electromagnetic system.
5. Is a systematic approach. With FDTD, specifying a new structure to be modeled is reduced to a problem of mesh generation rather than the potentially complex reformulation of an integral equation. For example, FDTD requires no calculation of structure-dependent Green's functions.

Computer memory capacities are increasing rapidly. While this trend positively influences all numerical techniques, it is of particular advantage to FDTD methods which are founded on discretizing space over a volume, and therefore inherently require a large random access memory (RAM). Computer visualization capabilities are increasing rapidly. This is an advantage to FDTD methods which generate time-marched arrays of field quantities suitable for use in colour videos to illustrate the field dynamics.

The FDTD method has been used in the solution of various problems and many publications are based on this method. This dissertation is also based on the FDTD method and the method has been used to solve Maxwell's equations in the time domain with constituting relations describing the sensitivity of a metallic sub-wavelength array embedded on an optical fibre end-face. In this section, the basics of the method are introduced so that the reader may be better equipped to appreciate the material presented in subsequent chapters. The details of the method can be found and studied from many other sources [190-192].

5.2.1. Finite difference approximation

The FDTD method is based on approximating the spatial and temporal derivatives by finite differences. The derivative of a function $f(x)$ at point x_0 (see Figure 5.1) can be approximated in different ways, for example:

$$\frac{df(x_0)}{dx} = f'(x_0) \approx \frac{f(x_0 + \Delta x) - f(x_0)}{\Delta x} \quad (5.1)$$

$$\frac{df(x_0)}{dx} = f'(x_0) \approx \frac{f(x_0) - f(x_0 - \Delta x)}{\Delta x} \quad (5.2)$$

$$\frac{df(x_0)}{dx} = f'(x_0) \approx \frac{f(x_0 + \Delta x) - f(x_0 - \Delta x)}{2\Delta x} \quad (5.3)$$

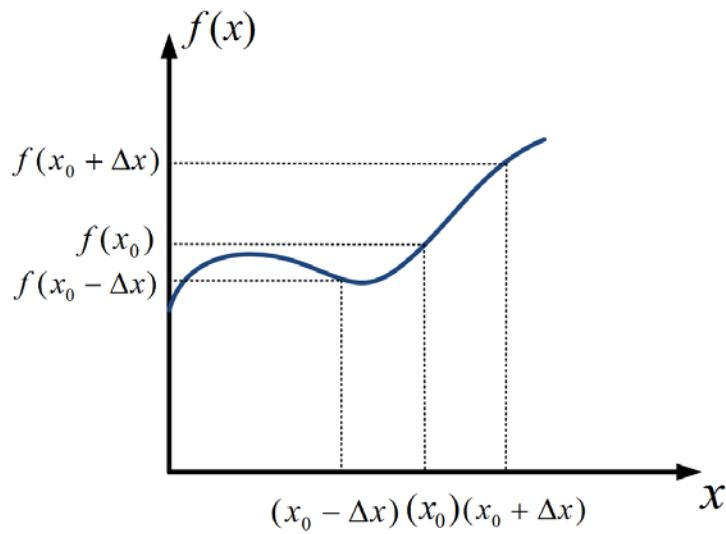


Figure 5.1: Function $f(x)$ at discrete points.

Equation (5.1) is the forward difference scheme while (5.2) is the backward difference scheme and (5.3) is the central difference scheme.

Considering the Taylor series expansions of $f(x + \Delta x)$ and $f(x - \Delta x)$,

$$f(x + \Delta x) = f(x) + \Delta x f'(x) + \frac{(\Delta x)^2}{2} f'' + \frac{(\Delta x)^3}{6} f''' + \dots \quad (5.4)$$

$$f(x - \Delta x) = f(x) - \Delta x f'(x) + \frac{(\Delta x)^2}{2} f'' - \frac{(\Delta x)^3}{6} f''' + \dots \quad (5.5)$$

and by taking the difference of Equations (5.4) and (5.5), and by dividing by $2\Delta x$, one obtains,

$$f'(x) = \frac{f(x + \Delta x) - f(x - \Delta x)}{2\Delta x} - \frac{\Delta x^2}{6} f'''(x) + \dots \quad (5.6)$$

The first term on the right side of Equation (5.6) is the central difference approximation to $f'(x)$ as given in Equation (5.3) and the other terms are the error between the approximation and the exact value of the derivative $f'(x)$. The error is proportional to the square of the finite difference Δx ; therefore the central difference scheme is considered *second order accurate*. In a similar manner, it can be shown that the forward difference and backward difference schemes are *first order accurate*. While it is possible to obtain and use more accurate schemes, the second order accurate central difference scheme is sufficiently accurate to use in most of the practical electromagnetic (EM) applications.

5.2.2. The Yee cell

The first step in the construction of an FDTD algorithm is the discretization of the computation space into cells and definition of the locations of the electric and magnetic field vectors on each cell. Yee [178] developed an algorithm in which the electric and magnetic field vector components are located in a staggered fashion as shown in Figure 5.2. In each cell, three electric field vectors and three magnetic field vectors are defined. Electric and magnetic fields are not defined at the same locations. The magnetic field components are located at the centres of the faces and are normal to the faces. The electric field components are located at the centres of the edges and are parallel to the edges. This special configuration depicts Faraday's Law and Ampere's Law. In Figure 5.2, it can be seen that electric field vectors are forming loops around magnetic field vectors, simulating Faraday's Law; and magnetic field vectors are forming loops around electric field vectors, simulating Ampere's Law.

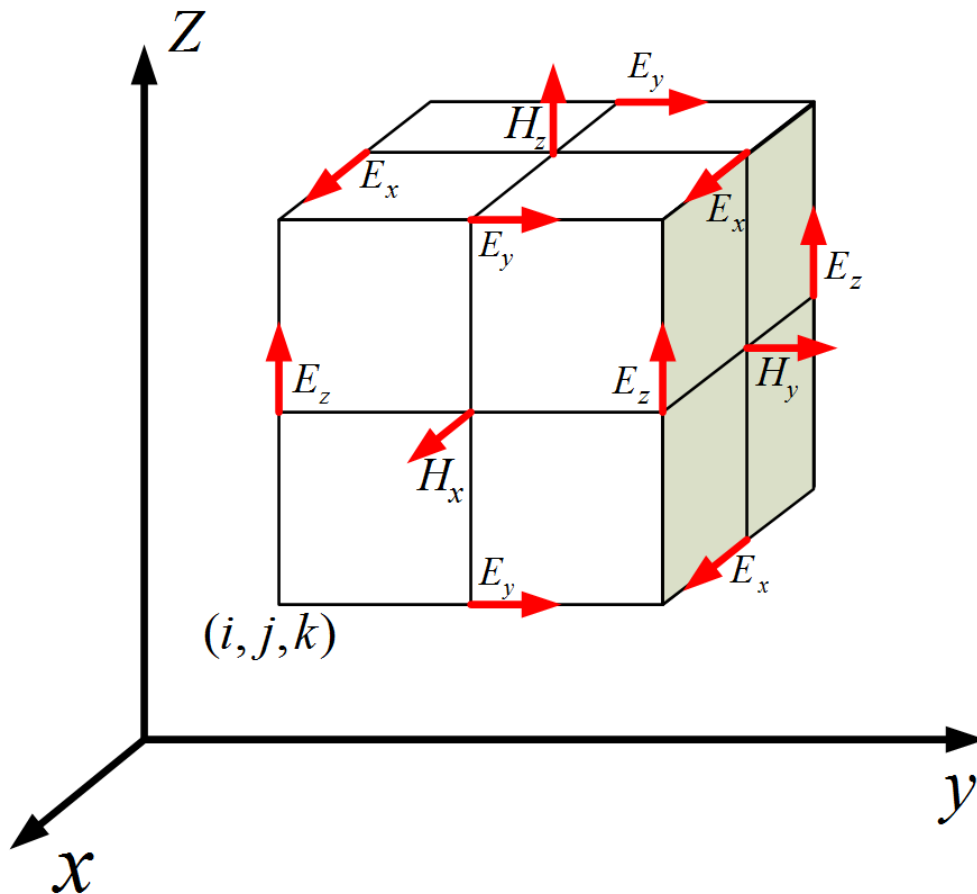


Figure 5.2: Positions of the electric and magnetic field vector components on a cubic unit cell of the Yee space lattice.

The FDTD algorithm is based on the computation of the electric and magnetic field values at every cell in the computation space iteratively in time. At every iteration time step, six new values of field vectors are calculated at every cell. In the Yee algorithm electric and magnetic fields are offset not only in space but also in time as the electric fields and magnetic fields are not calculated at the same time instant. If electric fields are calculated at time instant $2\Delta t$ then magnetic fields will be calculated at time instant $(l + 0.5)\Delta t$ where l is the time step iteration index and Δt is the duration of a time step. This is why this algorithm is called a *leap-frog* algorithm. This entire process of iterations fits to the equations when the second order accurate central difference scheme is used to discretize the time and space derivatives in Maxwell's curl equations. For more details of the FDTD method, readers can refer to [190-192].

5.2.3. Lumerical FDTD solutions

Lumerical FDTD SolutionsTM is a commercially available software package [193]. It provides a state-of-the-art method for solving Maxwell's equations in complex geometries. It is a fully vectorial method that naturally gives both time domain, and frequency domain information to the user, offering unique insight into all types of problems and applications in electromagnetics and photonics. Lumerical FDTD solutionsTM method is discrete in both space and time. The electromagnetic fields and structural materials of interest are described on a discrete mesh made up of so called-Yee cells. Maxwell's equations are solved discretely in time, where the time step used is related to the mesh size through the speed of light.

Structures to be simulated can have a wide variety of electromagnetic material properties. Lumerical FDTD solutionsTM is used to calculate how the electromagnetic fields propagate from the source through the structures. Subsequent iterations provide the electromagnetic field propagation in time. Typically, the simulation is run until there are essentially no electromagnetic fields left in the simulation region. More detailed information about Lumerical FDTD solutionsTM can be found in reference [193].

5.3. Finite element method (FEM)

The finite element method (FEM) or finite element analysis (FEA) is fundamentally a method for obtaining a numeric approximation to a governing differential equation, subject to prescribed boundary conditions, over some geometric domain [194-196]. The domain is divided into a finite number of smaller non-overlapping regions referred to as elements. All of the elements taken together completely cover the domain of interest like the pieces of a puzzle. Historically, the division of a domain into discrete elements to solve problems in elasticity began with Argyris *et al.* [197] and Turner *et al.* [198]. Since then, the finite element method has continued to evolve, driven by increasingly powerful computers, and the application of the technique to an ever broadening range of scientific and engineering problems.

Each element contains some number of points referred to as nodes. For example, a 2D problem may use triangular elements, and each element will have at least three nodes, corresponding to the vertex points of the triangle. The elements and nodes together are referred to as the mesh. The dependent variable is approximated over each element by some interpolating function, generally a polynomial. The number of nodes in each element must be

equal to the number of parameters to be determined in the interpolating function, so more may be added if necessary. More details regarding the mathematical details of FEM can be found in [199].

5.3.1. Comsol Multiphysics

Comsol MultiphysicsTM is also a commercially available software package, which evolved from the FEMLABTM finite element analysis tools. It provides a CAD interface to define the geometry, a sophisticated mesh generation capability, and a wide array of numeric solver and post-processing tools.

In addition to its general partial differential equation (PDE) solver capability, Comsol offers application specific modules, each tailored to solving specific types of physics and engineering problems including Chemical Engineering, Acoustics, Earth Science, and many others. The modules in turn contain application modes, which specify the form of the governing PDE to be solved, and allow the user to specify all coefficients, boundary conditions, and initial conditions. The coefficients may be functions of the spatial coordinates, functions of the dependent variable for which one is solving, or in the case of a multi-physics model dependent on the output of another coupled application mode.

The application specific module used for this study is the radio frequency (RF) Module. This module offers many different application modes, each of which formulates its governing PDE based on Maxwell's equations and the equation of continuity. More details of Comsol MultiphysicsTM 3.5a RF module can be found in [200].

5.4. Lumerical FDTD solutionTM versus Comsol MultiphysicsTM

All computational methods have drawbacks. For example, in all time-domain methods, one of the most important issues is the technique used to approximate time derivative equations. This approximation is responsible for the accuracy of the numerical solution as it evolves in time. Developing high accuracy approximations to these derivatives is challenging, because mathematically better approximations often end up degrading the physical solution, such as dissipating of the energy density of an electromagnetic wave in free space.

In order to decide which method is suitable for modeling of the sensor application in this thesis, one should verify results obtained from Lumerical FDTD solution and Comsol Multiphysics numerical methods with that of the analytical theory presented in Section 4.2.

Consider the end-face of a gold-coated optical fibre, Figure 5.3(a). The simulation geometry in which an optical wave is incident on an optically thick (i.e. ~ 180 nm) metallic gold film where it transmits through the z-direction is shown in Figure 5.3(b).

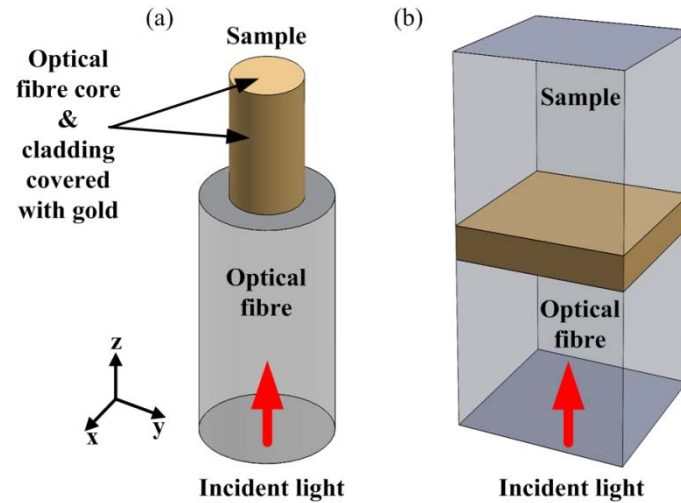


Figure 5.3: (a) An illustration of an incident plane wave travelling through an optical fibre to a flat gold film layer, and (b) the equivalent simulation set-up.

From the analytical theory shown in Chapter 4, the transmission peak positions, λ_{\max} , at normal incidence for light interacting with a gold metal layer is calculated to be approximately 500 nm. This is simply the optical properties of the gold layer and is not related to any structures that might be used as will be discussed in the subsequent Chapters. This result has also been confirmed by Dhawan *et al.* [13] and McMahon *et al.* [201]. To verify this value with the numerical modeling techniques with the RI of sample and fibre core were taken as air ≈ 1 and glass ≈ 1.5 , respectively. The results obtained from the simulations are shown in Figure 5.4(a) and Figure 5.5(a). These results reveal the difference between λ_{\max} calculated by Comsol Multiphysics and Lumerical FDTD solutions is nearly 100 nm. The reflection spectra seen in conjunction with these transmission peaks of the two techniques are also different, as shown in Figures 5.4(b) and 5.5(b). A possible reason for this discrepancy in the two techniques is the database of the Comsol Multiphysics package does not provide materials properties as a function of wavelength. To calculate the plasmonic properties of a gold material, one would manually use the data from an appropriate reference such as [79]. Figures 5.6(a) and (b), are the transmission and reflection spectra resulting from a 180 nm thick layer of gold placed on the end-face of a multimode fibre having a core diameter of 62.5 μm . Comparing this with the results from the FDTD and COMSOL

simulations supports the use of FDTD technique, particularly for use at around this wavelength region.

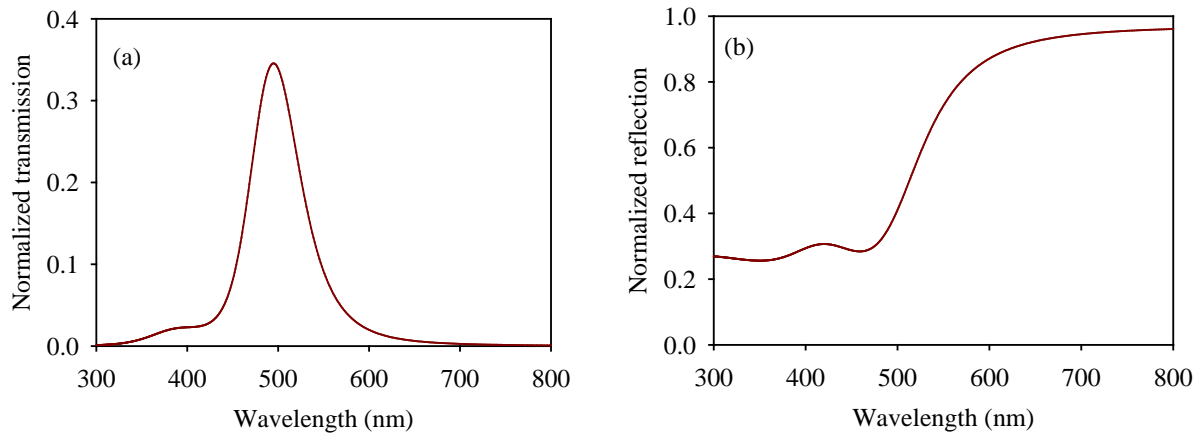


Figure 5.4: FDTD calculations of (a) transmission and (b) reflection of a flat (180 nm) thin gold film on an optical fibre end-face.

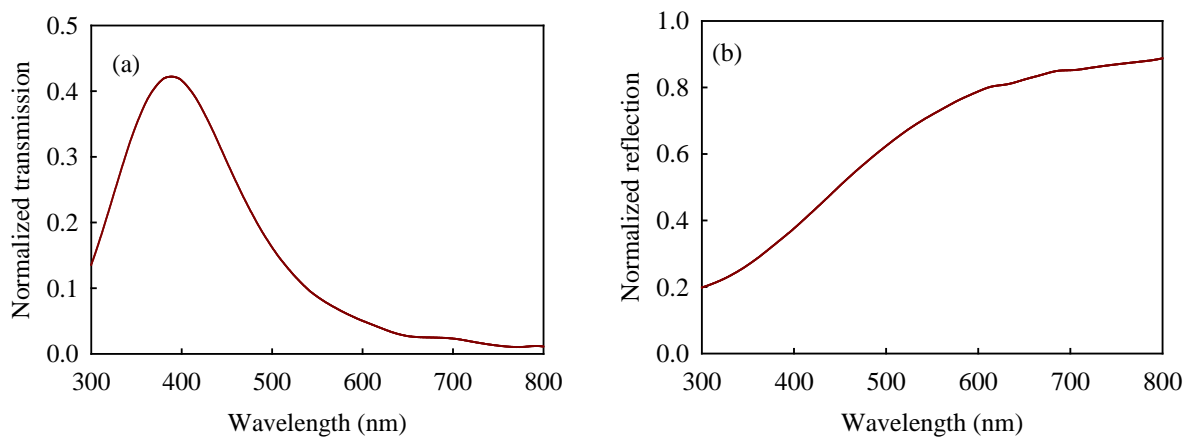


Figure 5.5: Comsol (FEM) calculations of (a) transmission and (b) reflection of a flat (180 nm) thin gold film on a optical fibre end-face.

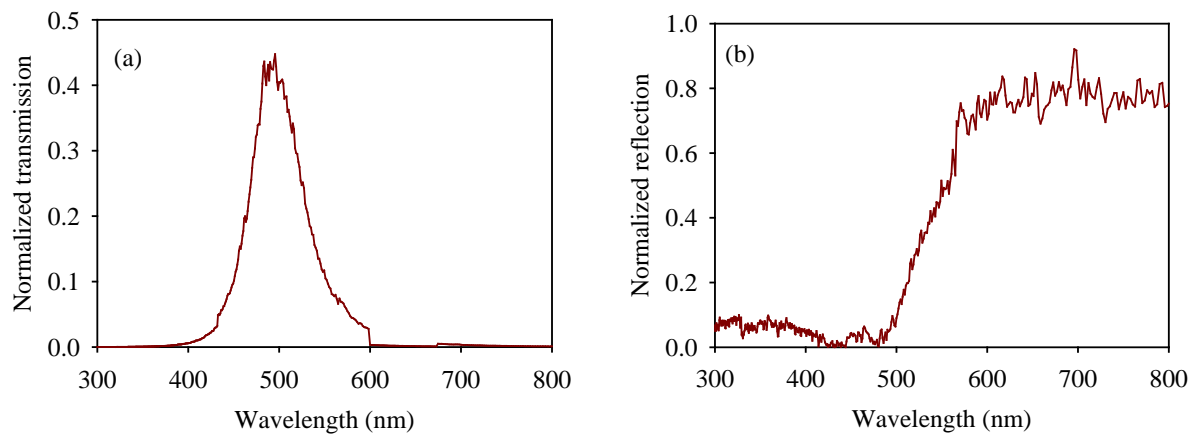


Figure 5.6: Measured (a) transmission and (b) reflection of a layer (180 nm) thin gold film on multimode fibre end-face

There are many advantages that Lumerical FDTD solutionsTM has to offer. One is that it has a simple, and straightforward formulation, as outlined in Section 5.2. Perhaps the biggest advantage is its applicability to a wide range of problems; any structure can be modeled by simply specifying ϵ (permittivity) and μ (permeability) over a computational domain which is periodic or non-periodic, and arbitrary incident fields can be easily inserted into the simulations. Because of these advantages, FDTD is preferred and therefore has been used to model a reflection-based sensor that includes as integrated an array of metallic sub-wavelength apertures on the end-face of an optical fibre.

Chapter 6. Fabrication and Experimental Techniques

6.1. Introduction

Various experimental data showing the measurement of the RI using a multimode optical fibre surface plasmon resonance sensor based on a metallic array of sub-wavelength apertures show a shift features in optical transmission spectra [13,202,203]. The shift in the optical transmission wavelength peaks is a result of change in the index of refraction of the liquid solution. This chapter adopts both an analytical solution and the FDTD approach to simulate an optical transmission-based setup used in the experiments. The FDTD technique is also used to explore the shift in optical reflection spectra for a reflection-based sensor used in the experiments.

It is considered important to establish the reliability of the simulation technique used against experimental data, thereby enabling the simulations to explore the likely sensitivity of a range of possible designs and configurations without the need for countless arrays to be fabricated and tested.

6.2. Transmission-based configuration

The OFS configuration assumed in this section is similar to the OFS explored in three previous studies [13,202,203], as shown schematically in Figure 6.1. Optical transmission measurements were performed by using a white light source (300 - 800 nm) that was focused onto the fibre end-face. The sensing part (**C**) was placed inside the sensor chamber specifically fabricated for the transmission experiments and allowing liquids of various RI to fill the chamber. The optical transmission was collected by a collector fibre (**D**) that was aligned to the gold-coated fibre end-face with a space, approximately 300 μm between the fibre end-faces.

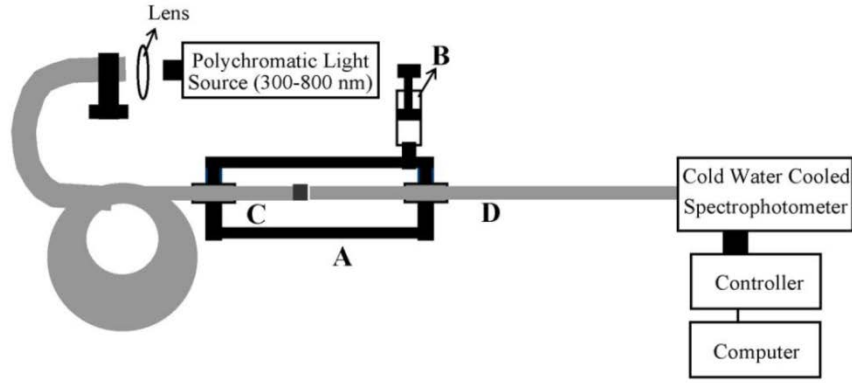


Figure 6.1: Schematic of the setup employed for evaluation of the spectrum of the array of nanoholes in a transmission-based configuration which included a sensor chamber (A), a liquid injection system (B), a sensing fibre (C), and a collecting fibre (D)[13].

6.2.1. Analytical solution

The analytical theory from Section 4.2 and Section 5.4 of this thesis show the transmission peak positions, λ_{\max} , at normal incidence for light interacting with a gold metal layer is calculated to be approximately 500 nm. The Equation (4.7) governing this result is

$$\lambda_{\max} = \frac{P}{\sqrt{i^2 + j^2}} \sqrt{\frac{\epsilon_d \epsilon_m}{\epsilon_d + \epsilon_m}}.$$

6.2.2. FDTD simulation

To simulate the optical properties of the FIB fabricated metallic nanostructure arrays on the fibre end-face, electromagnetic simulations using commercial FDTD software (Lumerical FDTD Solution Inc., Canada) [193] were carried out. The dimensions of each metallic nanostructure array are set the same as those in the actual experiments [13]. The array is taken as a 24 by 24 nanohole array. The diameter of the circular nanohole and the thickness of the gold layer are taken as 200 and 180 nm. The periodicities between the nanoholes are taken as 400 and 600 nm. According to the experiment in [13], the diameter of the fibre core is taken as 100 μm .

In FDTD Solutions, a unit cell (periodic unit) is a representation of an infinite array, as shown in Figure 6.2. This allows the use of a large array in the analysis and reduces the computation time. A noteworthy aspect of FDTD Solutions is its ability to perform parallel computation on multiple cores, multiprocessors and clusters. This enables large-scale and rapid simulation

of optical components, by distributing computational load and memory requirements. The FDTD Solutions package also offers an integrated scripting environment to customize simulation and analysis for design automation, and a movie generation feature for recording simulation field/intensity dynamics.

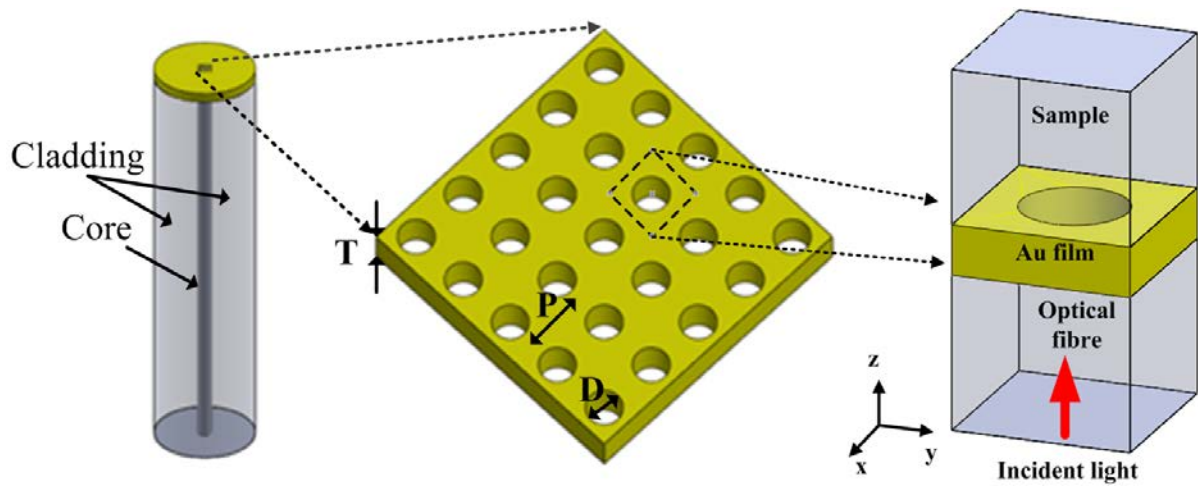


Figure 6.2: An interpretation of a unit cell used in FDTD Solutions.

Figure 6.3 shows a screen shot of a unit cell of the considered sensor simulated under FDTD Solutions. The script file which calculates the transmission spectra is located in Appendix A.

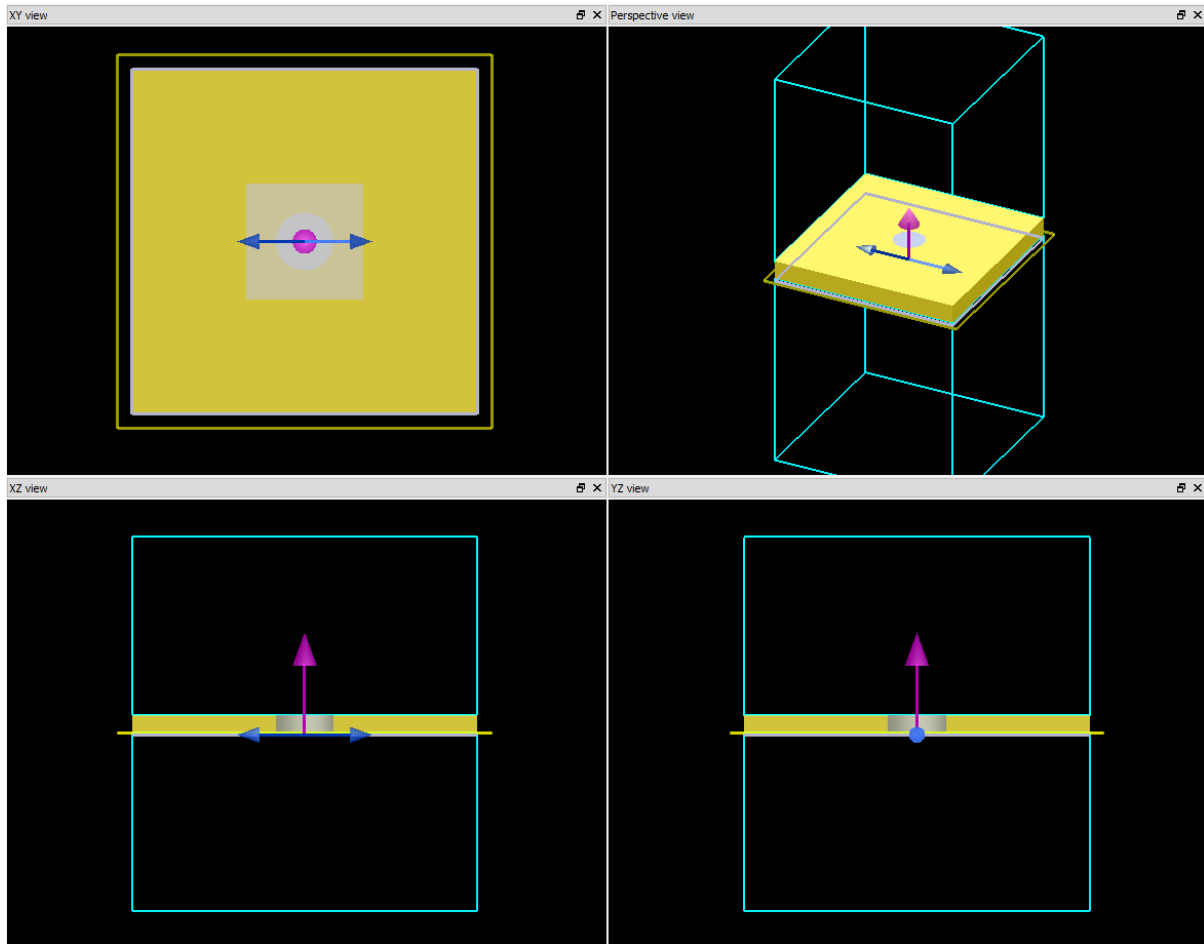


Figure 6.3: Screen shot from the FDTD Solutions of a unit cell of an array of circular nanoholes with periodicity of 600 nm in a 180 nm thick gold layer. The four individual frames depicted in the screen shot show (left to right, top to bottom), XY plane, Perspective view, XZ plane and XY plane.

The simulation settings were:

- minimum mesh step = 0.25 nm,
- maximum mesh step = 5 nm,
- mesh accuracy = 5,
- mesh type = auto non-uniform,
- boundary conditions = periodic for sides and perfect match layer (PML) for top and bottom layers,
- default dielectric properties of gold.

As stated above, a unit cell is a representation of an infinite array in the simulation and that a 24 by 24 nanohole array may be considered infinitely periodic with respect to one nanohole. Therefore, the transmission focused solely on the effects of the nanohole. However, there is an issue in the experiment as the 24 by 24 nanohole array covers an area of $207.4 \mu\text{m}^2$ (for periodicity = 600 nm), which is only a small fraction of the fibre core's $7854 \mu\text{m}^2$ (100 μm diameter). Thus, in order to calculate the response from the entire fibre core, the effect of the nanohole and the effect of the gold are scaled according to their relative area. Therefore, a more accurate method of simulation would be to run two simulations, one with the nanohole and one without the nanohole. Then the results would be added together with the correct area weighting factors. For example, $\left(\frac{207.4 \times 100}{7854}\right) = 2.64\%$ of the core's area covered by the nanoholes and $(100\% - 2.64\%) = 97.36\%$ covered by the gold for the case of the 600 nm periodicity above.

6.2.3. Experimental and simulation results comparison

The experimental transmission spectra taken from [13], are shown in Figure 6.4(a) and (b) for two different periodicities, 400 and 600 nm. The simulated transmission spectra are shown in Figure 6.5(a) and (b) for 400 and 600 nm period, respectively.

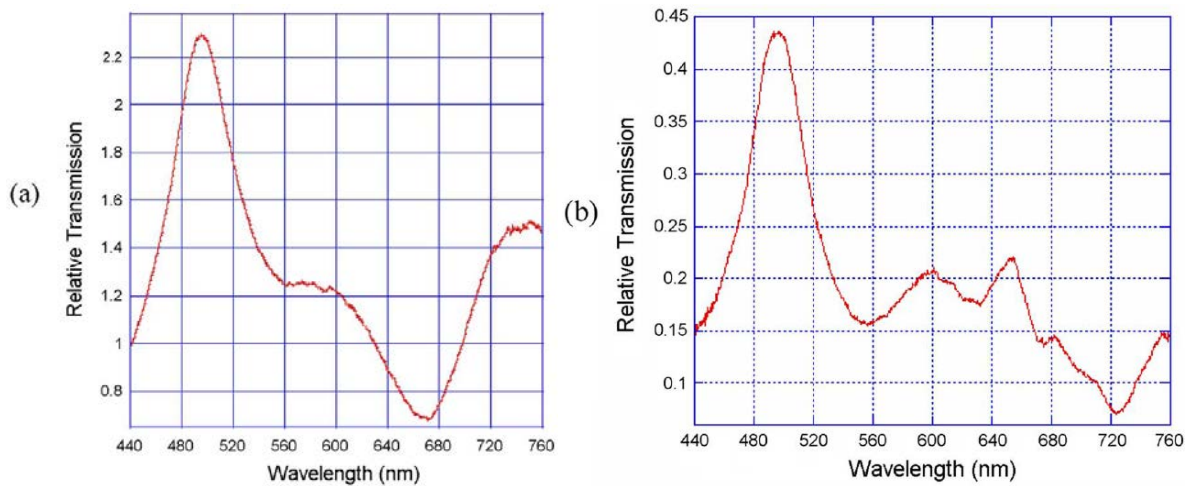


Figure 6.4: Measured transmission spectra of a 24 by 24 circular nanohole array in a gold film on the end-face of a multimode optical fibre, having a 100 μm core. The thickness of the gold film was 180 nm. The diameter of each nanohole was 200 nm. The spacing (periodicity) between the nanoholes was (a) 400 and (b) 600 nm. Graphs were taken from [13].

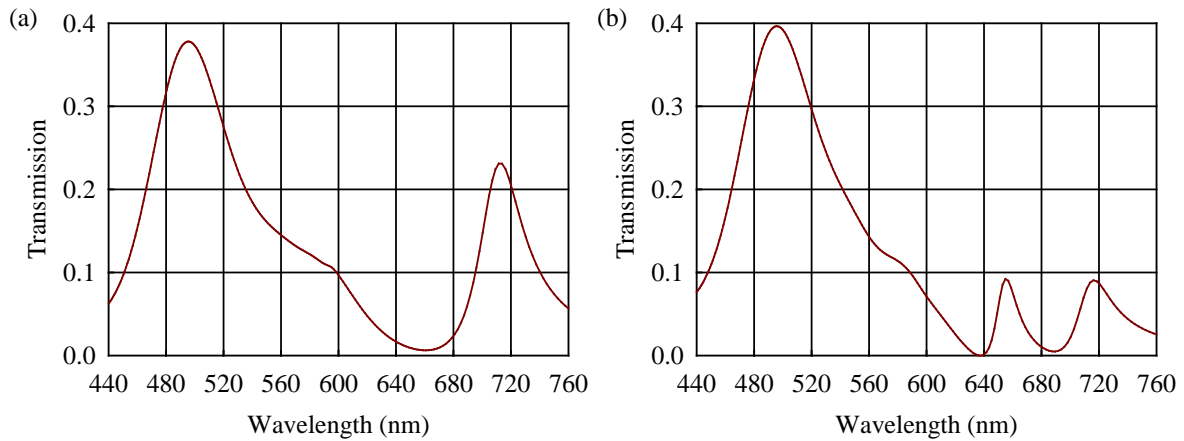


Figure 6.5: FDTD simulated transmission spectra of a 24 by 24 circular nanohole array in a gold film on the end-face of a multimode optical fibre, having a 100 μm core. The thickness of the gold film was 180 nm. The diameter of the nanohole was 200 nm. The periodicity between the nanoholes was (a) 400 and (b) 600 nm.

For a periodicity of 400 nm, Figures 6.4(a) and 6.5(a) display a broad maxima near $\lambda = 500$ nm. For periodicity of 600 nm, Figures 6.4(b) and 6.5(b) also display a peak at ~ 500 nm. This peak occurs due to electron transitions between the d-bands of gold and the Fermi level in the conduction band [204]. This peak is characteristic of the gold film layer and is not related to any nanohole or array properties [201,205]. The peak at ~ 660 nm in Figures 6.4(b) and 6.5(b) can be attributed to a combination of a localized surface plasmon resonance in each hole and the (1, 1) scattering order with optical fibre (silica) as the medium next to the gold film. The agreement between simulations and measurements is quite good, the only discrepancy being a small difference in the transmission resonance strength. As for the purpose of designing a reflection-based sensor in this thesis, the resonant dip is an important parameter to be considered in the testing of a liquid RI. Therefore, one can consider the results of the simulations to be sufficiently equivalent to experiments.

6.3. Reflection-based configuration

As analyzed above, a single mode fibre is the preferred choice when it comes to fabrication as it has smaller core size. Therefore the time taken to mill the arrays onto the gold-coated fibre end-face is greatly reduced. In this section and subsequent sections, single mode optical fibres are to be considered. The experimental setup of a reflection-based configuration is

shown in Figure 6.6. A sensing fibre is connected to one side of a standard 2×1 single mode optical fibre coupler. A tungsten halogen light source (HL-2000, wavelength range: 360 nm - 2000 nm, Ocean Optics) and an optical spectrum analyzer OSA (AQ-6317B, resolution 10 pm, Ando) are connected to the other two coupler ends. Light is coupled via the coupler into the fibre device, where it interacts with the nanohole array. The reflected spectrum, modified by the array, is detected by the OSA. To investigate the effect of changing the RI of the medium surrounding the fibre end-face, distilled water, acetone and iso-propyl alcohol solutions were prepared for the measurement.

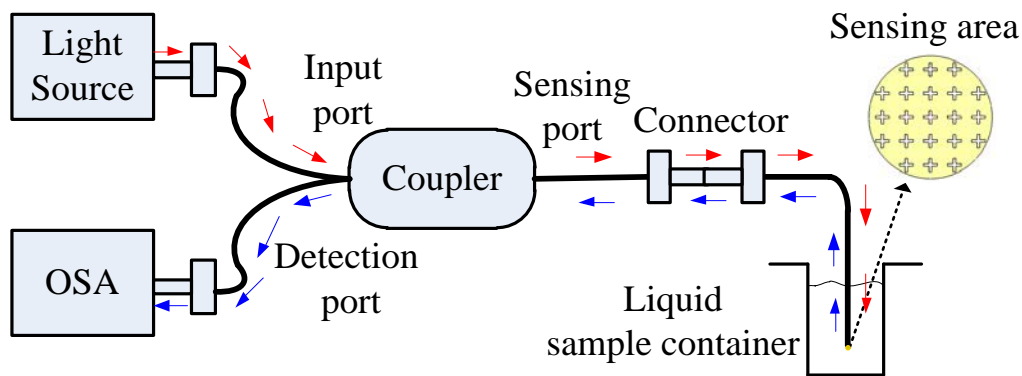


Figure 6.6: A reflection-based OFS experimental setup for determining RI.

6.3.1. Simulation

To simulate for the reflection spectra of the FIB fabricated cross-shaped array on the fibre end-face, electromagnetic simulation was carried out using FDTD. The simulation for a reflection-based sensor was similar to the transmission-based sensor above. The incident light is a plane wave propagating along the z-direction. Periodic boundary conditions were implemented on the sides and perfectly matched layers were used to eliminate reflections at the upper and lower surfaces. A unit cross-shaped simulated structure and the electric field around the cross-shaped are shown in Figures. 6.7(a) and (b). The reflected power was determined by integrating the z-component of the Poynting vector over the lower surface. Values were normalized to the incident power. All settings were the same as the transmission-based sensor except the script file which calculates the reflection spectra was different and is located in Appendix B.

Figure 6.8 shows a screen shot of the of a unit cell of the considered sensor simulated under FDTD Solutions.

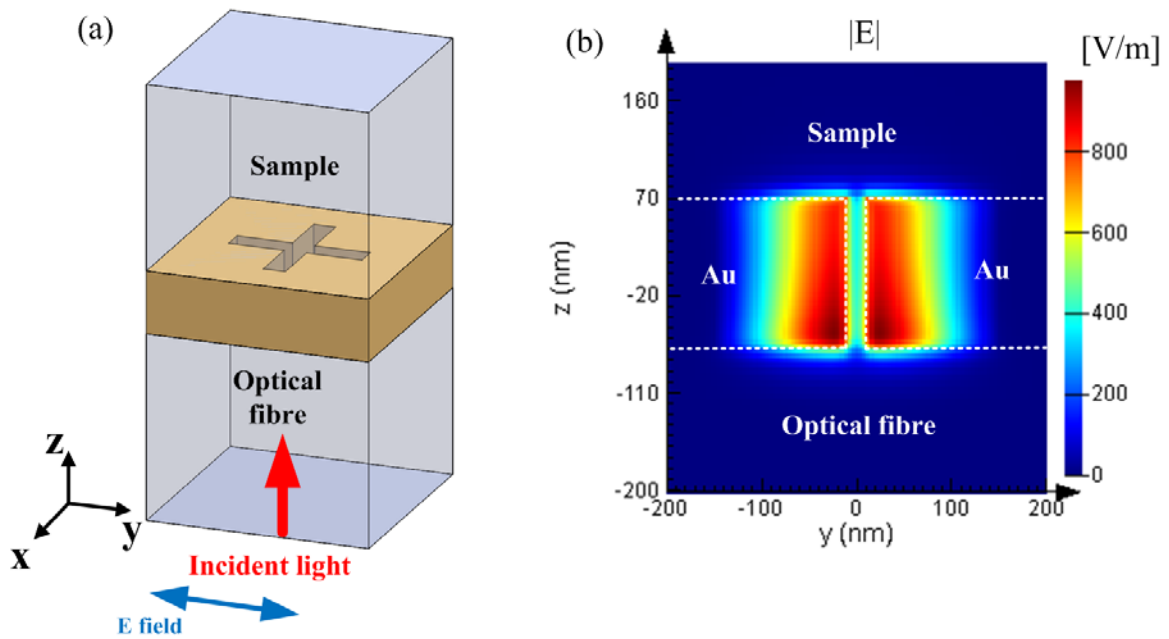


Figure 6.7: (a) The cross-shaped structure simulated in FDTD; (b) The intensity of the electric field around the cross-shaped: the cross-shaped is centered at the origin and the film boundaries are outlined in dashed lines.

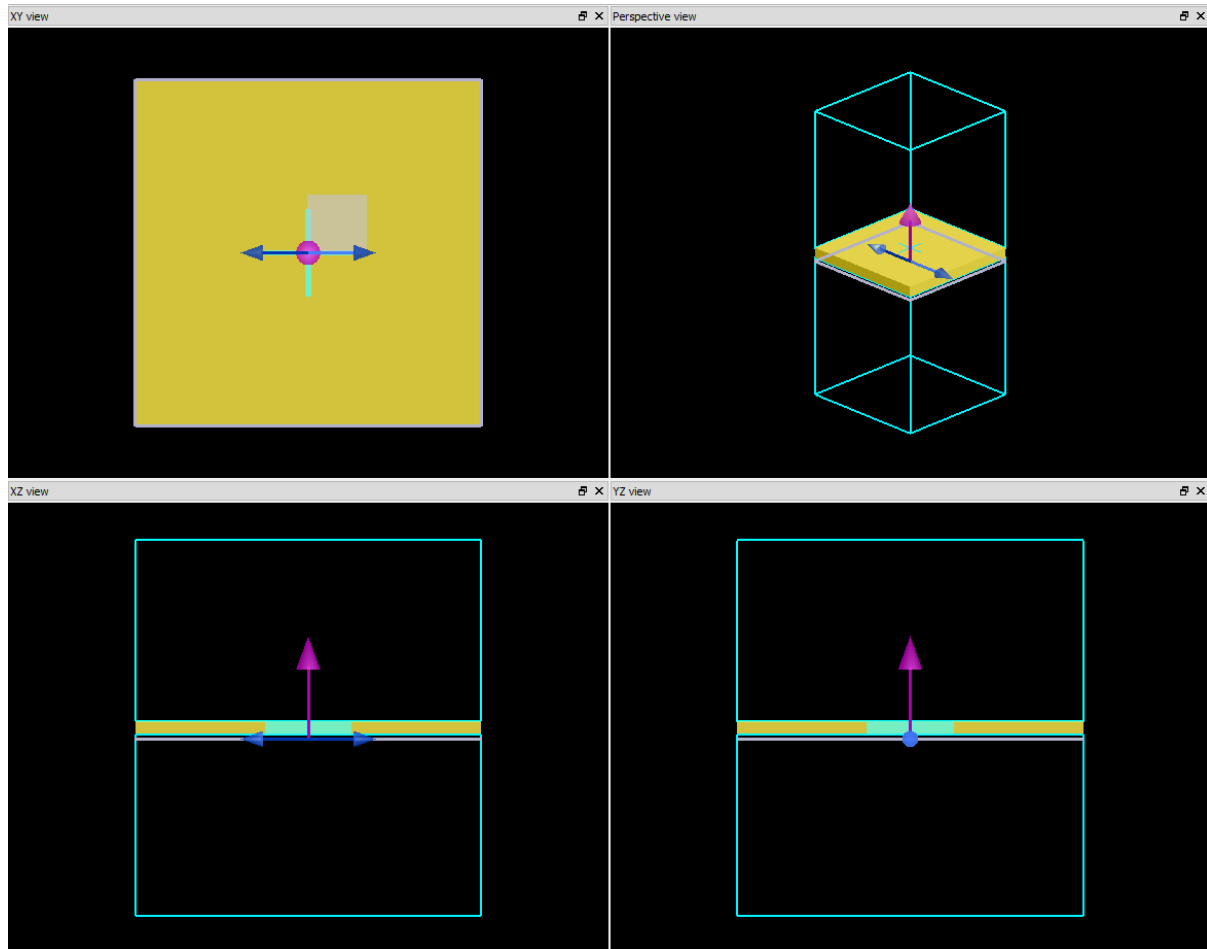


Figure 6.8: Screen shot from the FDTD Solutions of a unit cell of an array of cross-shape apertures with periodicity, width and length of 400, 20 and 300 nm, respectively, in a 140 nm thick gold layer. The four individual frames depicted in the screen shot show (left to right, top to bottom), XY plane, Perspective view, XZ plane and YZ plane.

6.3.2. Fabrication

There is evidence from the literature [201-203] that if the direct Au sputtering process was performed correctly, and the samples were situated properly in the focused ion beam chamber, issues such as distortion of the etched parameters can be avoided.

The fabrication process for an optical fibre surface plasmon resonance sensor based on an array of metallic sub-wavelength apertures includes the following steps:

Step 1. Preparing optical fibres for fabricating

The standard single mode optical fibres employed in this study were obtained from Australian Fibre Works (AFW) Technologies and had a 8 μm core and a 125 μm cladding

diameter. The fibre end-face was prepared by stripping the outer jacket, which was followed by cleaving the fibre end-face perpendicularly to obtain a flat end-face with a commercial handheld fibre cleaver. The fibre end-face was then cleaned with isopropyl alcohol to achieve a smooth mirror-like surface.

Step 2. Placing optical fibres into a special fibre holder

To form metallic nanostructures on the optical fibre end-faces, a special fibre holder that can be used in the gold depositing process and fitted in the focused ion beam (FIB) mounting-stage was fabricated by using the stainless steel material, as shown in Figure 6.9.

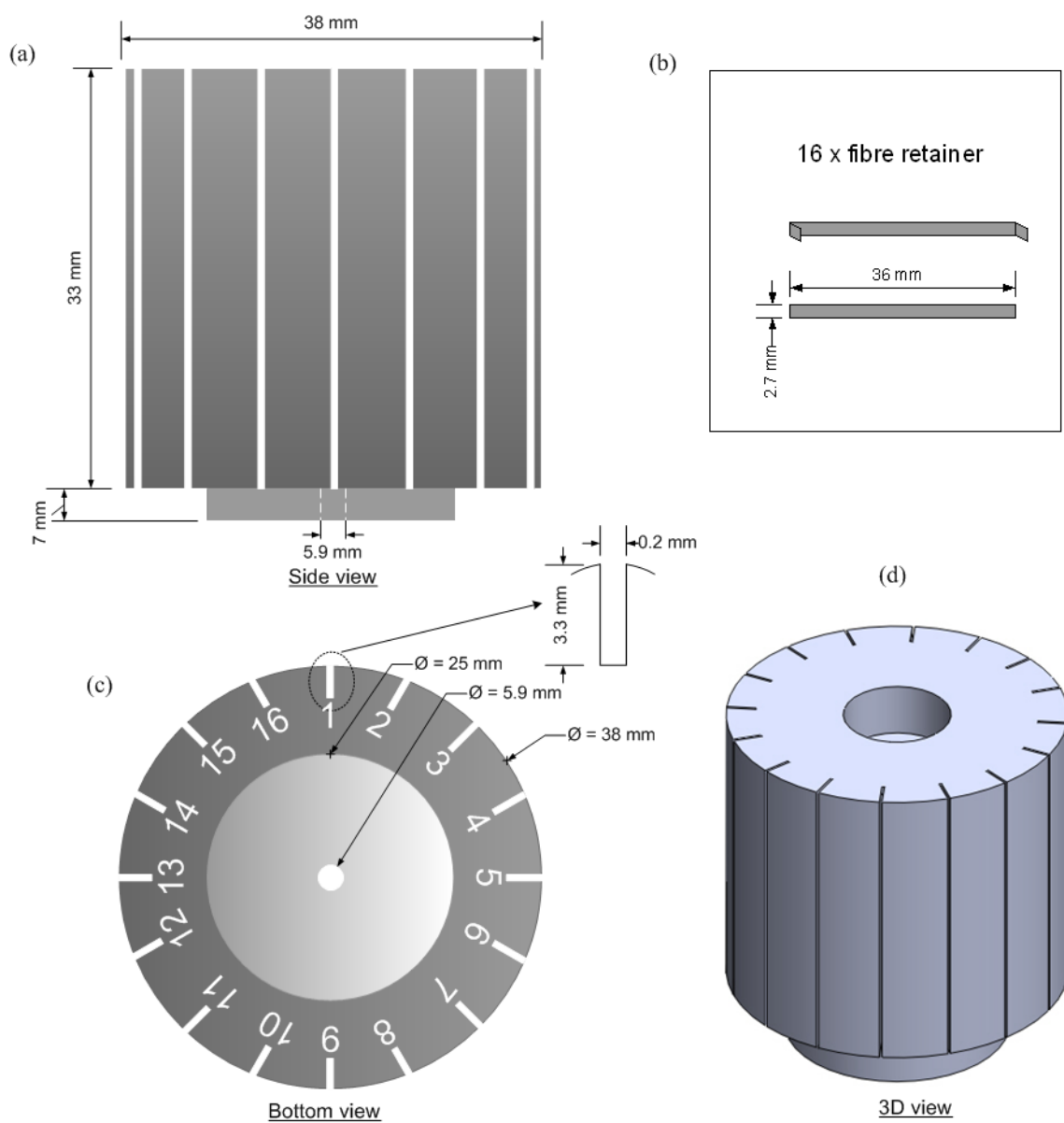


Figure 6.9: Schematic illustration of a special optical fibre holder with (a), (c), (d) are the side, bottom, 3D views and (b) dimension of a fibre retainer.

Step 3. Gold depositing

After the insertion of the optical fibres into the fibre holder, a gold layer was deposited on the fibre end-faces by using a Thermionics VE-180 e-beam/thermal vacuum evaporator (Figure 6.10(a)). During the evaporation process as shown in Figure 6.10(b), the optical fibre end-faces (substrate) faced the metal source, where the plume of evaporated gold particles (evaporant) radiating from the crucible to ensure that the fibre side walls and the fibre end-faces were completely covered with a 140 nm thick gold layer. Gold was chosen as the metal since it is highly conductive and resistant to oxidation. The sample mount was rotated to improve uniformity and the thickness of the gold was monitored by a quartz crystal detector. The deposition rate was kept constant at $\sim 0.2 \text{ nm s}^{-1}$ at a chamber pressure of $\sim 3 \times 10^{-6}$ torr.

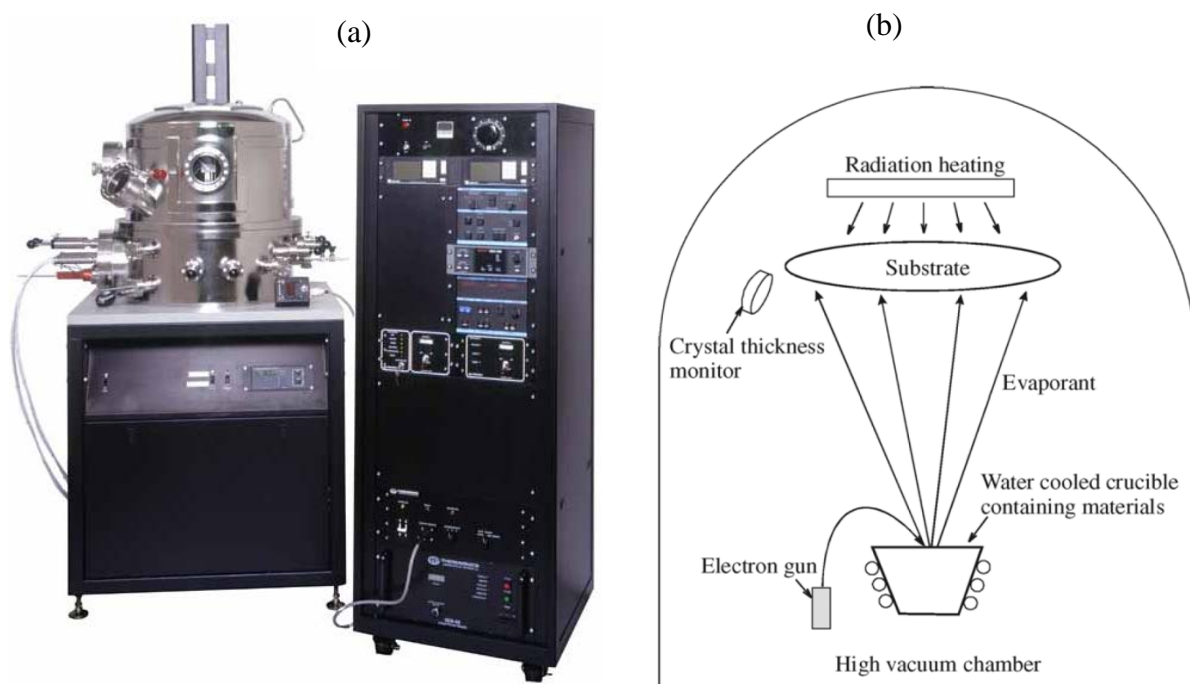


Figure 6.10: (a) A Thermionics VE-180 e-beam/thermal vacuum evaporator [206], and (b) Schematic diagram of an evaporation process.

Step 4. Designing of sub-wavelength apertures

Before carrying out FIB milling, the nanostructure designs were laid out in QCad version 2.1 (RibbonSoftTM). Within the FIB milling software, the structure layout is imported as a 24 bits bitmap pattern. The imported pattern can be rescaled to any desired dimensions. When

drawing a bitmap it is recommended to use black for non-milling points and white for the milling points. Figure 6.11 shows a Qcad layout of a cross-shaped nanostructure array.

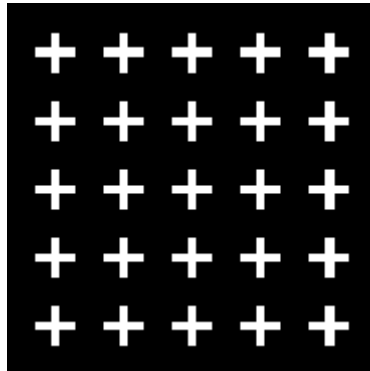


Figure 6.11: A Qcad graphic software layout design - The black and white colour scheme of a 5×5 cross-shaped array structure. The layout is scaled to the desired dimensions within the FIB milling software.

Step 5. FIB milling

The nanofabrication of sub-wavelength apertures on the fibre end-face was performed using a FEI Nova Dualbeam™ FIB and SEM system (Figure 6.12).



Figure 6.12: xT FEI Nova Dualbeam FIB and SEM system [207].

The FIB/SEM system is a combination of a high resolution 30 keV field emission SEM electron column (with beam spot sizes ranging from 2 to 10 nm) and a 30 keV Ga+ FIB

column (with a minimum beam spot size of 7 nm) integrated into one (Figure 6.13). The FIB column is tilted by 52° from the electron beam column. Both beams can be aligned to hit the same spot by 'eucentric height' (the height adjustment of the specimen) adjustment of the sample stage. In this study, the FIB with settings of 30 keV Ga^+ ions, 30 pA current were used to pattern the nanostructure array.

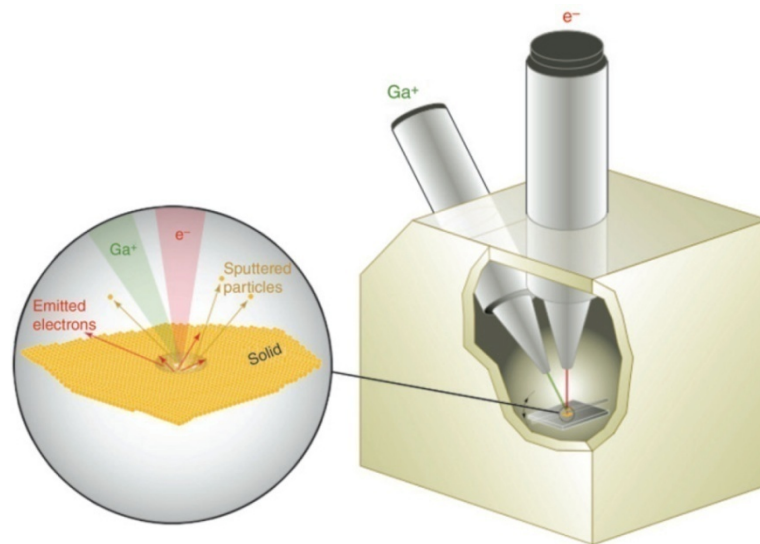


Figure 6.13: Schematic illustration of a dual-beam FIB-SEM instrument. Expanded view shows the electron and ion beam sample interaction [208]

It is important to note that FIB milling in nonconductive materials (optical fibres) normally imposes an extra degree of complexity, i.e. not all the fibre side walls are coated with gold and this can cause random deflection of the ion beam. The acceleration of positive ions into the sample induces the emission of backscattered and sputtered ions as well as secondary electrons with varying rates. These electrons only partially compensate the net injection of positive Ga^+ ions, this leads to charge building up on the surface if the fibre side walls have not been grounded correctly. Such a problem is often overcome by coating a 200-300 nm layer of carbon [209] or using a double sided carbon tape on the fibre side walls and the grounded sample holder. Therefore, this carbon layer minimizes sample charging, increases beam stability and improves image quality. Figure 6.14 shows the actual fibre holder which was mounted into the FIB sample mounting stage. Figure 6.15 depicts a summary of the fabrication process.

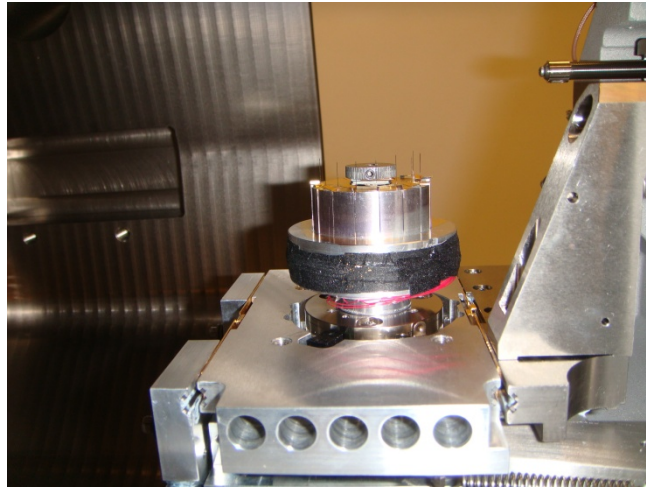


Figure 6.14: A special fibre holder mounted to a FIB vacuum chamber where a double sided tape (black band) is being used.

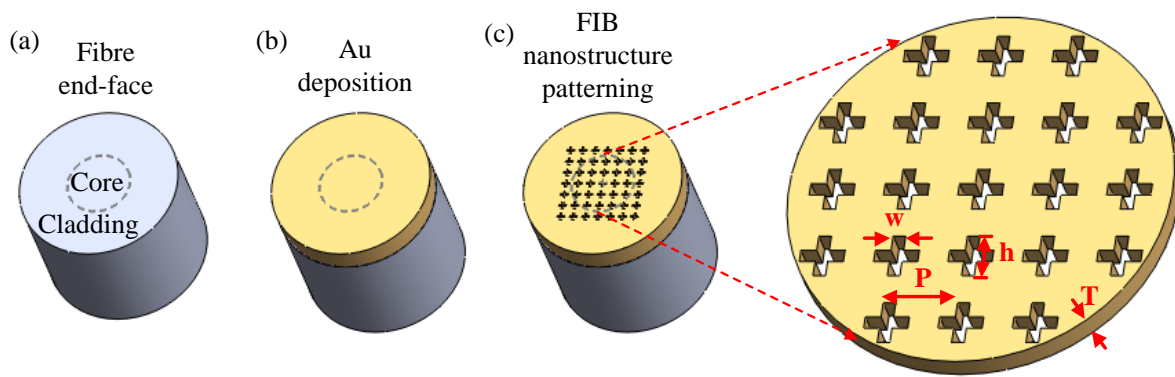


Figure 6.15: A fabrication process of a cross-shaped apertures array on the end-face of a single mode fibre.

An SEM image of a single mode fibre having an array of cross-shaped apertures milled in a 140 nm thick gold on its end-face is presented in Figure 6.16. The parameters of the cross-shaped were: length (h) = 300 nm, width (w) = 20 nm, and periodicity (P) = 400 nm.

As shown in Figure 6.16 (c). The milled crosses were a good match with the simulation in terms of the ratio of the parameter dimensions. Variances in the parameters were of the order of 2 nm and this would not be expected to cause a significant discrepancy between the experimental data and the simulation. However the broadening of the peak is not inconsistent with such a variation.

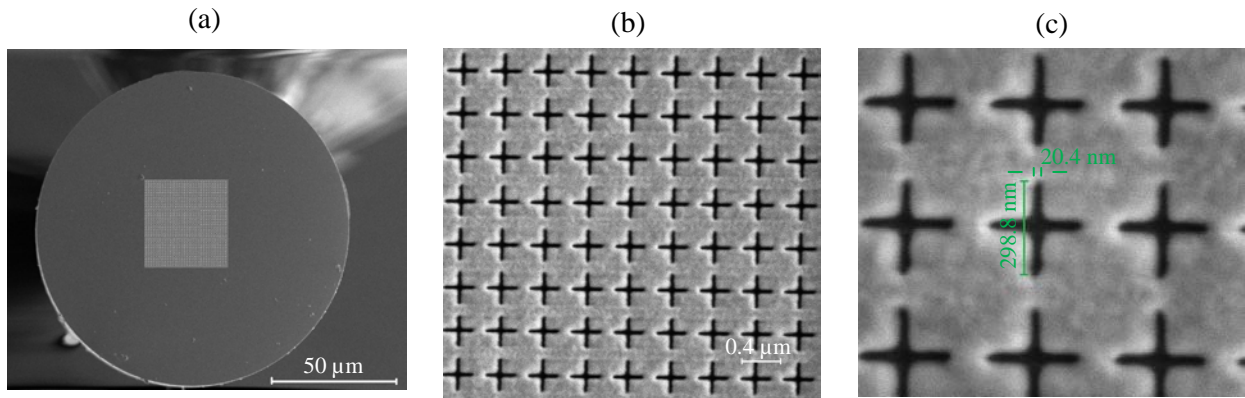


Figure 6.16: (a) an SEM image of a 30×30 array of cross-apertures milled on the gold-coated end-face of the fibre; (b) a zoom-in image of the array; (c) actual fabrication dimensions of the cross-shaped apertures.

6.3.3. Experimental and simulation results comparison

As can be seen from Tables 7.1 and 7.2, a better fit can be achieved when the periodicity (P) of the array changed. Hence, the cross-shaped nanostructure array performed best with the following parameters: $T = 140$ nm, $P = 400$ nm, $w = 20$ nm, and $h = 300$ nm.

The experiments were carried out using the reflection-based configuration as described in Section 6.3. The overlaid experimental and simulated reflection spectra as function of wavelength for a 30×30 array of cross-apertures milled on the gold-coated end-face of the fibre, with $h = 300$ nm, $w = 20$ nm, and $P = 400$ nm are shown in Figures 6.17 to 6.20 for different liquid refractive indices.

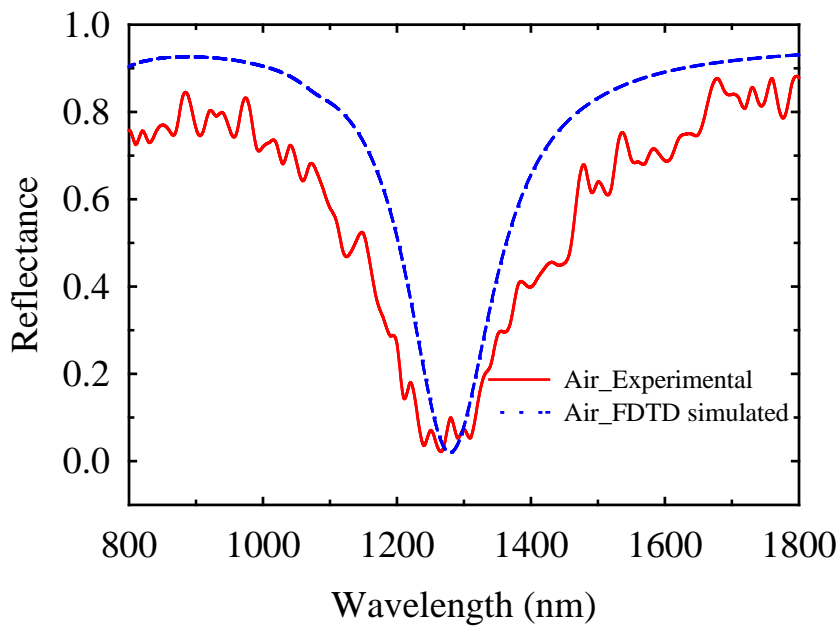


Figure 6.17: FDTD simulated (---) and experimental (—) reflection spectra of the OFS when the medium surrounding the fibre end-face was air. The cross-shaped array parameters were: $h = 300$ nm, $w = 20$ nm, $P = 400$, and $T = 140$ nm.

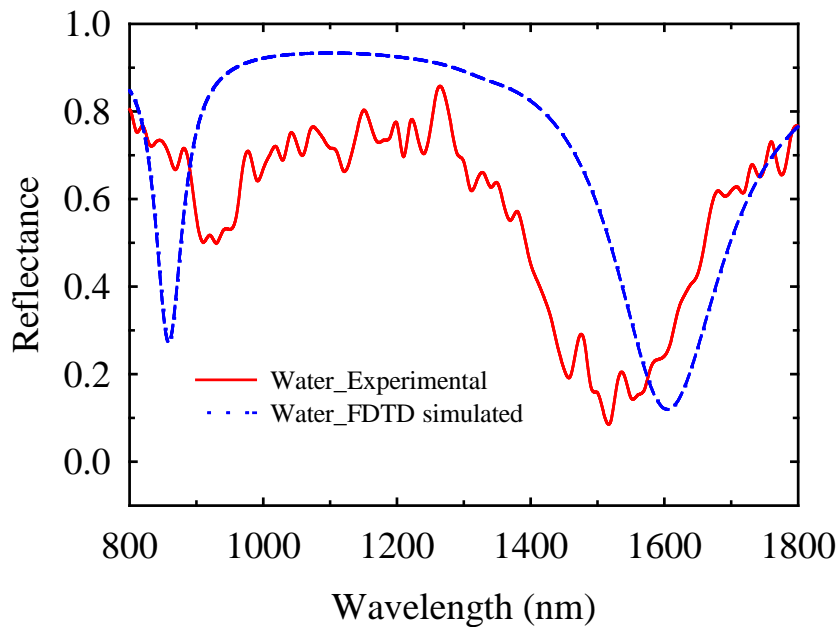


Figure 6.18: FDTD simulated (---) and experimental (—) reflection spectra of the OFS when the fibre end-face was immersed into water. The cross-shaped array parameters were: $h = 300$ nm, $w = 20$ nm, $P = 400$, and $T = 140$ nm.

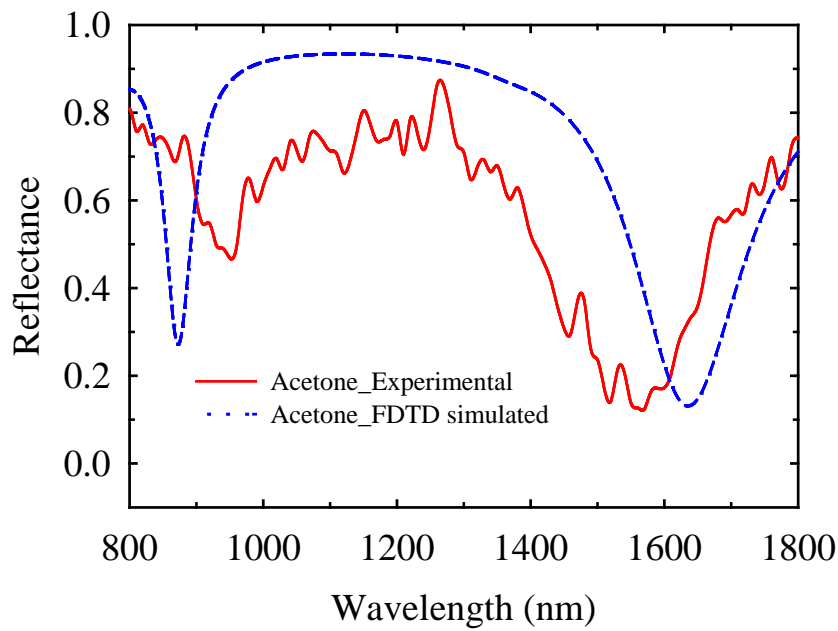


Figure 6.19: FDTD simulated (---) and experimental (—) reflection spectra of the OFS when the fibre end-face was immersed into acetone. The cross-shaped array parameters were: $h = 300$ nm, $w = 20$ nm, $P = 400$, and $T = 140$ nm.

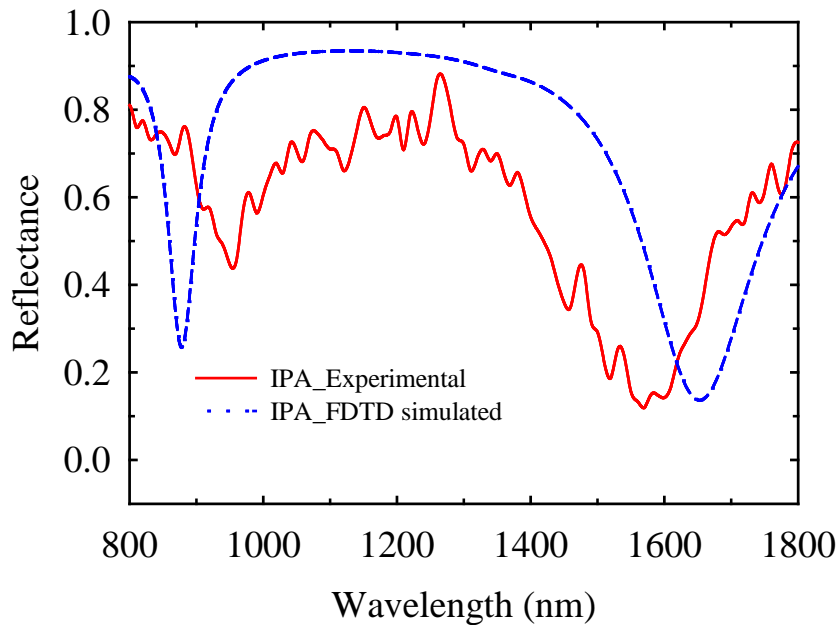


Figure 6.20: FDTD simulated (---) and experimental (—) reflection spectra of the OFS when the fibre end-face was immersed into isopropyl-alcohol (IPA). The cross-shaped array parameters were: $h = 300$ nm, $w = 20$ nm, $P = 400$, and $T = 140$ nm.

It can be seen from Figure 6.17, for a 30×30 cross-shaped with length (h) = 300 nm, width (w) = 20 nm, periodicity (P) = 400 nm and gold film thickness = 140 nm, a dip in reflection wavelength was measured at ~ 1270 nm, while the FDTD simulated model predicted ~ 1275.86 nm. There is a small spectral difference between the simulated and experimental results. This could possibly be due to small imperfections in the fabricated device.

When the medium surrounding the single mode fibre end-face was changed from air to water, acetone and IPA, spectral variations were observed as shown in Figures 6.17 to 6.20. The spectral difference associated with the reflection dips between the simulated and experimental results are widen, as listed in Table 6.1. To repeat this experiment, one would need to have the same testing environment as stated in section 6.3. The reproducibility of the results can be effected due to fabrication variability and wetting ability. Therefore some minor spectral changes in the reflectance are expected.

Refractive index	Reflection dip Measured (nm)	Reflection dip FDTD simulated (nm)	Difference in reflection dip (nm)
Air = 1.00	~ 1270	~ 1275.86	~ 5.86
Water = 1.33	~ 1520	~ 1608.70	~ 88.70
Acetone = 1.36	~ 1570	~ 1632.35	~ 62.35
IPA = 1.38	~ 1575	~ 1656.72	~ 81.72

Table 6.1: The difference in reflection spectra when the medium surrounding the single mode fibre end-face was changed from air to water, acetone and IPA.

From Table 6.1, it can be seen that there are large spectral differences between the measured and simulated results especially when the medium surrounding the fibre end-face was changed to water, ethanol and IPA. These discrepancies may be due to imperfections in the fabrication process. It has been shown that several kinds of fabricating artefacts, such as aperture length and width variation may significantly alter the reflection spectra [210]. Overall, there is an agreement between theoretical simulations and experimental reflection curves. As expected, the reflection spectrum does shift to a longer wavelength as the RI of the liquid increases. The dip around 900 nm corresponds to the first Fabry-Perot resonance.

The minimum dip wavelength of the measured reflectance for each liquid was plotted against the RI, as shown in Figures 6.21. A linear straight line could be fitted to the measured points. A linear fit between the shift of minimum in the reflection spectrum and the change of RI of

the medium surrounding the optical fibre end-face was obtained, with a sensitivity of approximately 1210.2 nm/RIU.

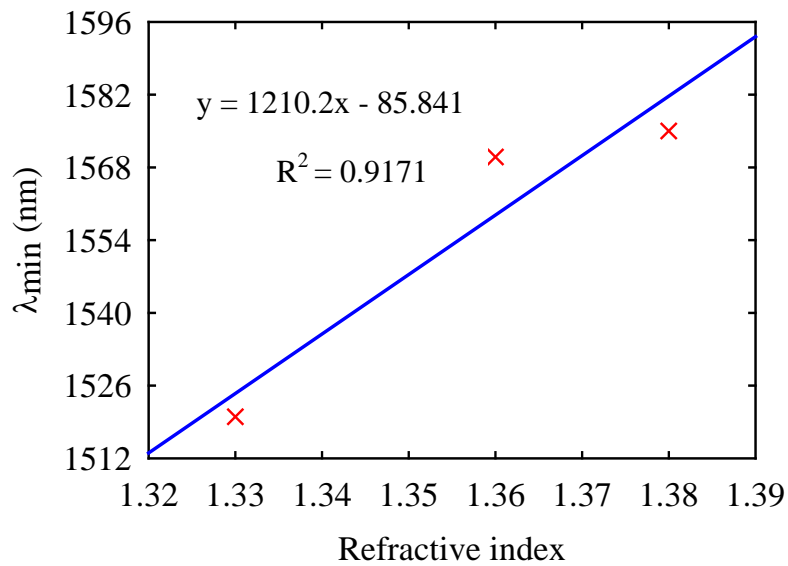


Figure 6.21: A plot of the measured SPR dip wavelengths versus the index of refraction of various liquids. The results of a linear fit are shown.

Similarly, for the FDTD simulated data, the sensor shows a sensitivity of approximately 985.22 nm/RIU, as shown in Figure 6.22.

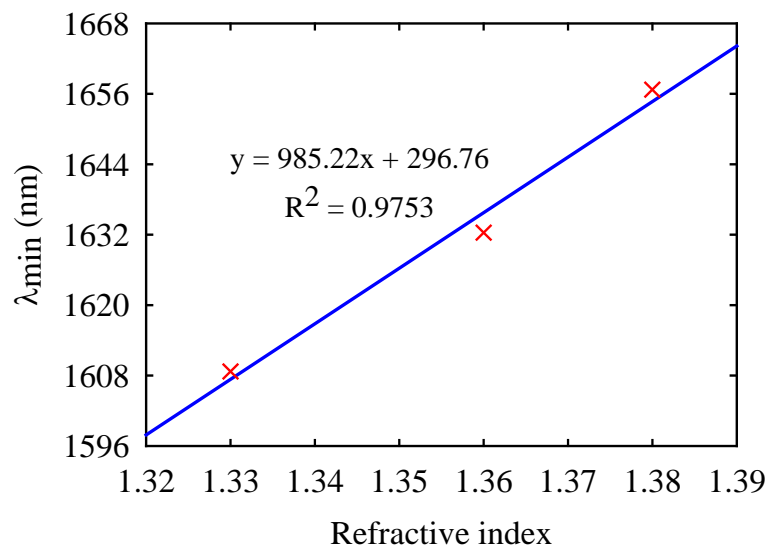


Figure 6.22: A plot of the FDTD simulated SPR dip wavelengths versus the index of refraction of various liquids. A Linear relationship between the minimum reflected wavelengths and the refractive indices is obtained with the indicated parameters.

6.3.4. Surface tension between liquids and sub-wavelength apertures

For the samples prepared in this thesis an ultrasonic bath was used to clean the sample in order to minimize wetting issues.

There is evidence that under certain conditions the liquid interacting with an array of sub-wavelength apertures cannot penetrate into the array due to the surface tension between the liquid and the metal [211-214]. Hence the sub-wavelength apertures are not totally immersed in the solutions. A body of research has been conducted to discover ways to control the surface wettability and liquid spreading on patterned surfaces for a broad range of applications, including DNA microarrays, inkjet printing and thin film lubrication. For an in depth discussion on the subject readers are referred to reference [212].

The aim here is to determine if this might explain the results discussed in the previous section, that is the large discrepancy between the measured and simulated reflection spectra of the array of cross-shaped apertures with parameters: length (h) = 300 nm, width (w) = 20 nm, period (P) = 400 nm and gold thickness (T) = 140 nm embedded on the end-face of an optical fibre. By considering the case where the liquids cannot penetrate into the apertures, a new set of FDTD simulation results have been generated as depicted in Figures 6.23 - 6.25 for the reflection-based OFS.

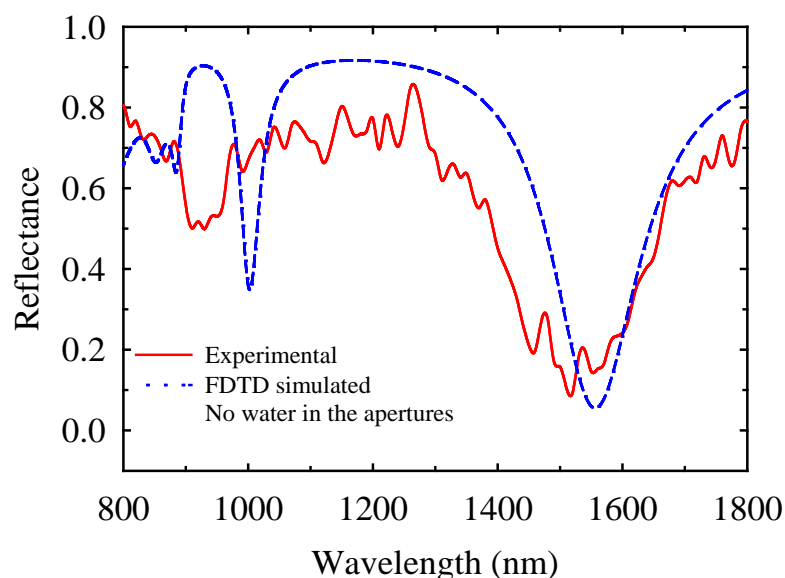


Figure 6.23: FDTD simulated (---) and experimental (—) reflection spectra of the SPR OFS by assuming that the water was not inside the apertures. The cross-shaped array parameters were: $h = 300$ nm, $w = 20$ nm, $P = 400$, and $T = 140$ nm.

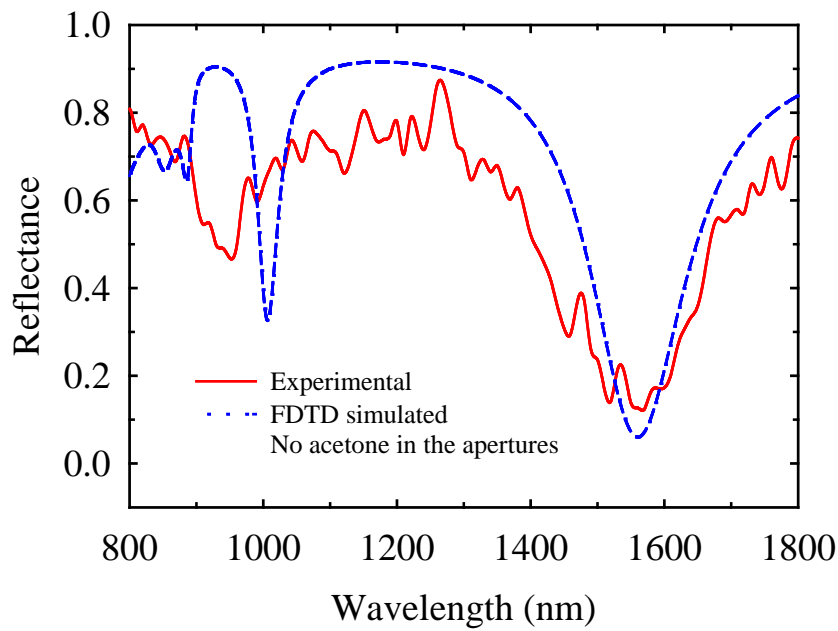


Figure 6.24: FDTD simulated (---) and experimental (—) reflection spectra of the SPR OFS by assuming that the acetone was not inside the apertures. The cross-shaped array parameters were: $h = 300$ nm, $w = 20$ nm, $P = 400$, and $T = 140$ nm.

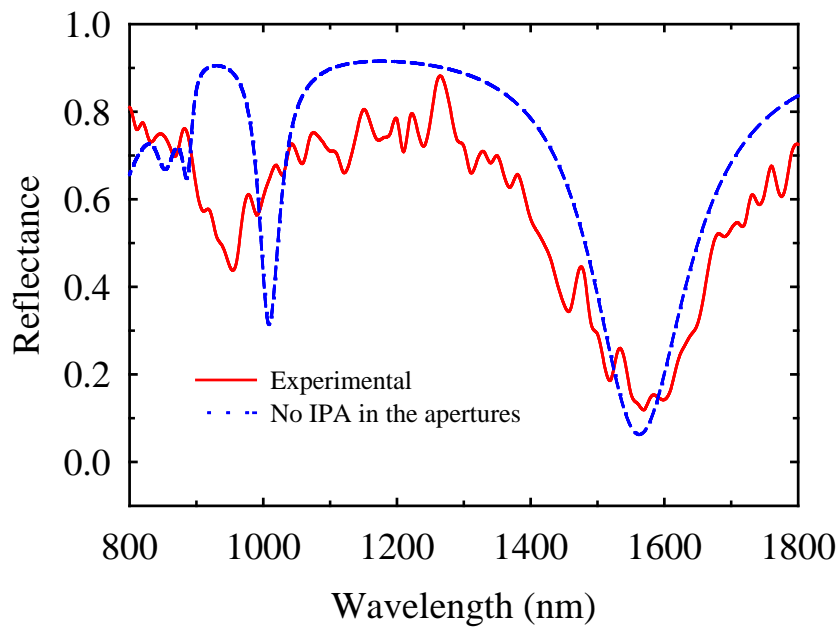


Figure 6.25: FDTD simulated (---) and experimental (—) reflection spectra of the SPR OFS by assuming that the isopropyl-alcohol (IPA) was not inside the apertures. The cross-shaped array parameters were: $h = 300$ nm, $w = 20$ nm, $P = 400$, and $T = 140$ nm.

Figure 6.26 depicts a plot of minimum dip wavelengths versus refractive indices of the FDTD simulated from Figures 6.23 to 6.25. A linear relationship can be seen here with a sensor sensitivity of 162.28 nm/RIU. This is much smaller than the previous result of the case when liquids were presented inside the apertures.

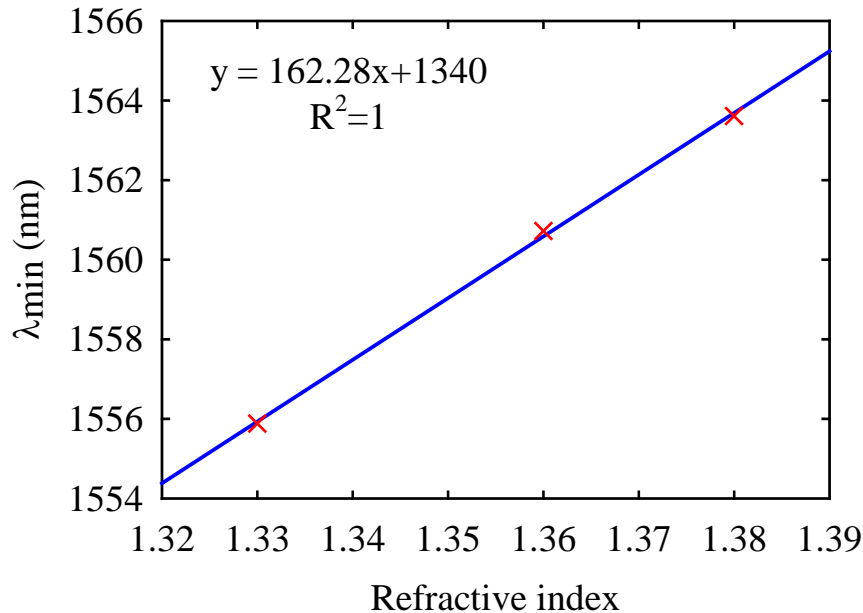


Figure 6.26: A plot of the FDTD simulated SPR dip wavelengths versus the index of refraction of various liquids which were not presented inside the apertures. A linear relationship between the minimum reflected wavelengths and the refractive indices is obtained with the indicated parameters.

Clearly, there is a discrepancy between the simulation and experiment results. By assuming that the liquid does not enter the array, the dip in the reflectance spectrum generated by the simulation matches more closely the experimental data however the sensitivity predicted by the simulation is greatly reduced. It is therefore possible to speculate that the real situation may be quite complex interplay between the metallic surface, trapped pockets of air and the liquid. This does not auger well for the development of a robust OFS based on sub-wavelength arrays.

Due to high fabrication cost of these sensors, it is not feasible to explore the sensor sensitivity experimentally for the multitude nanostructures and configurations. In the next chapter, this thesis focuses on FDTD modeling and simulations as they have proven to be reliable for both transmission- and reflection-based configurations.

Chapter 7. Simulations, Comparison and Discussion

7.1. Introduction

In previous chapters the reliability of using the FDTD method to predict the behaviour of an OFS based on an array of metallic sub-wavelength apertures has been established through comparison with published and current experimental data.

There are many types of sub-wavelength apertures that have been studied for the enhanced optical transmission (EOT), which can be classified by some of the most common aperture shapes, for examples, circular [175,215], rectangular [158,159], annular [161-163], and some unconventional aperture shapes, such as C [164], bowtie [165], I [166], and cross [167-169]. Four types of sub-wavelength apertures have selected for intensive simulation: the circular, cross, annular and rectangular apertures.

This chapter compares sensor sensitivities from all four sub-wavelength apertures, so as to establish the validity of building such sensors by comparison of the determined sensitivity with currently used technologies. All experimental (from Chapter 6) and FDTD results were obtained by using the linear polarized incident light source. If un-polarized light is considered, as is the case in many experiments, the affect would be to reduce the sensitivity of the sensor.

7.2. Reflection spectra from an array of circular apertures (nanoholes)

The simulation of reflection properties of an array of circular apertures embedded on the end-face of an optical fibre has been described in Section 6.3.1 of this thesis. In a similar manner, for a single mode fibre having a core diameter of $8\ \mu\text{m}$ ($\sim 50.2\ \mu\text{m}^2$ area), an array of 15×15 nanoholes with the following parameters: $P = 500\ \text{nm}$, $D = 300\ \text{nm}$, which is equated to $\sim 56.2\ \mu\text{m}^2$ in area, should sufficiently cover the entire fibre core, as shown in Figure 7.1. A simulation setup for a unit nanohole structure is shown in Figure 7.2(a), while the electric field intensity ($|E|^2 = |E_{\text{total}}|^2 / |E_{\text{incident}}|^2$) in the vicinity of the nanohole is shown in Figure 7.2 (b), where $|E_{\text{total}}|^2$ and $|E_{\text{incident}}|^2$ denote the electric field intensity of the total field and the incident field, respectively. Initially the sample around the fibre end-face was assumed to be air, $n = 1$.

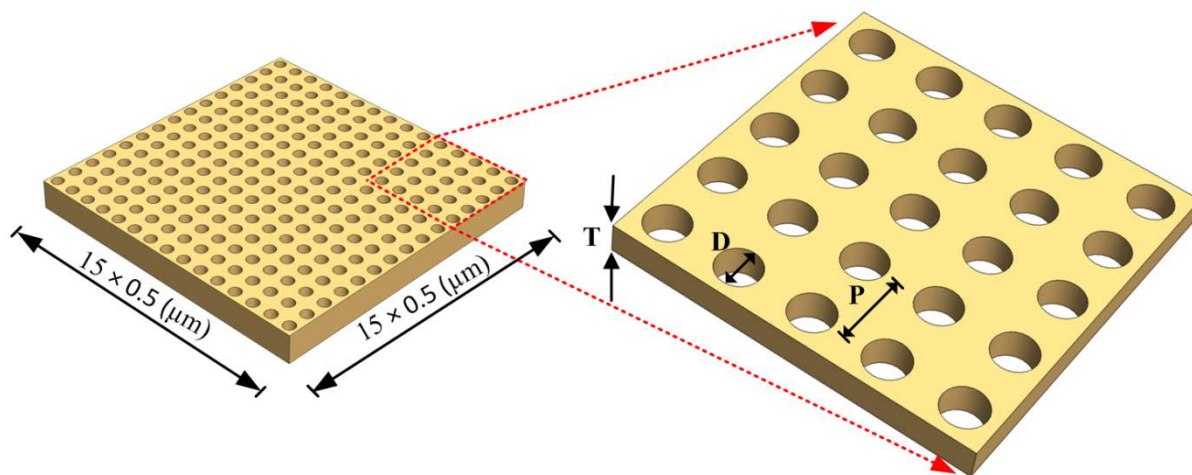


Figure 7.1: A 15×15 gold array of sub-wavelength circular apertures.

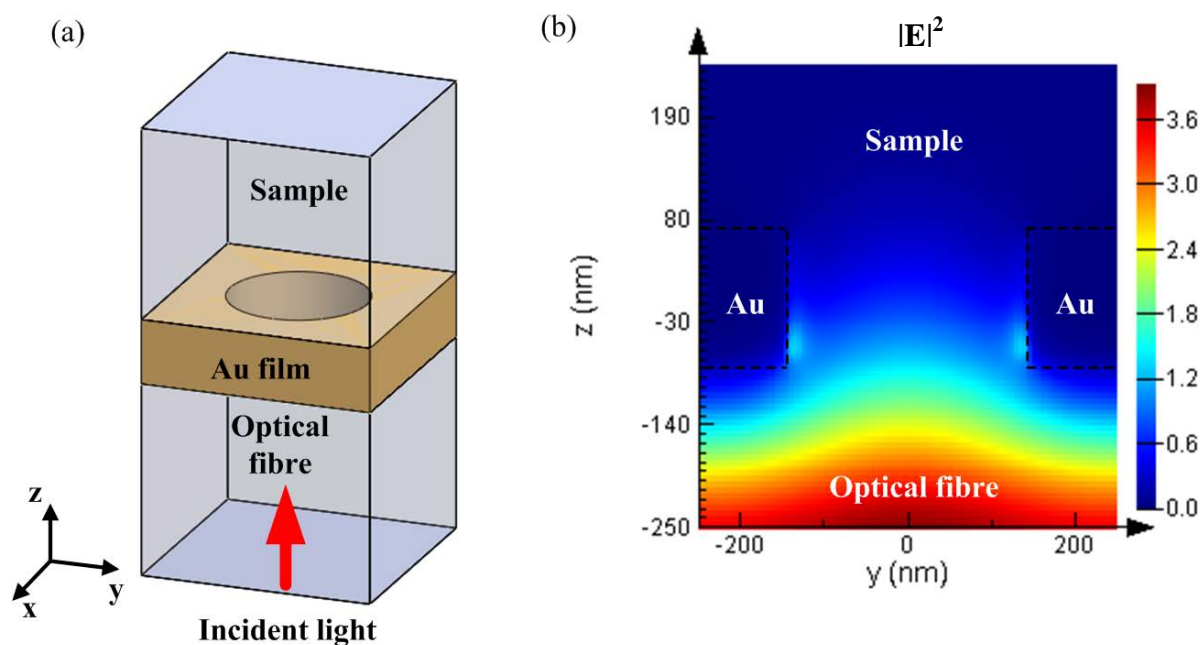


Figure 7.2: (a) A unit cell of the fibre end-face sensor simulated in FDTD; (b) The intensity of the electric field ($|E|^2$) around the nanohole: the nanohole is centered at the origin and the film boundaries are outlined in dashed lines.

Initially, the refractive indices for the regions of optical fibre and sample were taken as 1.5 and 1 (air). Subsequently, the RI of the sample was varied corresponding to a set of liquids or solutions. This enabled the sensitivity of the proposed OFS to be explored.

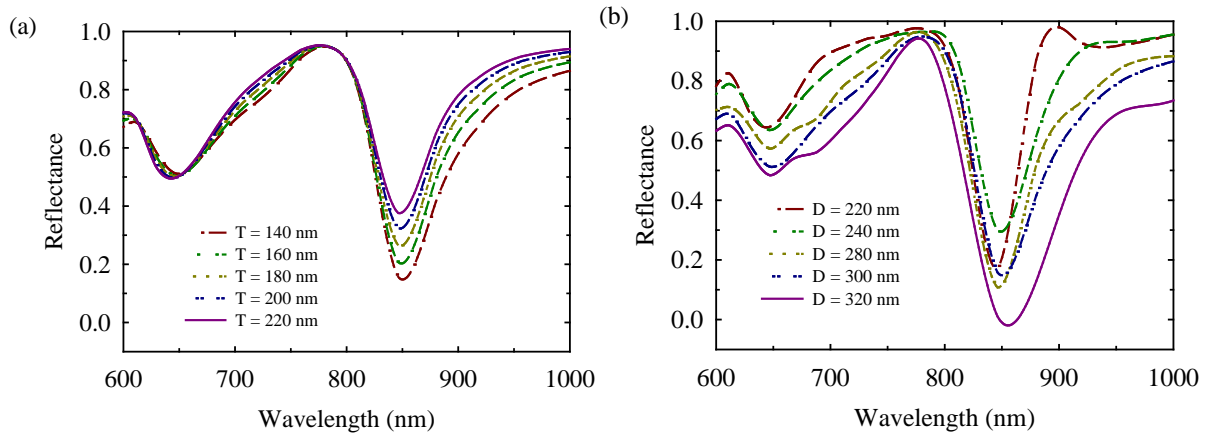


Figure 7.3: FDTD calculations of the reflectance intensity through a circular nanohole array with (a) the gold film thickness, T , varying from 140 to 220 nm while P and D remained at 500 and 300 nm, respectively; (b) the nanohole diameter, D , varying from 220 to 320 nm while P and T remained at 500 and 140 nm, respectively.

Figure 7.3(a) shows the reflection as a function of wavelength for circular nanoholes of a fixed periodicity of 500 nm and a diameter of 300 nm. It can be seen that increasing the thickness of the metal film leads to a narrower resonant dip and a near-uniform increase in the reflection intensity at longer wavelengths.

Figure 7.3(b) shows the reflection as a function of wavelength for nanoholes of a fixed thickness of 140 nm and a periodicity of 500 nm. It indicates that increasing the diameter of the nanoholes from 220 to 320 nm leads to a wider resonant dip and a non-uniform decrease in the reflection intensity at longer wavelengths.

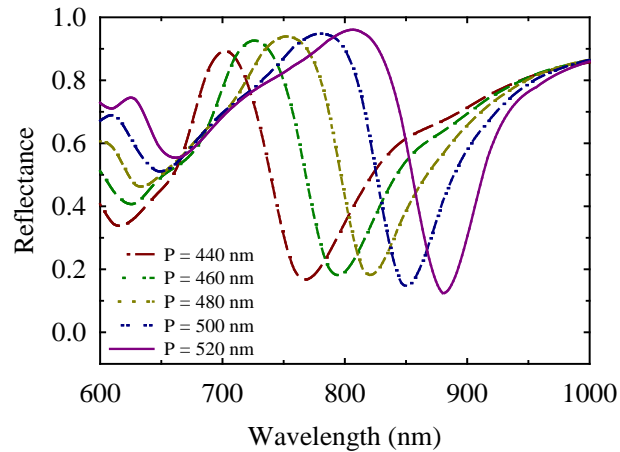


Figure 7.4: FDTD calculations of the reflectance intensity through a circular nanohole array with the periodicity, P , varying from 440 to 520 nm while D and T remained at 300 and 140 nm, respectively.

Figure 7.4 shows that by increasing the periodicity of the nanoholes from 440 to 520 nm, a red-shift in the resonant dip wavelength is observable from around 760 to 880 nm.

These findings suggest that a potential sensing device can be established, in which case a standard 2×1 single mode fibre coupler can be employed. The configuration is similar to that shown in Figure 6.6 of this thesis. The resonance spectra of the circular arrays were simulated as the index of the material interacting with the sensing area of the fibre end-face was varied from 1.33 to 1.47. As shown in Figure 7.5, the simulated resonances underwent a red-shift as the index surrounding them was increased.

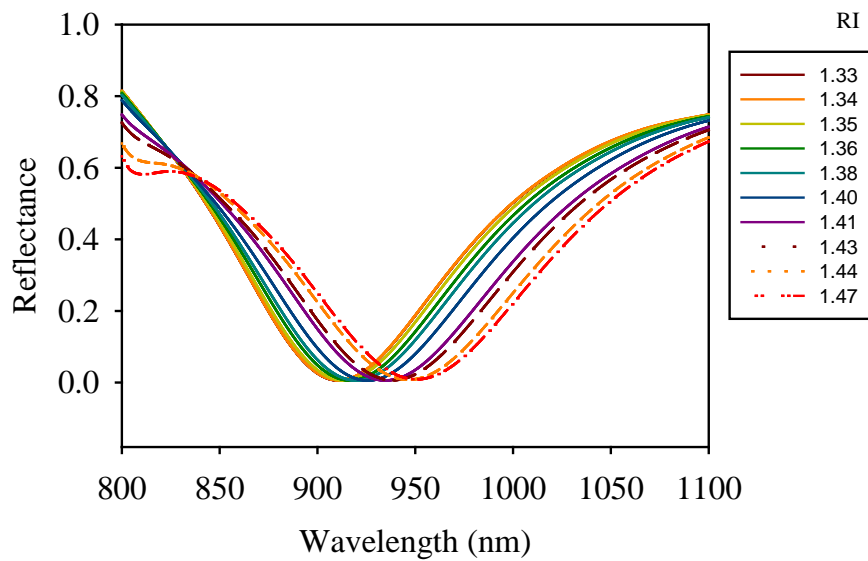


Figure 7.5: FDTD calculations of the reflected power spectra for the fibre sensor (circular apertures) in various liquids with the gold film thickness $T = 140$ nm, periodicity $P = 500$ nm and hole diameter $D = 300$ nm.

When the minimum dip wavelength for each liquid was plotted against the RI, as shown in Figure 7.6, a straight line could be fitted to the calculation points. This linear relationship between the shift of minimum in the reflection spectrum λ_{\min} and the assuming change of RI (from 1.33 to 1.47) of the surrounding medium would be obtained, with a sensitivity of approximately 373 ± 16 nm/RIU.

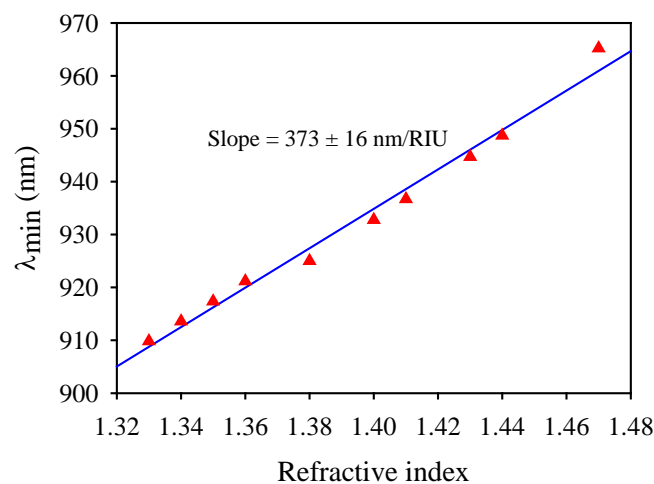


Figure 7.6: Dependence of SPR dip wavelength on the index of refraction of various liquids, showing the linear fit. The circular parameters: $T = 140$ nm, $P = 500$ nm and $D = 300$ nm

7.3. Reflection spectra from an array of cross-shaped apertures

In a similar manner to the above, various reflection spectra from a cross-shaped array with different sizes, thicknesses and periodicities were calculated. A representation of a 15×15 cross-shaped array is shown in Figure 7.7. A unit cross-shaped aperture for simulation purposes is shown in Figure 7.8. Once again, the initial sample surrounding the fibre end-face was air.

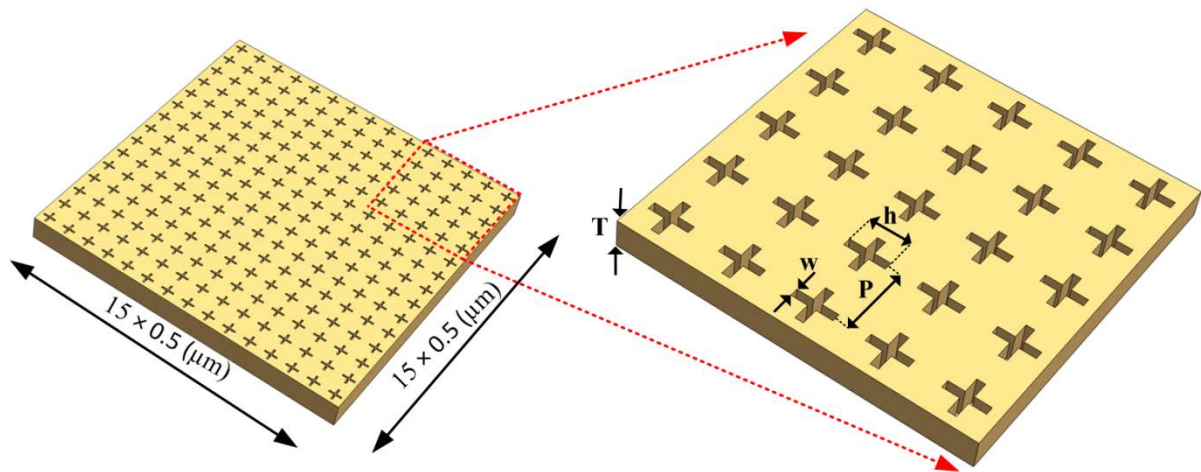


Figure 7.7: An illustration of a 15×15 cross-shaped array with a zoom-in 5×5 array.

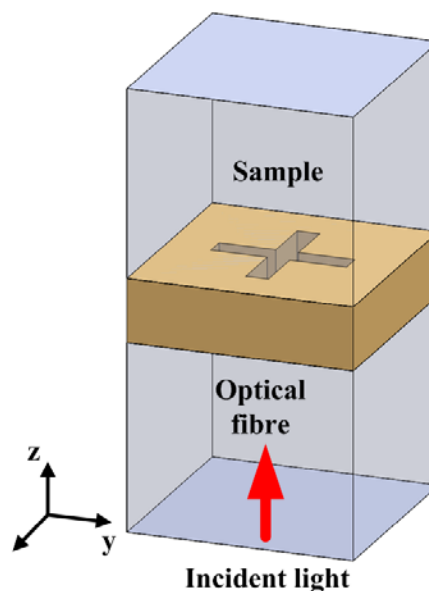


Figure 7.8: A unit cell representation for cross-shaped apertures for simulation purposes.

The simulation of reflection properties of an array of cross-shaped apertures embedded on the end-face of an optical fibre has been described in Section 6.3.1 of this thesis. Figure 7.9(a)

shows the reflection as a function of wavelength for a cross-shaped array of a fixed periodicity of 500 nm, a width of 20 nm and a thickness of 140 nm. It can be seen that increasing the arm length of the cross-shaped array leads to a stronger resonant dip and a red-shift in the resonant wavelength.

On the other hand, Figure 7.9(b) shows the reflectance as a function of wavelength for a cross-shaped array of a fixed thickness of 140 nm, an arm length of 300 nm and a periodicity of 500 nm. It clearly indicates that as the width of the cross decreases, leads to a weaken of the resonant dip coupled with a strong red-shift in the resonant wavelength.

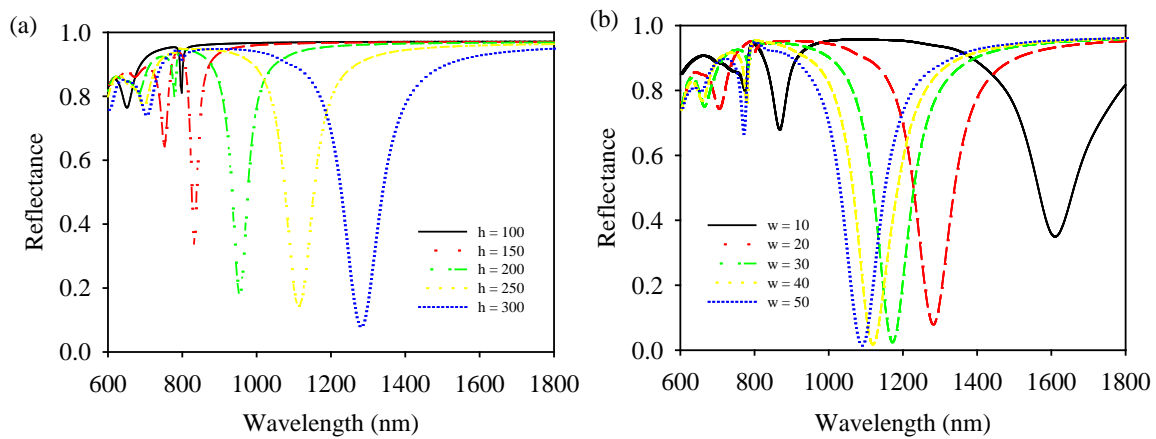


Figure 7.9: FDTD calculations of the reflectance intensity through a cross-shaped array with (a) the length, h varying from 100 to 300 nm while w , T and P were kept constant at 20, 140 and 500 nm, respectively; (b) the width, w varying from 10 to 50 nm while h , T and P were kept constant at 300, 140 and 500 nm, respectively.

The simulation considered the case with a normal incident plane wave. Polarization of the wave when the electric field vector points perpendicular to vertical axis of the cross-shaped array is designated as transverse electric (TE), while the designated transverse magnetic (TM) refers to the case when the electric field vector is parallel to the vertical axis of the array, as shown in Figure 7.10.

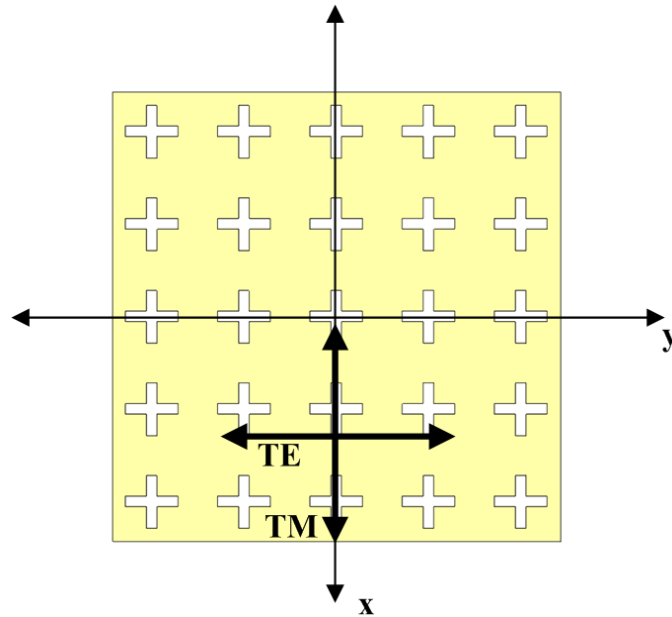


Figure 7.10: Geometry of a 5 by 5 array of cross-shaped apertures used in analysis of the reflection profiles. The analysis considers a normally incident plane wave with either TE or TM polarization.

Figures 7.11 and 7.12 show the electric field intensity distribution for TE and TM polarizations in the vicinity of the cross aperture with the following parameters: $T = 140 \text{ nm}$, $P = 500 \text{ nm}$, $h = 300 \text{ nm}$ and $w = 10 \text{ nm}$.

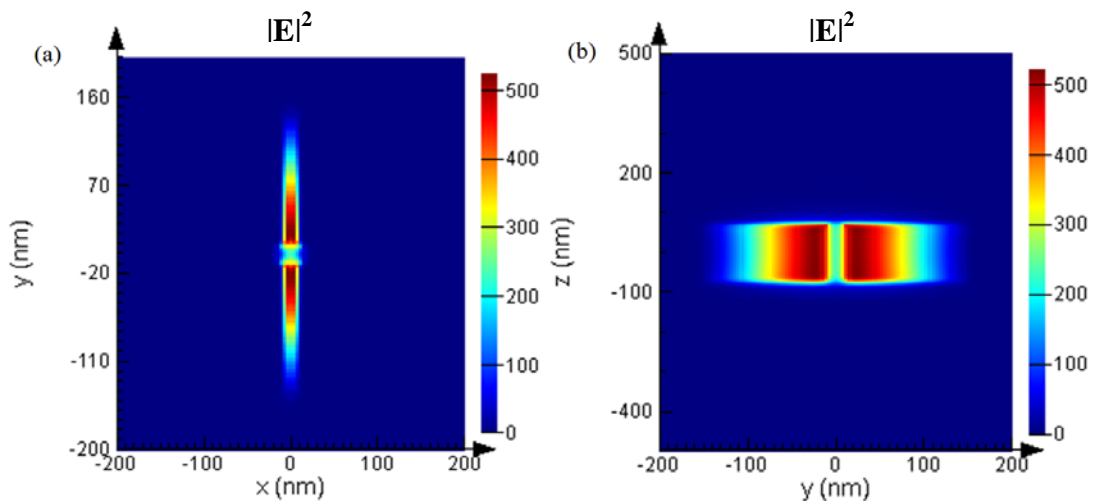


Figure 7.11: TE-polarization - (a) Electric field intensity versus position $[x, y]$, (b) Electric field intensity versus position $[y, z]$.

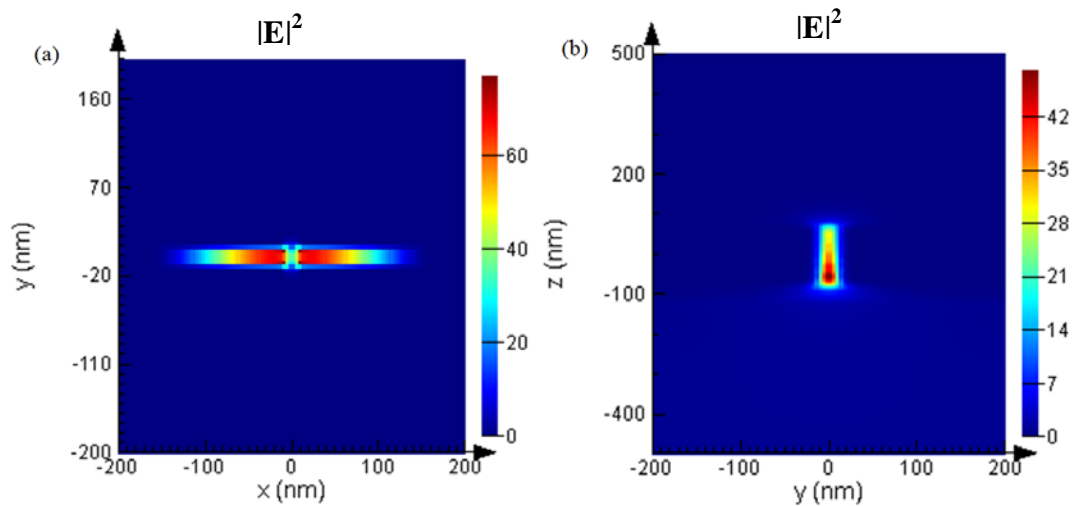


Figure 7.12: TM-polarization - (a) Electric field intensity versus position [x, y], (b) Electric field intensity versus position [y, z].

Figure 7.13(a) shows the reflectance as a function of wavelength for a cross-shaped array of fixed w , h , and P of 20, 300, and 500 nm, respectively as the thickness varied. It can be seen that increasing the thickness of the metal film leads to a narrower resonant dip and a stronger change in the reflection intensity.

Figure 7.13(b) shows the reflectance as a function of wavelength for a cross-shaped array of fixed T , w , and h of 140, 20, and 300, respectively as the periodicity varied. It indicates that increasing the periodicity of the array from 400 to 540 nm leads to a narrower reflection dip and an increase in the reflection intensity.

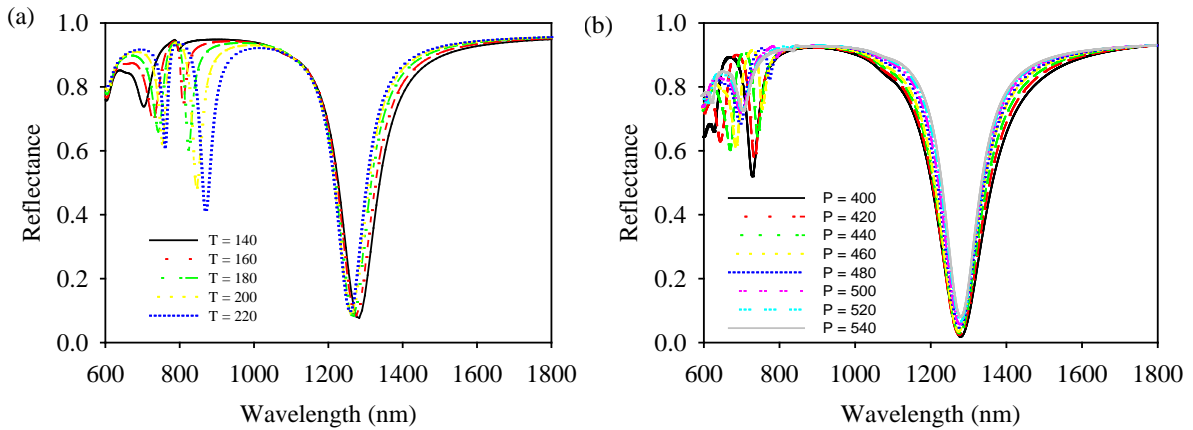


Figure 7.13: FDTD calculations of the reflectance intensity through a cross-shaped array with (a) the thickness, T varying from 140 to 220 nm while w , h and P were kept constant at 20, 300 and 500 nm, respectively; (b) the periodicity, P varying from 400 to 540 nm while w , h , and T were kept constant at 20, 300 and 140 nm, respectively.

Similar to the above, for example a standard 2×1 single mode fibre coupler can be used here as a reflection-based sensor. The resonance spectra of the cross-shaped arrays were simulated as the index of the material interacting with the sensing area of the fibre end-face was varied from 1.33 to 1.47. As shown in Figure 7.14, the simulated resonances underwent a red-shift as the index surrounding them was increased.

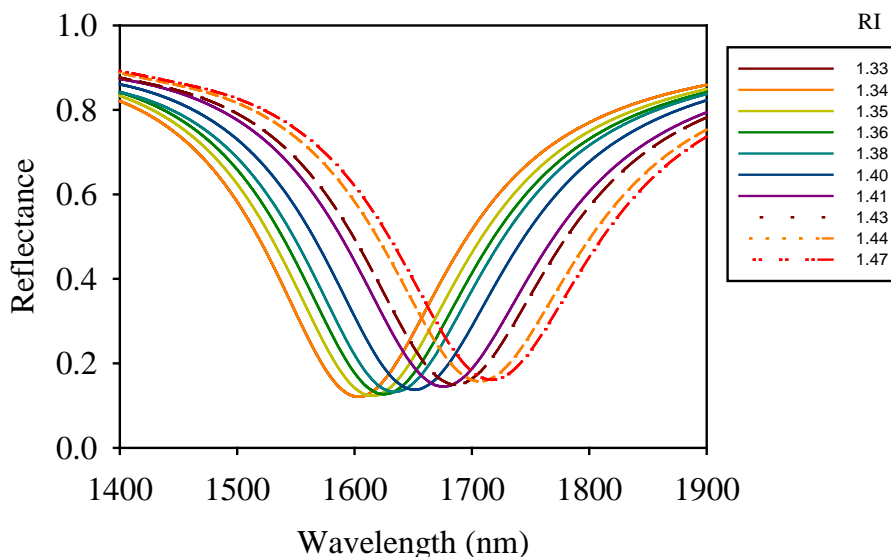


Figure 7.14: FDTD calculations of the reflected power spectra for the fibre sensor in various liquids with the gold film thickness $T = 140$ nm, periodicity $P = 400$ nm, length $h = 300$ nm and width $w = 20$ nm

When the minimum dip wavelength for each liquid was plotted against the RI, as shown in Figure 7.15, a straight line could be fitted to the calculation points. This linear relationship between the shift of minimum in the reflection spectrum λ_{\min} and the assuming change of RI (from 1.33 to 1.47) of the surrounding medium would be obtained, with a sensitivity of approximately 1019 ± 30 nm/RIU.

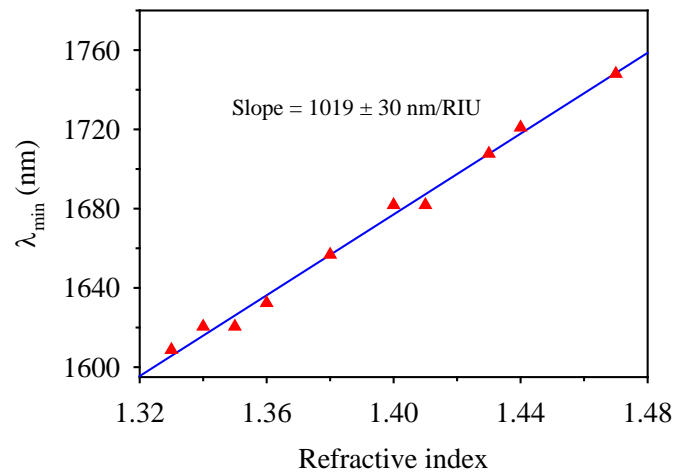


Figure 7.15: Dependence of SPR dip wavelength on the index of refraction of various liquids, showing the linear fit. The cross-shaped parameters: $T = 140$ nm, $P = 400$ nm, $h = 300$ nm and $w = 20$ nm.

Comparison of Figures 7.6 and 7.15 yield two differences in the sensor sensitivities between the optical fibre sensors with circular apertures and those with cross-shaped apertures. For an array of circular apertures, the sensitivity $\sim 373 \pm 16$ nm/RIU whilst it was $\sim 1019 \pm 30$ nm/RIU for an array of cross-shaped apertures. The second difference concerns the dip wavelength range of the resonance when the sensors were to dip into liquids ranging from 1.33 - 1.47. For the circular apertures the wavelength range was $\sim 910 - 965$ nm while the wavelength range for the cross-shaped apertures was $\sim 1609 - 1748$ nm.

Understanding the effects of the fabricated sensor shape and size artefacts on sensor performance is crucial in sensor design. However, it is very time consuming and difficult to perform such investigations experimentally. This thesis adopts the FDTD method discussed above to perform investigations of minor changes in the apertures, e.g., the unavoidable rounded corners of cross-shaped apertures due to the fabrication process. This is analyzed in the next section.

7.4. Reflection spectra from an array of cross-shaped apertures with rounded corners

Figure 7.14 depicts the cross-shaped apertures with rounded corners. The dimensions of the aperture and the periodicity are similar to the cross-shaped presented above (Figure 7.7): $w = 20$ nm, $h = 300$ nm, $T = 140$ nm, and $P = 400$ nm.

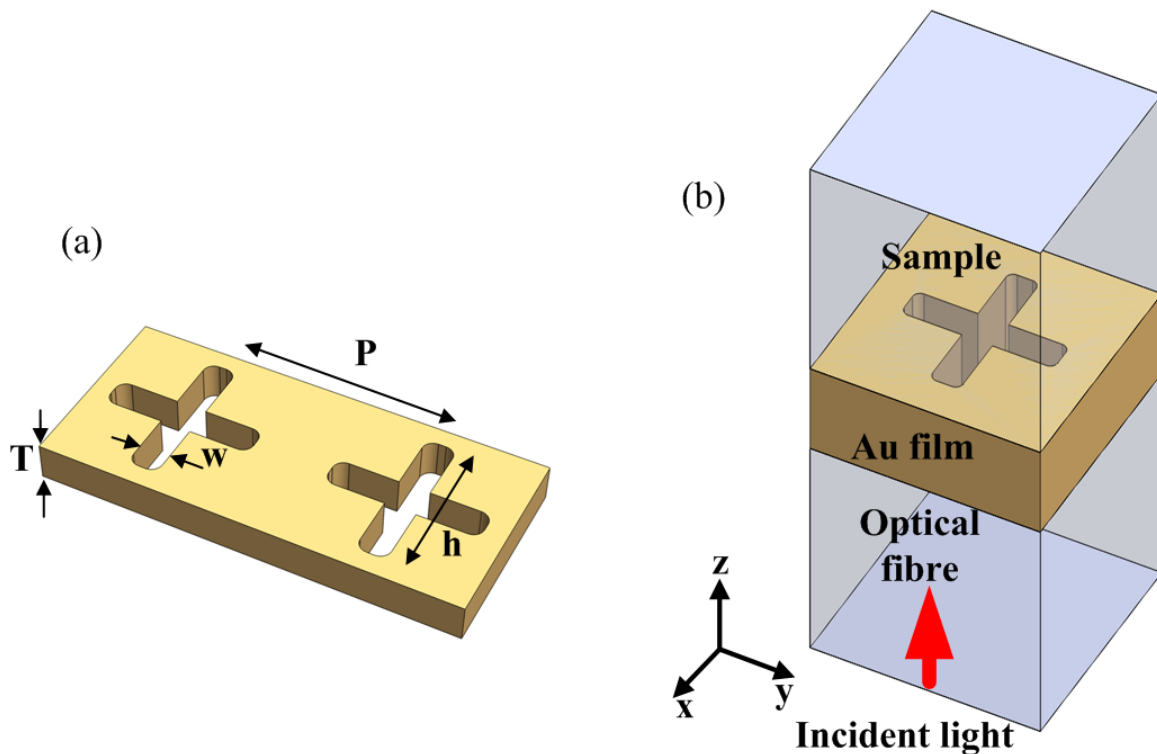


Figure 7.16: (a) An illustration of the dimensioning system used in a cross-shaped array with rounded corners on the end-face of a single mode fibre, (b) A unit cell representation for the simulation purposes.

The resonance spectra of the cross-shaped (rounded corners) array were simulated as the index of the of the material interacting with the sensing area of the fibre end-face was varied. As shown in Figure 7.17, the simulated resonances underwent a red-shift as the refractive index surrounding them was increased from 1.33 to 1.47.

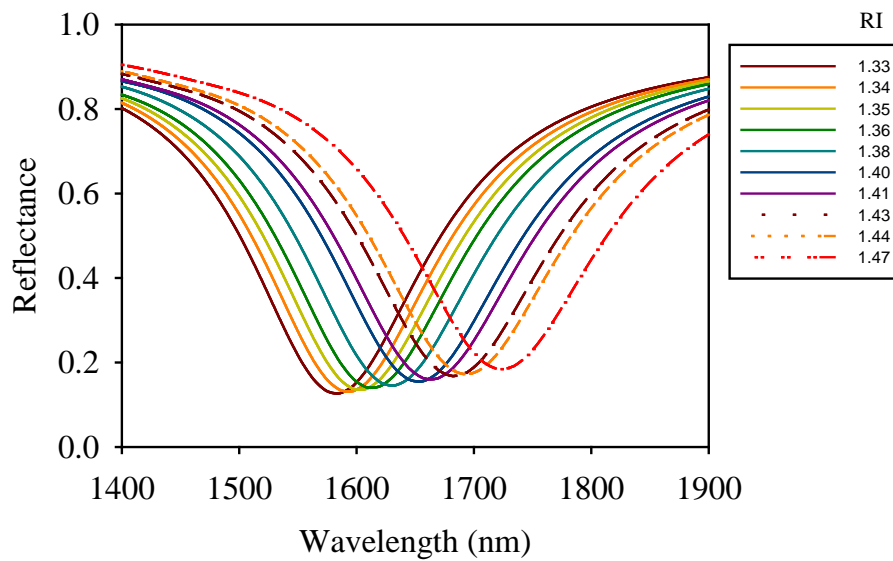


Figure 7.17: FDTD calculations of the reflected power spectra for the fibre sensor in various liquids of the rounded corners cross-shaped structure with $T = 140$ nm, periodicity $P = 400$ nm, length $h = 300$ nm and width $w = 20$ nm.

When the minimum dip wavelength for each liquid was plotted against the RI, as shown in Figure 7.16, a straight line could be fitted to the calculation points. This linear relationship between the shift of minimum in the reflection spectrum λ_{\min} and the change of RI of the surrounding medium provided a sensitivity of approximately 1001 ± 29 nm/RIU.

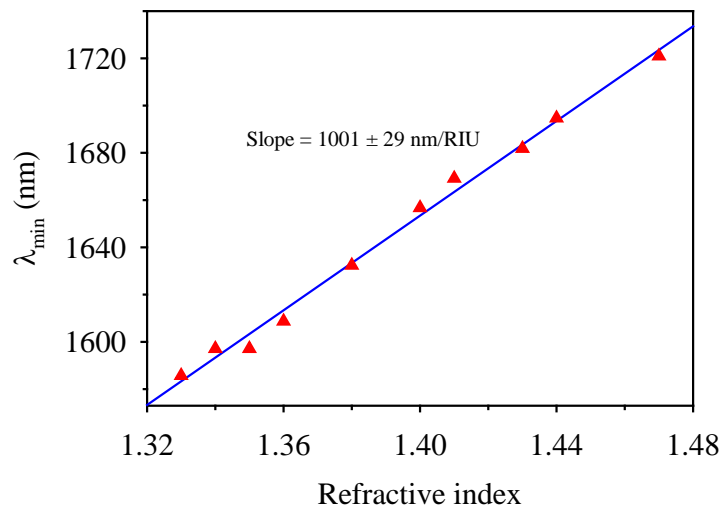


Figure 7.18: Dependence of SPR dip wavelength on the index of refraction of various liquids, showing the linear fit. The rounded corners cross-shaped parameters: $T = 140$ nm, $P = 400$ nm, $h = 300$ nm and $w = 20$ nm

Comparing Figure 7.14 with Figure 7.17, the effect of the rounded corners due the fabrication process on the sensor sensitivity is small but identifiable. The sensitivity is reduced from $\sim 1019 \pm 30$ nm/RIU for the sharper corners to $\sim 1001 \pm 29$ nm/RIU for the rounded corners cross-shaped array, as shown in Figures 7.15 and 7.18, respectively.

7.5. Reflection spectra from an array of annular apertures

In a similar manner, the results of reflection spectra and sensor sensitivities can be determined with the annular array of sub-wavelength apertures for a RI range 1.33 - 1.47.

Figure 7.19 depicts the annular apertures. The dimensioning system used for the annular array of apertures are as follow: gold thickness (T), inside (inner) diameter (D_{in}), outside (outer) diameter (D_{out}) and periodicity (P). Air was chosen for the sample in the initial simulations.

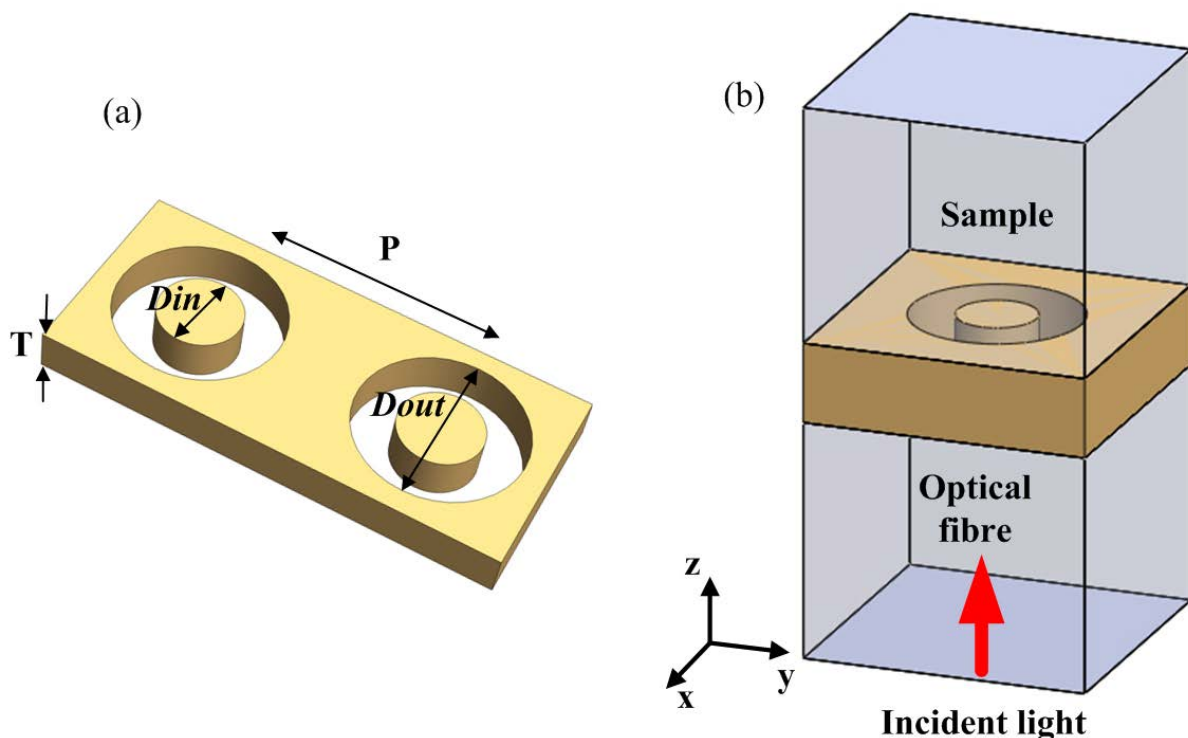


Figure 7.19: (a) An illustration of the dimensioning system used in an array of annular apertures on the end-face of a single mode fibre, (b) A unit cell representation for the simulation purposes.

Firstly, by varying the size of the inside diameter D_{in} , the reflection spectra as a function of wavelength for an annular array of a fixed periodicity P of 500 nm, an outside diameter D_{out} of 200 nm and a thickness T of 100 nm were obtained, as shown in Figure 7.20(a). It can be seen also from Figure 7.20(a) that increasing the inside diameter of the annular array leads to a broader resonant dip and a red-shift in the resonant wavelength.

By varying the size of the outside diameter D_{out} of the annular array, the reflection spectra as a function of wavelength of a fixed P of 500 nm, D_{in} of 80 nm and T of 100, are shown in Figure 7.20(b). Although Figure 7.20(b) shows that as the outside diameter increases, the resonant dip becomes broader but the red-shift in with the resonant wavelength is less rapid.

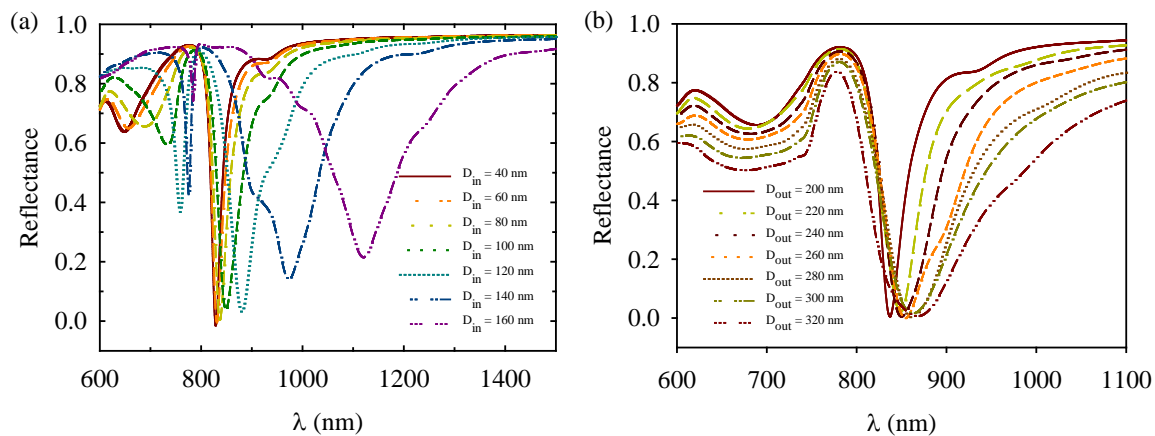


Figure 7.20: FDTD calculations of the reflectance intensity through an annular array with (a) the inner diameter, D_{in} , varying from 40 to 160 nm while P , D_{out} and T remained at 500, 200 and 100 nm, respectively; (b) the outer diameter, D_{out} , varying from 200 nm to 320 nm while P , T and D_{in} remained at 500, 100 and 80 nm, respectively.

Similarly, by varying the size of the periodicity of the array and the thickness of the gold layer, further reflection spectra were obtained, as shown in Figures 7.21(a) and 7.21(b), respectively.

Comparison of Figures 7.20(a) and 7.21(a) shows one difference in the reflection profile and that is the resonant dip becomes narrower as the periodicity increases whereas the resonant dip becomes broader as the inside diameter increases. Comparison of Figures 7.20(b) and 7.21(b) also yields a contrast and that is as the film thickness increases, the resonant dip becomes narrower and broader as outside diameter increases.

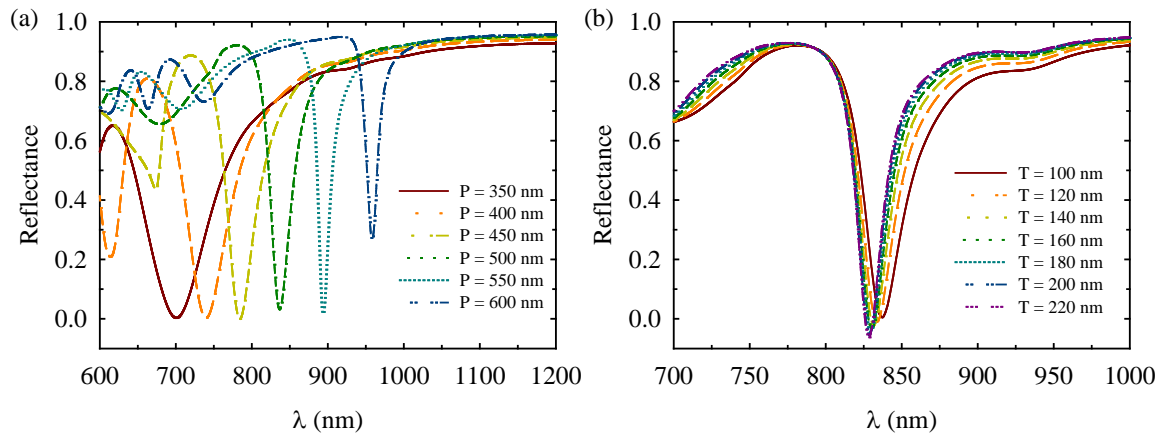


Figure 7.21: FDTD calculations of the reflectance intensity through an annular array with (a) the periodicity, P , varying from 350 to 600 nm while D_{in} , D_{out} and T remained at 80, 200 and 100 nm, respectively; (b) the thickness, T , varying from 100 to 220 nm while P , D_{out} and D_{in} remained at 500, 200 and 80 nm, respectively.

In a similar manner to the above, an investigation into the effect of this structure on the sensor sensitivity was carried out. Figure 7.22 shows the resonance spectra versus wavelength when the medium surrounding the fibre end-face interacted with various liquids (1.33 - 1.47).

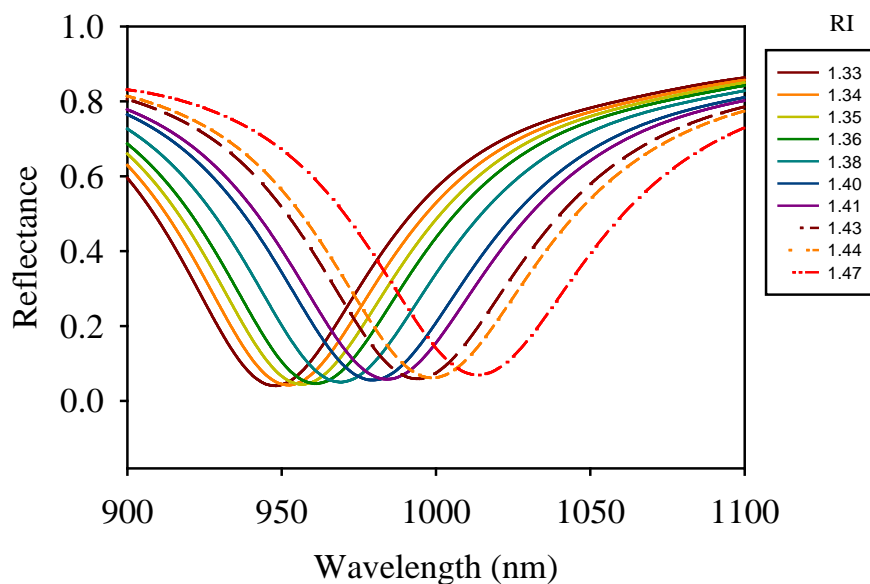


Figure 7.22: FDTD calculations of the reflected power spectra for the fibre sensor in various liquids with the gold film thickness $T = 100$ nm, periodicity $P = 500$ nm, inner diameter $D_{in} = 100$ nm and outer diameter $D_{out} = 200$ nm.

When the minimum dip wavelength for each liquid was plotted against the RI (between 1.33 - 1.47), as shown in Figure 7.23, a straight line could be fitted to the calculation points. The linear relationship between the shift of minimum in the reflection spectrum λ_{\min} and the assuming change of RI of the surrounding medium would be obtained, with a sensitivity of approximately 468 ± 11 nm/RIU.

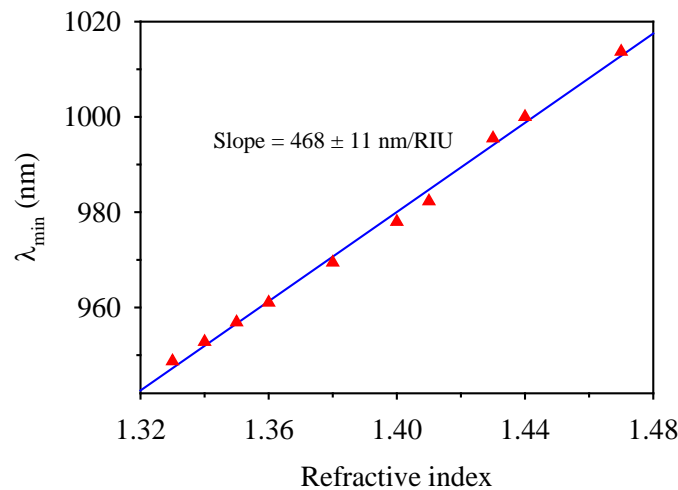


Figure 7.23: Dependence of SPR dip wavelength on the index of refraction of various liquids, showing the linear fit. The annular parameters: $T = 100$ nm, periodicity $P = 500$ nm, inner diameter $D_{\text{in}} = 100$ nm and outer diameter $D_{\text{out}} = 200$ nm.

Similarly, by increasing the inside diameter from 100 nm to 120 nm for an array of annular apertures with the following parameters: $T = 100$ nm, $P = 500$ nm, $D_{\text{in}} = 120$ nm, and $D_{\text{out}} = 200$ nm, a plot of reflection spectra versus wavelength would be obtained, as shown in Figure 7.24. The linear relationship between the resonant dips and refractive indices is shown in Figure 7.25.

Comparing Figures 7.22 and 7.24, one can observe that the wavelength range has been red-shifted from ($\sim 950 - 1014$ nm) to ($\sim 1023 - 1105$ nm) as the inside diameter increases from 100 nm to 120 nm. This diameter increase leads to an increase in the sensitivity from approximately 468 ± 11 nm/RIU to 567 ± 13 nm/RIU, as shown in Figures 7.23 and 7.25.

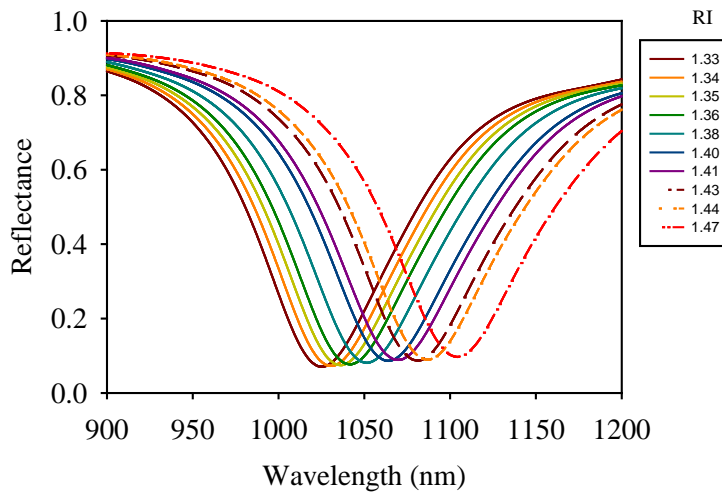


Figure 7.24: FDTD calculations of the reflected power spectra for the fibre sensor in various liquids with the following annular array parameters: $T = 100$ nm, $P = 500$ nm, $D_{in} = 120$ nm and $D_{out} = 200$ nm.

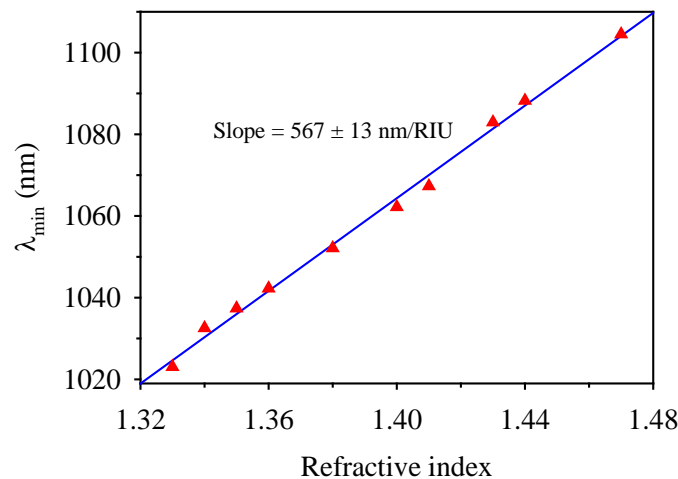


Figure 7.25: Dependence of SPR dip wavelength on the index of refraction of various liquids, showing the linear fit. The annular array parameters: $T = 100$ nm, $P = 500$ nm, $D_{in} = 120$ nm and $D_{out} = 200$ nm.

7.6. Reflection spectra from an array of rectangular apertures

The same procedure is again repeated, except, this time the arrays of rectangular apertures are considered. The FDTD simulation of an array of rectangular apertures on the end-face of an optical fibre begins with a setup as shown in Figure 7.26.

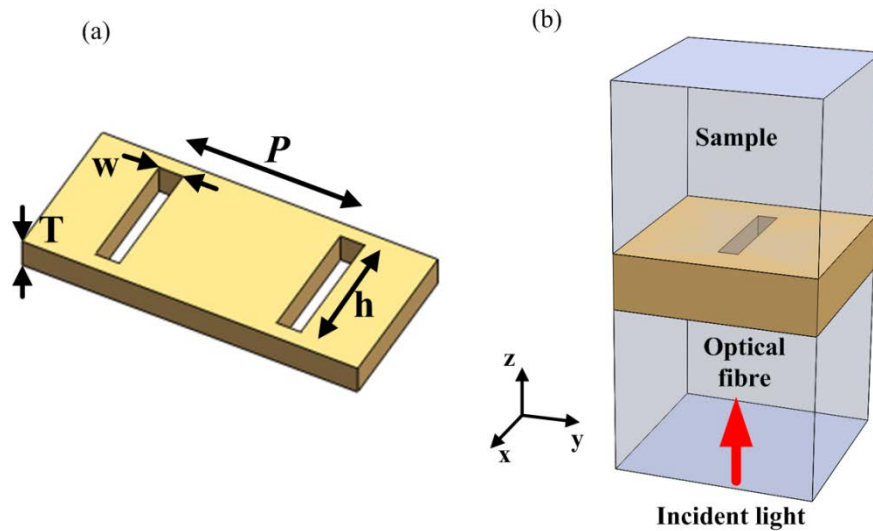


Figure 7.26: (a) An illustration of the geometry used in an array of rectangular apertures on the end-face of a single mode fibre, (b) A unit cell representation for simulation purposes.

Figure 7.27 shows the reflection as a function of wavelength for an array of rectangular sub-wavelength apertures of a fixed thickness of 140 nm, length of 300 nm and a periodicity of 500 nm. It indicates that as the width of the rectangular aperture decreases, the resonant dip weakens and there is a strong red-shift in the resonant wavelength.

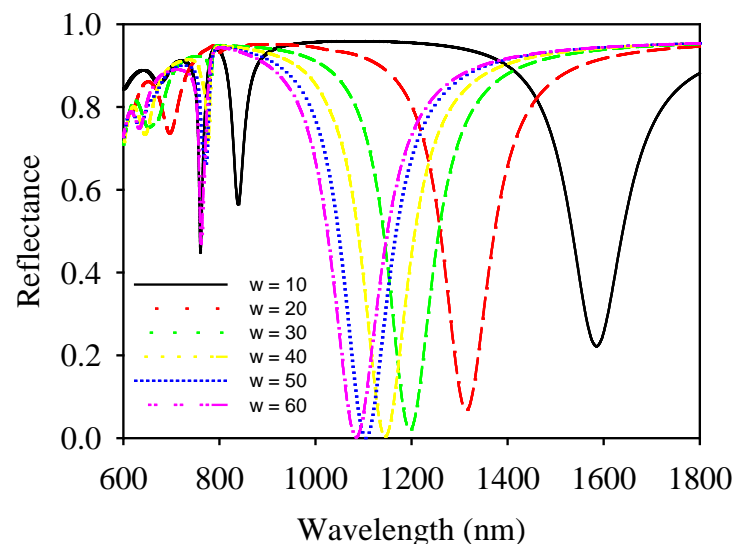


Figure 7.27: FDTD calculations of the reflectance intensity through a cross-shaped array with the width, w varying from 10 to 60 nm while h , T and P were kept constant at 300, 140 and 500 nm, respectively.

Comparing Figure 7.27 to Figure 7.9(b), one observes the similarity in the reflection spectra resulting from the fact that an array of rectangular apertures is similar to an array of cross-shaped apertures with TE polarization.

An investigation into the effect of this structure (with the following parameters: $h = 300$ nm, $T = 140$ nm, $w = 20$ nm, and $P = 400$ nm) on the sensor sensitivity was carried out. Figure 7.28 shows the resonance spectra versus wavelength when the medium surrounding the fibre end-face interacted with various liquids (1.33 - 1.47).

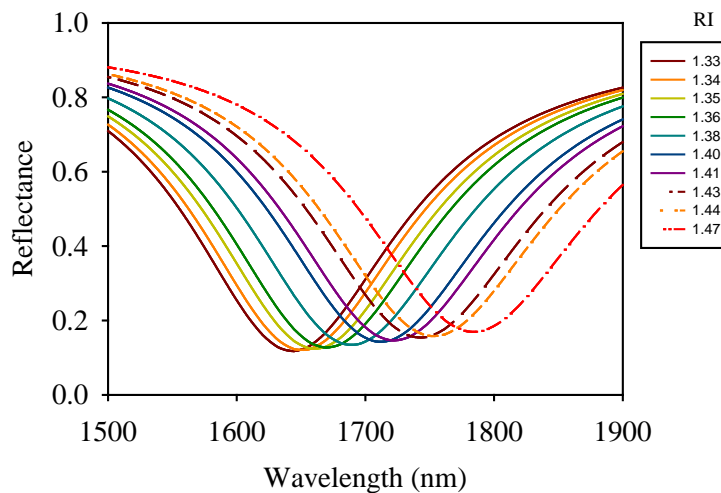


Figure 7.28: FDTD calculations of the reflected power spectra for the fibre sensor in various liquids with the rectangular array parameters: $T = 140$ nm, $P = 400$ nm, $h = 300$ nm and $w = 20$ nm.

The linear relationship between the shift of minimum in the reflection spectrum λ_{\min} and the assuming change of RI of the surrounding medium is shown in Figure 7.29. A sensitivity of approximately 1027 ± 35 nm/RIU would be obtained.

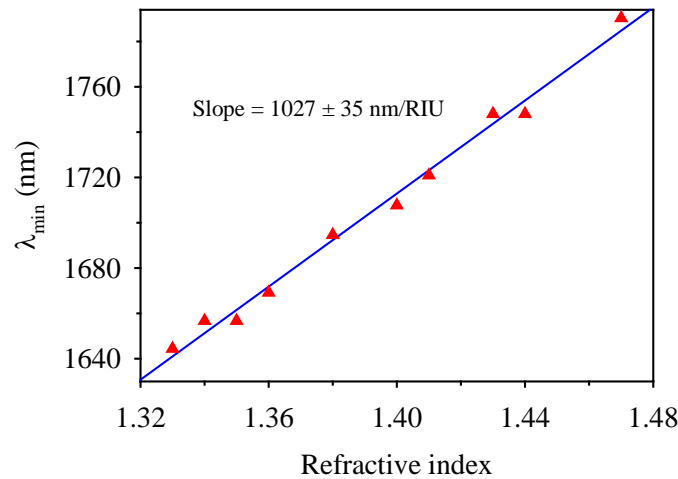


Figure 7.29: Dependence of SPR dip wavelength on the index of refraction of various liquids, showing the linear fit. The rectangular array parameters: $T = 140$ nm, $P = 400$ nm, $h = 300$ nm and $w = 20$ nm.

The above findings suggest that the sensitivity of the OFS would increase by $\sim 8 \pm 5$ nm/RIU when an array of rectangular apertures is used instead of an array of cross-shaped apertures of the same periodicity, gold layer thickness, length, and width, as shown in Figures 7.18 and 7.29.

The performances of sub-wavelength apertures used on the optical fibre end-face are summarized in Table 7.1 for an RI range: 1.33 - 1.38, and for an RI range: 1.33 - 1.47 are summarized in Table 7.2

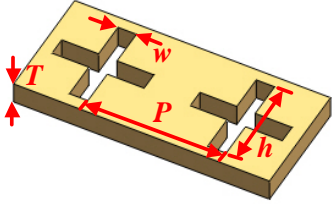
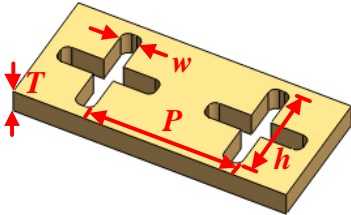
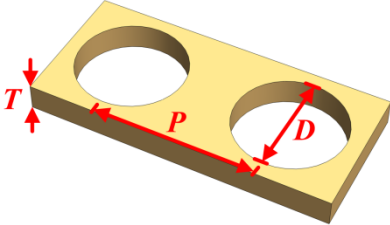
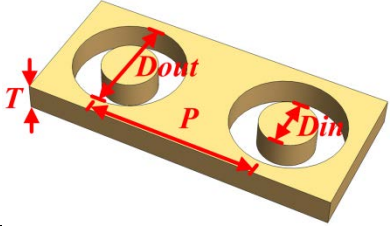
Aperture shape	Aperture size (nm)	Wavelength range (nm)	Sensitivity (nm/RIU)
	T, P, w, h <u>w changes:</u> 140, 500, 30, 300 140, 500, 40, 300 <u>h changes:</u> 140, 500, 20, 150 140, 500, 20, 200 <u>P changes:</u> 140, 400, 20, 300 140, 440, 20, 300 140, 500, 20, 300 <u>T changes:</u> 180, 500, 20, 300 220, 500, 20, 300	~1432 - 1480 ~ 1353 - 1387 ~ 961 - 987 ~ 1162 - 1200 ~ 1608 - 1657 ~ 1597 - 1644 ~ 1597 - 1644 ~ 1597 - 1644 ~ 1047 - 1078	~ 996 ~ 694 ~ 541 ~ 796 ~ 985 ~ 1013 ~ 1013 ~ 971 ~ 644
	T, P, w, h 140, 400, 20, 300	~ 1586 - 1632	~ 957
	T, P, D <u>D changes:</u> 140, 500, 220 140, 500, 280 140, 500, 300 <u>P changes:</u> 140, 440, 300 140, 460, 300 <u>T changes:</u> 180, 500, 300 220, 500, 300	~ 857 - 867 ~ 899 - 914 ~ 916 - 930 ~ 841 - 857 ~ 864 - 881 ~ 902 - 917 ~ 899 - 914	~ 212 ~ 304 ~ 359 ~ 339 ~ 358 ~ 319 ~ 304
	T, P, D_{in}, D_{out} <u>D_{in} changes:</u> 100, 500, 100, 200 100, 500, 120, 200 100, 500, 140, 200	~ 949 - 969 ~ 1033 - 1057 ~ 1156 - 1187	~ 433 ~ 513 ~ 645

Table 7.1: Metallic sub-wavelength apertures investigated in this thesis and their performance with respect to sensor sensitivity for an RI range 1.33 - 1.38.

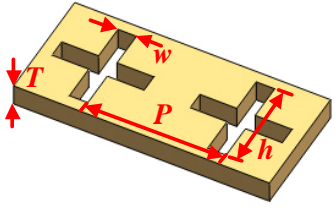
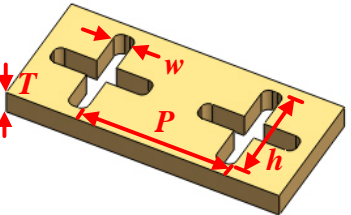
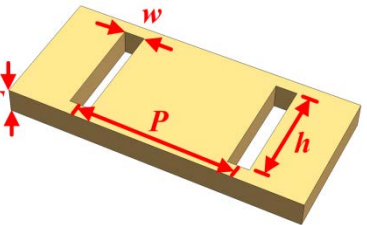
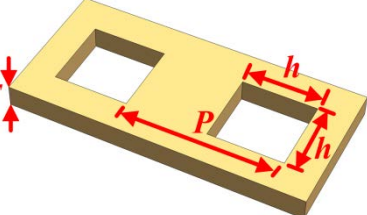
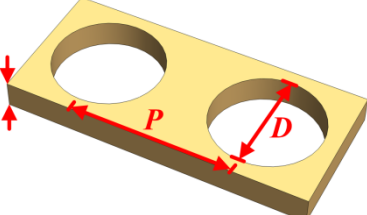
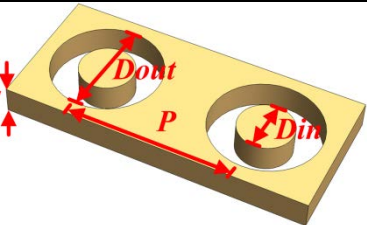
Aperture shape	Aperture size (nm)	Wavelength range (nm)	Sensitivity (nm/RIU)
	T, P, w, h 140, 400, 20, 300 140, 500, 20, 300	$\sim 1609 - 1748$ $\sim 1597 - 1734$	$\sim 1019 \pm 30$ $\sim 973 \pm 20$
	T, P, w, h 140, 400, 20, 300	$\sim 1586 - 1721$	$\sim 1001 \pm 29$
	T, P, w, h 140, 400, 300, 20	$\sim 1644 - 1793$	$\sim 1027 \pm 35$
	T, P, h 140, 500, 300	$\sim 957 - 1023$	465 ± 13
	T, P, D 140, 500, 300	$\sim 910 - 965$	$\sim 373 \pm 16$
	T, P, D_{in}, D_{out} <u>D_{in} changes:</u> 100, 500, 100, 200 100, 500, 120, 200 100, 500, 140, 200	$\sim 950 - 1014$ $\sim 1023 - 1104$ $\sim 1156 - 1254$	$\sim 468 \pm 11$ $\sim 567 \pm 13$ $\sim 715 \pm 12$

Table 7.2: Metallic sub-wavelength apertures investigated in this thesis and their performance with respect to sensor sensitivity for an RI range 1.33 - 1.47.

In this chapter, the spectral reflection properties of optical fibre surface plasmon resonance sensors based on a metallic sub-wavelength apertures were investigated. The properties of such a sensor were studied in details using the FDTD technique. The results showed that a tailored parameter (e.g. length, width, periodicity) combination may improve the sensitivity of a sensor and determine a design wavelength range. The effects of the fabricated sensor shape and size artefacts on sensor performance were also studied. The different in sensor's sensitivity between an artefact of fabrication and a true structure were identified, e.g. a sensitivity of approximately 18 nm/RIU difference between a cross-shaped array and a rounded cross-shaped array (Table 7.2), whereas an estimated 90 nm/RIU difference between a square array and a circular array having the same dimension and periodicities (Table 7.2). The highest sensitivity achieved were:

- approximately 1027 ± 35 nm/RIU for an array of rectangular sub-wavelength apertures (RI range: 1.33 - 1.47), and
- approximately 1013 nm/RIU for a cross-shaped array of sub-wavelength apertures (RI range: 1.33 - 1.38).

Table 7.2 also indicated that an array of circular apertures with a diameter (D) = 300 nm produced a lower sensitivity (373 ± 16 nm/RIU) compared to an array of square apertures of similar length (h) = 300nm with a higher sensitivity (465 ± 13 nm/RIU). In both of these cases, a change in periodicity (P) led to a huge change in resonance wavelength. However when the length of one side of a square aperture was reduced, the aperture became a rectangular aperture. A rectangular aperture was a special case of a cross-shaped aperture due to the polarization effect as was discussed in section 7.3. This polarization was the main reason behind the switch in the parameters of an array that were responsible to a large change in resonance wavelength.

Chapter 8. Conclusion and Outlook

This dissertation explored the possibility of developing optical fibre sensors based on the application of an array of metallic sub-wavelength apertures as a sensitive material placed at the end-face of an optical fibre. The unusual phenomenon of higher optical transmission than expected by the classical aperture theory makes these nanostructures a very attractive option for optical sensing.

Metallic sub-wavelength apertures arranged in a periodic array pattern were examined in detail to provide design specification for optical fibre liquid RI sensors. These sub-wavelength apertures were modelled using the commercial finite-domain time-difference software developed by Lumerical Solutions, Inc. Comparison of data calculated from the model with experimentally measured data confirmed the validity of the model for metallic sub-wavelength apertures embedded on the optical fibre end-face. Here the metal selected was a gold thin film with thickness much less than the wavelength under consideration. A sensor design for a liquid RI sensor with a sensitivity of ~ 985 nm/RIU, and a wavelength range of $\sim 1520 - 1575$ nm was undertaken and completed (Chapter 6).

Due to the high FIB milling cost of these sensors, it is not feasible to explore the sensor sensitivity experimentally for the multitude sub-wavelength apertures and configurations. The FDTD simulation technique was employed to investigate the three most popular sub-wavelength apertures (i.e. cross-shaped, annular, circular and rectangular) which recently have been shown to produce promising experimental results for the measurement of refractive index. The simulations performed were based on a detailed study of the experimental requirements of a real sensor taking into consideration the challenges of the fabrication process. Specifically, the geometrical parameters, such as shape, size, and array periodicity, that influence the optical properties of the array of metallic nanostructure when placed at the end-face of an optical fibre were analysed. In the case of the cross-shaped or rectangular arrays, by varying the width and length of the aperture, one would observe a significant shift in the resonant wavelength. However, for the case of circular or annular arrays, the changing of periodicity of the array was the main factor that produced a significant shift in the resonant wavelength. Other parameters also played an important role in determining the reflection profile. For example, if one needs to sharpen the resonance (i.e. reducing the full width at half maximum), an increase in the film thickness is necessary.

The rectangular nanostructure array produced the highest sensitivity of approximately 1027 ± 35 nm/RIU according to the simulation (Table 7.2). However, the cross-shaped nanostructure array presented a favourable sensitivity of approximately 1013 nm/RIU according to the simulation (Table 7.1). Taking into account the uncertainties of the sensitivity slope, the cross-shaped nanostructure array performed the best out of the four nanostructures. These values are not as high as reported by some other groups [95,103,115-117] (Table 3.1) but are superior to some of the recently reported sensors [12-14] which had similar sensor configurations.

The design of the optical fibre liquid refractive sensors consisted of an extensive systematic examination of sub-wavelength apertures in order to better understand the reflection spectral profiles that result from various shapes and dimensions, and array periodicities. This was done for an array embedded on the optical fibre end-faces. Water, propane, ether, acetone, hexane, IPA, octane, decane, propylene glycol and chloroform were considered as the medium surrounding the fibre end-face, thereby enabling the RI range from 1.33 to 1.47 to be considered.

An important issue arose when comparing experimental data with the simulations for cross-shaped apertures. It would appear that the significant difference between the two is best explained by considering the effect of surface tension in inhibiting a liquid from entering the apertures as was discussed in Chapter 6. This represents a serious limitation in the confidence that might be placed on the likelihood of developing a robust optical fibre sensor based on sub-wavelength apertures.

Given:

1. The sensitivity of proposed sensors are not superior to other existing optical fibre sensor technologies;
2. The cost of fabrication and difficulties in manufacturing compared to other cheaper and simpler technologies, and;
3. Difficulties with surface tension as outlined above;

it is highly unlikely that this type of optical fibre sensor will be widely adopted.

The employment of metal nanoparticles [216,217] instead of sub-wavelength apertures (nano cavities) which could reduce issues related to the surface tension between the liquid and the metal have been explored by some researchers and may represent a superior approach.

Appendix A

```
#####  
# Script file: t180p400d200_nanoholes_array.lsf  
#  
# Description: This script calculates the transmission vs. wavelength  
# for the file t180p400d200_nanoholes_array.fsp. It also  
# creates plots of field profiles  
#####  
# calculate the transmission as a function of wavelength  
load("t180p400d200_nanoholes_array.fsp");  
T1=transmission("transmission");  
load("t180p400d200_nanoholes_array_reference.fsp");  
T2=transmission("transmission");  
f=getdata("transmission","f");  
lambda=c/f;  
a=lambda*1e9;  
plot(a,T1,T2,T1*0.1+T2);  
data_to_print1=[a,T1];  
data_to_print2=[a,T2];  
data_to_print3=[a,(T1*0.012+T2*0.988)];  
write("T1.txt",num2str(data_to_print1));  
write("T2.txt",num2str(data_to_print2));  
write("T3.txt",num2str(data_to_print3));
```

Appendix B

```
#####  
# Script file: t140p400h300w20_cross_shaped_array.lsf  
#  
# Description: This script calculates the reflection vs. wavelength  
# for the file t140p400h300w20_cross_shaped_array.fsp. It also  
# creates plots of field profiles.  
#  
#####  
# calculate reflection as a function of wavelength  
load("t140p400h300w20_cross_shaped_array.fsp");  
R1=-transmission("reflection");  
load("t140p400h300w20_cross_shaped_array_reference.fsp");  
R2=-transmission("reflection");  
f=getdata("reflection", "f");  
lambda=c/f;  
a=lambda*1e9;  
plot(a,R1,R2,R1*0.1+R2);  
data_to_print1=[a,R1];  
data_to_print2=[a,R2];  
data_to_print3=[a,(R1*0.012+R2*0.988)];  
write("R1.txt",num2str(data_to_print1));  
write("R2.txt",num2str(data_to_print2));  
write("R3.txt",num2str(data_to_print3));
```

Bibliography

- [1] Grattan, K. T. V. and Meggitt, B. T. (eds), *Optical fibre sensor technology*, Chapman & Hall, London, (1995).
- [2] Raether, H., [Surface plasmons on smooth and rough surfaces and on gratings], Springer, New York, (1988).
- [3] Barnes, W. L., Dereux, A. and Ebbesen, T. W., "Surface plasmon subwavelength optics," *Nature* 424, 824-830 (2003).
- [4] <http://www.biacore.com>.
- [5] Sharma, A. K, Jha, R. and Gupta, B. D., "Fiber-optic sensors based on surface plasmon resonance: a comprehensive review," *IEEE Sensors* 7(8), 1118-1129 (2007).
- [6] Kanso, M., Cuenot, S. and Louarn, G., "Sensitivity of optical fiber sensor based on surface plasmon resonance: modelling and experiments," *Plasmonics* 3(2-3), 49-57 (2008).
- [7] Gupta, B. D. and Verma, R. K., "Surface plasmon resonance-based fiber optic sensors: principle, probe designs, and some applications," *Journal of Sensors* 2009, 1-12 (2009).
- [8] Ebbesen, T. W., Lezec, H. J., Ghaemi, H. F., Thio, T. and Wolff, P. A., "Extraordinary optical transmission through sub-wavelength hole arrays," *Nature* 391, 667-669 (1998).
- [9] Bethe, H. A., "Theory of diffraction by small holes," *Physical Review* 66(7-8), 163-182 (1944).

- [10] Anker, J. N., Hall, W. P., Lyandres, O., Shah, N. C., Zhao, J. and Van Duyne, R. P., "Biosensing with plasmonic nanosensors," *Nature Materials* 7, 442-453 (2008).
- [11] Jain, P. K. and El-Sayed, M. A., "Plasmonic coupling in noble metal nanostructures," *Chemical Physics Letters* 487(4-6), 153-164 (2010).
- [12] Smythe, E. J., Cubukcu, E. and Capasso, F., "Optical properties of surface plasmon resonances of coupled metallic nanorods," *Optics Express* 15(12), 7439-7447 (2007).
- [13] Dhawan, A., Gerhold, M. and Muth, J., "Plasmonic structures based on subwavelength apertures for chemical and biological sensing applications," *IEEE Sensors Journal* 8(6), 942-950 (2008).
- [14] Lin, Y., Zou, Y. and Lindquist, R. G., "A reflection-based localized surface plasmon resonance fiber-optic probe for biochemical sensing," *Biomedical Optics Express* 2(3), 478-484 (2011).
- [15] Snyder, A. W. and Love, J. D., [Optical waveguide theory], Chapman and Hall, New York, (1983).
- [16] Harrick, N. J. (ed.) *Electromagnetic wave pattern near a reflecting interface*, in *Internal reflection spectroscopy*, Interscience Publishers, New York, (1967).
- [17] Wolfbeis, O. S., "Fiber-optic chemical sensors and biosensors," *Analytical Chemistry* 76(12), 3269-3284 (2004).
- [18] Stewart, G., Jin, W. and Culshaw, B., "Prospects for fibre-optic evanescent-field gas sensors using absorption in the near-infrared," *Sensors and Actuators B: Chemical* 38(1-3), 42-47 (1997).

- [19] Chan, K., Ito, H. and Inaba, H., "An optical-fiber-based gas sensor for remote absorption measurement of low-level CH₄ gas in the near-infrared region," *Journal of lightwave technology* 2(3), 234-237 (1984).
- [20] Rowe-Taitt, C. A. and Ligler, F. S., 'Fibre optic biosensors', in Lopez-Higuera, JM (ed.), *Handbook of optical fibre sensing technology*, John Wiley & Sons, pp. 687-700 (2001).
- [21] Ferguson, J. A., Boles, T. C, Adams, C. P. and Walt, D. R., "A fiber-optic DNA biosensor microarray for the analysis of gene expression," *Nature Biotechnology* 14, 1681-1684 (1996).
- [22] Healy, B. G., Li, L. and Walt, D. R., "Multianalyte biosensors on optical imaging bundles," *Biosensors and Bioelectronics* 12(6), 521-529 (1997).
- [23] Barker, S. L. R., Kopelman, R., Meyer, T. E. and Cusanovich, M. A., "Fiber-optic nitric oxide-selective biosensors and nanosensors," *Analytical Chemistry* 70(5), 971-976 (1998).
- [24] Holst, G. and Mizaikoff, B., 'Fibre optic sensors for environmental applications', in Lopez-Higuera, JM (ed.), *Handbook of optical fibre sensing technology*, John Wiley & Sons, pp. 729-749 (2001).
- [25] Dietrich, A. M., Jensen, J. N. and da Costa, W. F., "Measurement of pollutants: chemical species," *Water environmental research* 68(4), 391-406 (1996).
- [26] Schweizer, G., Latka, I., Lehmann, H. and Willsch, R., "Optical sensing of hydrocarbons in air or in water using UV absorption in the evanescent field of fibers," *Sensors and Actuators B: Chemical* 38(1-3), 150-153 (1997).
- [27] Mizaikoff, B., Taga, K. and Kellner, R., "Infrared fiber optic gas sensor for chlorofluorohydrocarbons," *Vibrational Spectroscopy* 8(2), 103-108 (1995).

- [28] Archenault, M., Gagnaire, H., Goure, J. P. and Jaffrezic-Renault, N., "A simple intrinsic optical fibre refractometer," *Sensors and Actuators B: Chemical* 5(1-4), 173-179 (1991).
- [29] Egami, C., Takeda, K., Isai, M. and Ogita, M., "Evanescent-wave spectroscopic fiber optic pH sensor," *Optics Communications* 122(4-6), 122-126 (1996).
- [30] Trolier-McKinstry, S., Fox, G. R., Kholkin, A., Muller, C. A. P. and Setter, N., "Optical fibers with patterned ZnO/electrode coatings for flexural actuators " *Sensors and Actuators A: Physical* 73(3), 267-274 (1999).
- [31] Yuan, J. and El-Sherif, M. A., "Fiber-optic chemical sensor using polyaniline as modified cladding material," *IEEE Sensors* 3(1), 5-12 (2003).
- [32] Guo, H. and Tao, S., "An active core fiber-optic temperature sensor using an Eu(III)-doped sol-gel silica fiber as a temperature indicator," *IEEE Sensors Journal* 7(6), 953-954 (2007).
- [33] MacCraith, B. D., McDonagh, C. M., O'Keeffe, G., McEvoy, A. K., Butler, T. and Sheridan, F. R., "Sol-gel coatings for optical chemical sensors and biosensors," *Sensors and Actuators B: Chemical* 29(1-3), 51-57 (1995).
- [34] Yin, S., [Fiber optic sensors], 2nd edn, Taylor & Francis Group, CRC Press(2008).
- [35] Soloman, S., [Sensors Handbook], McGraw Hill 245-246 (2009).
- [36] Fuhr, P. L., "Measuring with light (in four parts)," *Sensors Magazine*, San Jose, CA(2000).

- [37] Allsop, T., Reeves, R., Webb, D. J., Bennion, I. and Neal, R., "A high sensitivity refractometer based upon a long period grating Mach-Zehnder interferometer," *Review of Scientific Instruments*(73), 1702-1705 (2002).
- [38] Patrick, H. J., Kersey, A. D. and Bucholtz, F., "Analysis of the response of long period fiber gratings to external index of refraction," *Journal of lightwave technology* 16(9), 1606-1612 (1998).
- [39] Iadicicco, A., Cusano, A., Campopiano, S., Cutolo, A. and Giordano, M., "Thinned fiber Bragg grating as refractive index sensors," *IEEE Sensors Journal* 5(6), 1288-1295 (2005).
- [40] Iadicicco, A., Campopiano, S., Cutolo, A., Giordano, M. and Cusano, A., "Refractive index sensor based on microstructured fiber Bragg grating," *IEEE Photonics Technology Letters* 17(6), 1250-1252 (2005).
- [41] Culshaw, B., Muhammad, F., Stewart, G., Murray, S., Pinchbeck, D., Norris, J., Cassidy, S., Wilkinson, M., Williams, D., Crisp, I., Van Ewyk, R. and McGhee, A., "Evanescent wave methane detection using optical fibres," *Electronics Letters* 28(24), 2232-2234 (1992).
- [42] Cox, F. M., Lwin, R., Large, M. C. J. and Cordeiro, C. M. B., "Opening up optical fibres," *Optics Express* 15(19), 11843-11848 (2007).
- [43] Newby, K., Reichert, W. M., Andrade, J. D. and Benner, R. E., "Remote spectroscopic sensing of chemical absorption using a single multimode optical fiber," *Applied Optics* 23(11), 1812-1815 (1984).
- [44] Kurihara, K., Ohkawa, H., Iwasaki, Y., Niwa, O., Tobita, T. and Suzuki, K., "Fiber-optic conical microsensors for surface plasmon resonance using chemically etched single-mode fiber," *Analytica Chimica Acta* 523(2), 165-170 (2004).

- [45] Chiu, M. H., Wang, S. F. and Chang, R. S., "D-type fiber biosensor based on surface-plasmon resonance technology and heterodyne interferometry," *Optics Letters* 30(3), 233-235 (2005).
- [46] Asawa, C. K., Yao, S. K., Stearns, R. C., Mota, N. L. and Downs, J. W., "High-sensitivity fibre-optic strain sensors for measuring structural distortion," *Electronics Letters* 18(9), 362-364 (1982).
- [47] Lagakos, N., Cole, J. H. and Bucaro, J. A., "Microbend fiber-optic sensor," *Applied Optics* 26(11), 2171-2180 (1987).
- [48] Lee, S. T., Aneeshkumar, B., Radhakrishnan, P., Vallabhan, C. P. G. and Nampoore, V. P. N., "A microbent fibre optic pH sensor," *Optics Communications* 205(4-6), 253-256 (2002).
- [49] Pandey, N. K. and Yadav, B. C., "Embedded fibre optic microbend sensor for measurement of high pressure and crack detection," *Sensors and Actuators A: Physical* 128(1), 33-36 (2006).
- [50] Luo, F., Liu, J., Ma, N. and Morse, T. F., "A fiber optic microbend sensor for distributed sensing application in the structural strain monitoring," *Sensors and Actuators A: Physical* 75(1), 41-44 (1999).
- [51] MacLean, A., Moran, C., Johnstone, W., Culshaw, B., Marsh, D. and Parker, P., "Detection of hydrocarbon fuel spills using a distributed fibre optic sensor," *Sensors and Actuators A: Physical* 109(1-2), 60-67 (2003).
- [52] Otsuki, S., Adachi, K. and Taguchi, T., "A novel fiber-optic gas-sensing configuration using extremely curved optical fibers and an attempt for optical humidity detection," *Sensors and Actuators B: Chemical* 53(1-2), 91-96 (1998).
- [53] Yeo, T. L., Sun, T. and Grattan, K. T. V., "Fibre-optic sensor technologies for humidity and moisture measurement," *Sensors and Actuators A: Physical* 144(2), 280-295 (2008).

- [54] Nath, P., Singh, H. K., Datta, P. and Sarma, K. C., "All-fiber optic sensor for measurement of liquid refractive index," *Sensors and Actuators A: Physical* 148(1), 16-18 (2008).
- [55] Ilev, I. K. and Waynant, R. W., "All-fiber-optic sensor for liquid level measurement," *Review of Scientific Instruments* 70(5), 2551-2554 (1999).
- [56] Komachiya, M., Fumino, T., Sakaguchi, T. and Watanabe, S., "Design of a sensing glass fiber with specific refractive-index composition for a system with 1.3 μm wavelength light source," *Sensors and Actuators A: Physical* 78(2), 172-179 (1999).
- [57] Stokes, D. L. and Vo-Dinh, T., "Development of an integrated single-fiber SERS sensor," *Sensors and Actuators B: Chemical* 69(1-2), 28-36 (2000).
- [58] Zhang, Y., Gu, C., Schwartzberg, A. M. and Zhang, J. Z., "Surface-enhanced Raman scattering sensor based on D-shaped fiber," *Applied Physics Letters* 87(12), 123105-123103 (2005).
- [59] Viets, C. and Hill, W., "Fibre-optic SERS sensors with angled tips," *Journal of Molecular Structure* 565-566(1-3), 515-518 (2001).
- [60] Lucotti, A. and Zerbi, G., "Fiber-optic SERS sensor with optimized geometry," *Sensors and Actuators B: Chemical* 121(2), 356-364 (2007).
- [61] Kostovski, G., White, D. J., Mitchell, A., Austin, M. W. and Stoddart, P. R., "Nanoimprinted optical fibres: Biotemplated nanostructures for SERS sensing," *Biosensors and Bioelectronics* 24(5), 1531-1535 (2008).
- [62] Jorgenson, R. C. and Yee, S. S., "A fiber-optic chemical sensor based on surface plasmon resonance," *Sensors and Actuators B: Chemical* 12(3), 213-220 (1993).

- [63] Trouillet, A., Ronot-Trioli, C., Veillas, C. and Gagnaire, H., "Chemical sensing by surface plasmon resonance in a multimode optical fibre," *Pure and Applied Optics* 5(2), 227-237 (1996).
- [64] Piliarik, M., Homola, J., Manikova, Z. and Ctyroky, J., "Surface plasmon resonance sensor based on a single-mode polarization-maintaining optical fiber," *Sensors and Actuators B: Chemical* 90(1-3), 236-242 (2003).
- [65] Tubb, A. J. C., Payne, F. P., Millington, R. B. and Lowe, C. R., "Single-mode optical fiber surface plasma wave chemical sensor," *Sensors and Actuators B: Chemical* 41(1-3), 71-79 (1997).
- [66] Shankaran, D. V., Gobi, K. V. and Miura, N., "Recent advancements in surface plasmon resonance immunosensors for detection of small molecules of biomedical, food and environmental interest," *Sensors and Actuators B: Chemical* 121(1), 158-177 (2007).
- [67] Wood, R. W., "On a remarkable case of uneven distribution of light in a diffraction grating," *Philosophical Magazine Series 6* 4(21), 396-402 (1902).
- [68] Fano, U., "The theory of anomalous diffraction gratings and of quasi-stationary waves on metallic surfaces (Sommerfeld's waves)," *Journal of the Optical Society of America* 31(3), 213-222 (1941).
- [69] Turbadar, T., "Complete absorption of light by thin metal films," *Proceedings of the Physical Society* 73(1), 40-44 (1959).
- [70] Otto, A., "Excitation of nonradiative surface plasma waves in silver by the method of frustrated total reflection " *Zeitschrift fur Physik A Hadrons and Nuclei* 216(4), 398-410 (1968).
- [71] Otto, A., "A new method for exciting nonradioactive surface plasma oscillations," *Physica Status Solidi (b)* 26(1), 99-101 (1968).

- [72] Kretschmann, E. and Raether, H., "Radiative decay of nonradiative surface plasmons excited by light," *Z. Naturforsch. A* 23, 2135-2136 (1968).
- [73] Liedberg, B., Nylander, C. and Lundstrom, I., "Surface plasmon resonance for gas detection and biosensing," *Sensors and Actuators* 4, 299-304 (1983).
- [74] Villuendas, F. and Pelayo, J., "Optical fibre device for chemical sensing based on surface plasmon excitation," *Sensors and Actuators A: Physical* 23(1-3), 1142-1145 (1990).
- [75] Tanahashi, I., Iwagishi, H. and Chang, G., "Localized surface plasmon resonance sensing properties of photocatalytically prepared Au/TiO₂ films," *Materials Letters* 62(17-18), 2714-2716 (2008).
- [76] Esteban, O., Naranjo, F. B., Diaz-Herrera, N., Valdueza-Felip, S., Navarrete, M. C. and Gonzalez-Cano, A., "High-sensitive SPR sensing with Indium Nitride as a dielectric overlay of optical fibers," *Sensors and Actuators B: Chemical* 158(1), 372-376 (2011).
- [77] Maier, S. A., [Plasmonics: fundamentals and applications], Springer, New York, (2007).
- [78] Ashcroft, N. W. and Mermin, N. D., [Solid state physics], Harcourt College, New York, (1976).
- [79] Johnson, P. B. and Christy, R. W., "Optical constants of the noble metals," *Physical Review B* 6(12), 4370-4379 (1972).
- [80] Goubau, G., "Surface waves and their application to transmission lines," *Journal of Applied Physics* 21(11), 1119-1128 (1950).
- [81] Ligler, F. S. and Taitt, C. R. (eds), *Optical biosensors: today and tomorrow*, Elsevier Science, (2008).

- [82] Ritchie, R. H., Arakawa, E. T., Cowanand, J. J. and Hamm, R. N., "Surface plasmon resonance effect in grating diffraction," *Physical Review Letters* 21(22), 1530-1533 (1968).
- [83] Homola, J., "Present and future of surface plasmon resonance biosensors," *Analytical Bioanalytical Chemistry* 377(3), 528-539 (2003).
- [84] Barnes, W. L., Murray, W. A., Dintinger, J., Devaux, E. and Ebbesen, T. W., "Surface plasmon polaritons and their role in the enhanced transmission of light through periodic arrays of subwavelength holes in a metal film," *Physical Review Letters* 92(10), 107401 (2004).
- [85] <http://www.sensata.com>.
- [86] <http://www.ecochemie.nl>.
- [87] <http://www.ibis-spr.nl>.
- [88] <http://www.reichert.com>.
- [89] <http://www.xantec.com>.
- [90] Luong, J. H. T., Male, K. B. and Glennon, J. D., "Biosensor technology: technology push versus market pull," *Biotechnology Advances* 26(5), 492-500 (2008).
- [91] Wang, S., Boussad, S. and Tao, N. J., "High-sensitivity stark spectroscopy obtained by surface plasmon resonance measurement," *Analytical Chemistry* 72(17), 4003-4008 (2000).
- [92] Tao, N. J., Boussad, S., Huang, W. L., Arechabaleta, R. A. and D'Agnesi, J., "High resolution surface plasmon resonance spectroscopy," *Review of Scientific Instruments* 70(12), 4656-4660 (1999).
- [93] Fan, X., White, I. M., Shopova, S. I., Zhu, H., Suter, J. D. and Sun, Y., "Sensitive optical biosensors for unlabeled targets: a review," *Analytica Chimica Acta* 620(1-2), 8-26 (2008).

- [94] Wolfbeis, O. S., "Fiber-optic chemical sensors and biosensors," *Analytical Chemistry* 80(12), 4269-4283 (2008).
- [95] Lee, B., Roh, S. and Park, J., "Current status of micro- and nano-structured optical fiber sensors," *Optical Fiber Technology* 15(3), 209-221 (2009).
- [96] Slavik, R., Homola, J. and Brynda, E., "A miniature fiber optic surface plasmon resonance sensor for fast detection of staphylococcal enterotoxin B," *Biosensors and Bioelectronics* 17(6-7), 591-595 (2002).
- [97] Homola, J., "Optical fiber sensor based on surface plasmon excitation," *Sensors and Actuators B: Chemical* 29(1-3), 401-405 (1995).
- [98] Tseng, S. M., Hsu, K. Y., Wei, H. S. and Chen, K. F., "Analysis and experiment of thin metal-clad fiber polarizer with index overlay," *IEEE Photonics Technology Letters* 9(5), 628-630 (1997).
- [99] Esteban, O., Alonso, R., Navarrete, M. C. and Cano, A. G., "Surface plasmon excitation in fiber-optics sensors: a novel theoretical approach," *Journal of lightwave technology* 20(3), 448-453 (2002).
- [100] Lin, G. C., Wang, L., Yang, C. C., Shih, M. C. and Chuang, T. J., "Thermal performance of metal-clad fiber Bragg grating sensors," *IEEE Photonics Technology Letters* 10(3), 406-408 (1998).
- [101] Schroeder, K., Ecke, W., Mueller, R., Willsch, R. and Andreev, A., "A fibre Bragg grating refractometer," *Measurement Science and Technology* 12(7), 757-764 (2001).
- [102] Sharma, A. K and Gupta, B. D., "Fiber optic sensor based on surface plasmon resonance with nanoparticle films," *Photonics and Nanostructures - Fundamentals and Applications* 3(1), 30-37 (2005).

- [103] Sharma, A. K and Gupta, B. D., "Fiber-optic sensor based on surface plasmon resonance with Ag-Au alloy nanoparticle films," *Nanotechnology* 17(1), 124-131 (2006).
- [104] Slavik, R., Homola, J., Ctyroky, J. and Brynda, E., "Novel spectral fiber optic sensor based on surface plasmon resonance," *Sensors and Actuators B: Chemical* 74(1-3), 106-111 (2001).
- [105] Hernandez, D. M. and Villatoro, J., "High-resolution refractive index sensing by means of a multiple-peak surface plasmon resonance optical fiber sensor," *Sensors and Actuators B: Chemical* 115(1), 227-231 (2006).
- [106] He, Y. J., Lo, Y. L. and Huang, J. F., "Optical-fiber surface-plasmon-resonance sensor employing long-period fiber gratings in multiplexing," *Journal of Optical Society of America B* 23(5), 801-811 (2006).
- [107] Nemova, G. and Kashyap, R., "Modeling of plasmon-polariton refractive-index hollow core fiber sensors assisted by a fiber Bragg grating," *Journal of lightwave technology* 24(10), 3789-3796 (2006).
- [108] Allsop, T., Neal, R., Rehman, S., Webb, D. J., Mapps, D. and Bennion, I., "Generation of infrared surface plasmon resonances with high refractive index sensitivity utilizing tilted fiber Bragg gratings," *Applied Optics* 46(22), 5456-5460 (2007).
- [109] Ronot-Trioli, C., Trouillet, A., Veillas, C. and Gagnaire, H., 'A monochromatic excitation of a surface plasmon resonance in an optical fibre refractive index sensor', paper presented to The 8th international conference on solid-state sensors and actuators and Eurosensors IX(1995).

- [110] Slavik, R., Homola, J. and Ctyroky, J., "Miniaturization of fiber optic surface plasmon resonance sensor," *Sensors and Actuators B: Chemical* 51(1-3), 311-315 (1998).
- [111] Phan Huy, M. C., Laffont, G., Frignac, Y., Dewynter-Marty, V., Ferdinand, P., Roy, P., Blondy, J. -M., Pagnoux, D., Blanc, W. and Dussardier, B., "Fibre Bragg grating photowriting in microstructured optical fibres for refractive index measurement," *Measurement Science and Technology* 17(5), 992-997 (2006).
- [112] Minkovich, V. P., Villatoro, J., Monzon-Hernandez, D., Calixto, S., Sotsky, A. B. and Sotskaya, L. I., "Holey fiber tapers with resonance transmission for high-resolution refractive index sensing," *Optics Express* 13(19), 7609-7614 (2005).
- [113] Chong, J. H., Shum, P., Haryono, H., Yohana, A., Rao, M. K., Lu, C. and Zhu, Y. , "Measurements of refractive index sensitivity using long-period grating refractometer," *Optics Communications* 229(1-6), 65-69 (2004).
- [114] Nemova, G. and Kashyap, R., "Theoretical model of a planar integrated refractive index sensor based on surface plasmon-polariton excitation with a long period grating," *Journal of Optical Society of America B* 24(10), 2696 - 2701 (2007).
- [115] Verma, R. K., Sharma, A. K and Gupta, B. D., "Surface plasmon resonance based tapered fiber optic sensor with different taper profiles," *Optics Communications* 281(6), 1486-1491 (2008).
- [116] Verma, R. K., Sharma, A. K and Gupta, B. D., "Modeling of tapered fiber-optic surface plasmon resonance sensor with enhanced sensitivity," *IEEE Photonics Technology Letters* 19(22), 1786-1788 (2007).

- [117] Zeng, J. and Liang, D., "Application of fiber optic surface plasmon resonance sensor for measuring liquid refractive index," *Journal of Intelligent Material Systems and Structures* 17(8-9), 787-791 (2006).
- [118] Wedge, S., Hooper, I. R., Sage, I. and Barnes, W. L., "Light emission through a corrugated metal film: the role of cross-coupled surface plasmon polaritons," *Physical Review B* 69(24), 245418 (2004).
- [119] Gifford, D. K. and Hall, D. G., "Extraordinary transmission of organic photoluminescence through an otherwise opaque metal layer via surface plasmon cross coupling," *Applied Physics Letters* 80(20), 3679-3681 (2002).
- [120] Srituravanich, W., Durant, S., Lee, H., Sun, C. and Zhang, X., "Deep subwavelength nanolithography using localized surface plasmon modes on planar silver mask," *Journal of Vacuum Science and Technology B* 23(6), 2636-2639 (2005).
- [121] Luo, X. and Ishihara, T., "Surface plasmon resonant interference nanolithography technique," *Applied Physics Letters* 84(23), 4780-4782 (2004).
- [122] Ghaemi, H. F., Thio, T., Grupp, D. E., Ebbesen, T. W. and Lezec, H. J., "Surface plasmons enhance optical transmission through subwavelength holes," *Physical Review B* 58(11), 6779-6782 (1998).
- [123] Grupp, D. E., Lezec, H. J., Ebbesen, T. W., Pellerin, K. M. and Thio, T., "Crucial role of metal surface in enhance transmission through subwavelength apertures," *Applied Physics Letters* 77(11), 1569-1571 (2000).
- [124] Schouten, H. F., Kuzmin, N., Dubois, G., Visser, T. D., Gbur, G., Alkemade, P. F. A., Blok, H., Hooft, G. W. 't, Lenstra, D. and Eliel, E. R.,

- "Plasmon-assisted two-slit transmission: Young's experiment revisited," *Physical Review Letters* 94(5), 053901 (2005).
- [125] Darmanyán, A. and Zayats, A. V., "Light tunneling via resonant surface plasmon polariton states and the enhanced transmission of periodically nanostructured metal films: An analytical study," *Physical Review B* 67(3), 035424 (2003).
- [126] Lalanne, P. and Hugonin, J. P., "Interaction between optical nano-objects at metallo-dielectric interfaces," *Nature Physics* 2, 551-556 (2006).
- [127] Liu, H. and Lalanne, P., "Microscopic theory of the extraordinary optical transmission," *Nature* 452, 728-731 (2008).
- [128] Cao, Q. and Lalanne, P., "Negative role of surface plasmons in the transmission of metallic gratings with very narrow slits," *Physical Review Letters* 88(5), 057403 (2002).
- [129] Lezec, H. J. and Thio, T., "Diffracted evanescent wave model for enhanced and suppressed optical transmission through subwavelength hole arrays," *Optics Express* 12(16), 3629-3651 (2004).
- [130] Degiron, A. and Ebbesen, T. W., "The role of localized surface plasmon modes in the enhanced transmission of periodic subwavelength apertures," *Journal of Optics A: Pure and Applied Optics* 7(2), S90-S96 (2005).
- [131] Eah, S. K., Jaeger, H. M., Scherer, N. F., Wiederrecht, G. P. and Lin, X. M., "Plasmon scattering from a single gold nanoparticle collected through an optical fiber," *Applied Physics Letters* 86(3), 031902 (2005).
- [132] Sarrazin, M., Vigneron, J. -P. and Vigoureux, J. -M., "Role of Wood anomalies in optical properties of thin metallic films with a bidimensional array of subwavelength holes," *Physical Review B* 67(8), 085415 (2003).

- [133] Genet, C., van Exter, M. P. and Woerdman, J. P., "Fano-type interpretation of red shifts and red tails in hole array transmission spectra," *Optics Communications* 225(4-6), 331-336 (2003).
- [134] Borisov, A. G., Garcia de Abajo, F. J. and Shabanov, S. V., "Role of electromagnetic trapped modes in extraordinary transmission in nanostructured materials," *Physical Review B* 71(7), 075408 (2005).
- [135] Jiang, Y. -W., Tzuang, L. D., Ye, Y. -H., Wu, Y. -T., Tsai, M. -W., Chen, C. -Y. and Lee, S. -C., "Effect of Wood's anomalies on the profile of extraordinary transmission spectra through metal periodic arrays of rectangular subwavelength holes with different aspect ratio," *Optics Express* 17(4), 2631-2637 (2009).
- [136] Degiron, A., Lezec, H. J., Yamamoto, N. and Ebbesen, T. W., "Optical transmission properties of a single subwavelength hole in a real metal," *Optics Communications* 239(1-3), 61-66 (2004).
- [137] Hou, B., Hong, Z. H., Wen, W., Chan, C. T. and Sheng, P., "Microwave transmission through metallic hole arrays: surface electric field measurements," *Applied Physics Letters* 89(13), 131917 (2006).
- [138] Tsai, M. -W., Chuang, T. -H., Chang, H. -Y. and Lee, S. -C., "Dispersion of surface plasmon polaritons on silver film with rectangular hole arrays in a square lattice," *Applied Physics Letters* 89(9), 093102 (2006).
- [139] Matsui, T., Agrawal, A., Nahata, A. and Vardeny, Z. V., "Transmission resonances through aperiodic arrays of subwavelength apertures," *Nature* 446, 517-521 (2007).
- [140] Masson, J. -B. and Gallot, G., "Coupling between surface plasmons in subwavelength hole arrays," *Physical Review B* 73(12), 121401(R) (2006).

- [141] Kim, T. J., Thio, T., Ebbesen, T. W., Grupp, D. E. and Lezec, H. J., "Control of optical transmission through metals perforated with subwavelength hole arrays," *Optics Letters* 24(4), 256-258 (1999).
- [142] Thio, T., Ghaemi, H. F., Lezec, H. J., Wolff, P. A. and Ebbesen, T. W., "Surface-plasmon-enhanced transmission through hole arrays in Cr films," *Journal of Optical Society of America B* 16(10), 1743-1748 (1999).
- [143] Azad, A. K., Zhao, Y. and Zhang, W., "Transmission properties of terahertz pulses through an ultrathin subwavelength silicon hole array," *Applied Physics Letters* 86(14), 141102 (2005).
- [144] Degiron, A., Lezec, H. J., Barnes, W. L. and Ebbesen, T. W., "Effects of hole depth on enhanced light transmission through subwavelength hole arrays," *Applied Physics Letters* 81(23), 4327-4329 (2002).
- [145] Roberts, A., Baxter, G. W. and Davis, T. J., "*Nanophotonic resonators: Metamaterials, extraordinary transmission and sensing*", Australian Research Council. Project number DP0878268, (2008).
- [146] Gordon, R., Brolo, A. G., McKinnon, A., Rajora, A., Leathem, B. and Kavanagh, K. L., "Strong polarization in the optical transmission through elliptical nanohole arrays," *Physical Review Letters* 92(3), 037401 (2004).
- [147] Koerkamp, K. J. K., Enoch, S., Segerink, F. B., van Hulst, N. F. and Kuipers, L., "Strong influence of hole shape on extraordinary transmission through periodic arrays of subwavelength holes," *Physical Review Letters* 19(18), 183901 (2004).
- [148] van der Molen, K. L., Klein Koerkamp, K. J., Enoch, S., Segerink, F. B., van Hulst, N. F. and Kuipers, L., "Role of shape and localized resonances

- in extraordinary transmission through periodic arrays of subwavelength holes: experiment and theory," *Physical Review B* 72(4), 045421 (2005).
- [149] Ruan, Z. and Qiu, M., "Enhanced transmission through periodic arrays of subwavelength holes: the role of localized waveguide resonances," *Physical Review Letters* 96(23), 233901 (2006).
- [150] Garcia-Vidal, F. J., Moreno, E., Porto, J. A. and Martin-Moreno, "Transmission of light through a single rectangular hole," *Physical Review Letters* 95(10), 103901 (2005).
- [151] Lee, J. W., Seo, M. A., Kang, D. H., Khim, K. S., Jeoung, S. C. and Kim, D. S., "Terahertz electromagnetic wave transmission through random arrays of single rectangular holes and slits in thin metallic sheets," *Physical Review Letters* 99(13), 137401 (2007).
- [152] Gay, G., de Leseqno, B. V., Mathevet, R., Lezec, H. J. and Weiner, J., "Mapping of angular and spatial optical intensity distributions issuing from nanostructured slits, milled into subwavelength metallic layers," *Journal of Physics: Conference Series* 19, 102-108 (2005).
- [153] Gay, G., Alloschery, O., de Leseqno, B. V., O'Dwyer, C., Weiner, J. and Lezec, H. J., "The optical response of nanostructured surfaces and the composite diffracted evanescent wave model," *Nature Physics* 2, 262-267 (2006).
- [154] Gay, G., Alloschery, O., de Leseqno, B. V., Weiner, J. and Lezec, H. J., "Surface Wave Generation and Propagation on Metallic Subwavelength Structures Measured by Far Field Interferometry," *Physical Review Letters* 96(21), 213901 (2006).
- [155] Kowarz, M. W., "Homogeneous and evanescent contributions in scalar near-field diffraction," *Applied Optics* 34(17), 3055-3063 (1995).

- [156] Genet, C., van Exter, M. P. and Woerdman, J. P., "Huygens description of resonance phenomena in subwavelength hole arrays," *Journal of optical Society of America A* 22(5), 998-1002 (2005).
- [157] Tang, Y., Vlahovic, B. and Brady, D. J., "Metallic nano-structures for polarization independent multi-spectral filters," *Nanoscale Research Letters* 6(1), 394 (2011).
- [158] Prangma, J. C., Oosten, D. v., Moerland, R. J. and Kuipers, L., "Increase of group delay and nonlinear effects with hole shape in subwavelength hole arrays," *New Journal of Physics* 12, 013005 (2010).
- [159] Li, J. Y., Hua, Y. L., Fu, J. X. and Li, Z. Y., "Influence of hole geometry and lattice constant on extraordinary optical transmission through subwavelength hole arrays in metal films," *Journal of Applied Physics* 107, 073101 (2010).
- [160] Xu, J., Wang, J. and Tian, Q., "Non-planar 3D nano-aperture design with strong near-field enhancement," *Journal of the Korean Physical Society* 47, S13-S17 (2005).
- [161] Caglayan, H., Bulu, I. and Ozbay, E., "Extraordinary grating-coupled microwave transmission through a subwavelength annular aperture," *Optics Express* 13(5), 6283 (2005).
- [162] Orbons, S. M. and Roberts, A., "Resonance and extraordinary transmission in annular aperture arrays," *Optics Express* 14(26), 77531 (2006).
- [163] Si, G., Zhao, Y., Liu, H., Teo, S., Zhang, M., Huang, T. J., Danner, A. J. and Teng, J., "Annular aperture array based color filter," *Applied Physics Letters* 99, 033105 (2011).

- [164] Shi, X., Thornton, R. L. and Hesselink, L., "A nano-aperture with 1000× power throughput enhancement for very small aperture laser system " Proceedings of SPIE 4342, 320-327 (2002).
- [165] Sendur, K. and Challener, W. A., "Near-field radiation efficiency of a bow-tie antennas and apertures at optical frequencies," Journal of Microscopy 210, 279-283 (2003).
- [166] Tanaka, K. and Tanaka, M., "Simulation of an aperture in the thick metallic screen that gives high intensity and small spot size using surface plasmon polariton," Journal of Microscopy 210, 294-300 (2003).
- [167] Chen, C. Y., Tsai, M. W., Chuang, T. H., Chang, Y. T. and Lee, S. C., "Extraordinary transmission through a silver film perforated with cross shaped hole arrays in a square lattice," Applied Physics Letters 91, 063108 (2007).
- [168] Lin, L. and Roberts, A., "Angle-robust resonances in cross-shaped aperture arrays," Applied Physics Letters 97, 061109 (2010).
- [169] He, M. D., Liu, J. Q., Gong, Z. Q., Luo, Y. F. and Chen, X., "Light transmission through metal films perforated with arrays of asymmetric cross-shaped hole," Solid State Communications 150, 104-108 (2010).
- [170] Lee, B., Lee, I. M., Kim, S., Oh, D. H. and Hesselink, L., "Review on subwavelength confinement of light with plasmonics," Journal of Modern Optics 57(16), 1479-1497 (2010).
- [171] Garcia-Vidal, F. J., Martin-Moreno, L., Moreno, E., Kumar, L. K. S. and Gordon, R., "Transmission of light through a single rectangular hole in a real metal," Physical Review B 74, 153411 (2006).
- [172] Jin, E. X. and Xu, X., "Finite-difference time-domain studies on optical transmission through planar nano-apertures in a metal film," Japanese Journal of Applied Physics 43(1), 407-417 (2004).

- [173] Wang, H., An, Z., Qu, C., Xiao, S., Zhou, L., Komiyama, S., Lu, W., Shen, X. and K., Chu. P., "Optimization of optoelectronic plasmonic structures " *Plasmonics* 6(2), 319-325 (2011).
- [174] Yanik, A. A., Cetin, A. E., Huang, M., Artar, A., Mousavi, S. H., Khanikaev, A., Connor, J. H., Shvets, G. and Altug, H., "Seeing protein monolayers with naked eye through plasmonic Fano resonances," *Proceedings of the National Academy of Sciences of the USA* 108(29), 11784-11789 (2011).
- [175] Blanchard-Dionne, A-P., Guyot, L., Patskovsky, S., Gordon, R. and Meunier, M., "Intensity based surface plasmon resonance sensor using a nanohole rectangular array," *Optical Society of America* 19(16), 143702 (2011).
- [176] Hu, D. and Zhang, Y., "Localized surface plasmons-based transmission enhancement of terahertz radiation through metal aperture arrays," *Optik* 121, 1423-1426 (2009).
- [177] Kroekenstoel, E. J. A., Verhagen, E., Walters, R. J., Kuipers, L. and Polman, A., "Enhanced spontaneous emission rate in annular plasmonic nanocavities," *Applied Physics Letters* 95, 263106 (2009).
- [178] Yee, K. S., "Numerical solution of initial boundary value problems involving Maxwell's equations in isotropic media," *IEEE Transactions on Antennas and Propagation* 14(3), 302-307 (1966).
- [179] Sullivan, D. M., "A frequency-dependent FDTD method for biological applications," *IEEE Transactions on Microwave Theory and Techniques* 40(3), 532-539 (1992).
- [180] Xiao, S. and Vahldieck, R., "An efficient 2-D FDTD algorithm using real variables," *IEEE Microwave and guided wave letters* 3(5), 127-129 (1993).

- [181] Zivanovic, S. S., Yee, K. S. and Mei, K. K., "A subgridding method for the time-domain finite-difference method to solve Maxwell's equations," *IEEE Transactions on Microwave Theory and Techniques* 39(3), 471-479 (1991).
- [182] Taflove, A., "Application of the finite-difference time-domain method to sinusoidal steady-state electromagnetic-penetration problems," *IEEE Transactions on Electromagnetic Compatibility* 22(3), 191-202 (1980).
- [183] Taflove, A. and Brodwin, M. E., "Numerical solution of steady-state electromagnetic scattering problems using the time-dependent Maxwell's equations," *IEEE Transactions on Microwave Theory and Techniques* 23(8), 623-630 (1975).
- [184] Liu, L., Han, Z. and He, S., "Novel surface plasmon waveguide for high integration," *Optics Express* 13(17), 6645-6650 (2005).
- [185] Feigenbaum, E. and Orenstein, M., "Modeling of complementary (void) plasmon waveguiding," *Journal of lightwave technology* 25(9), 2547-2562 (2007).
- [186] Moreno, E., Rodrigo, S. G., Bozhevolnyi, S. I. and Moreno, L. M., "Guiding and focusing of electromagnetic fields with wedge plasmon polaritons," *Physical Review Letters* 100(2), 023901 (2008).
- [187] Dissanayake, C. M., Premaratne, M., Rukhlenko, I. D. and Agrawal, G. P., "FDTD modeling of anisotropic nonlinear optical phenomena in silicon waveguides," *Optics Express* 18 20(20), 21427-21448 (2010).
- [188] Poh, C. -H., Rosa, L., Juodkazis, S. and Dastoor, P., "FDTD modeling to enhance the performance of an organic solar cell embedded with gold nanoparticles," *Optical Materials Express* 1(7), 1326-1331 (2011).
- [189] Khankhoje, U. K., Kim, S. -H., Richards, B. C., Hendrickson, J., Sweet, J., Olitzky, J. D., Khitrova, G., Gibbs, H. M. and Scherer, A., "Modelling

and fabrication of GaAs photonic-crystal cavities for cavity quantum electrodynamics," *Nanotechnology* 21(6), 065202 (2010).

- [190] Taflove, A. and Hagness, S. C., [Computational electrodynamics: The finite-difference time-domain method], Norwood, MA, (2000).
- [191] Kunz, K. S. and Luebbers, R. J., [The finite difference time domain method for electromagnetics], CRC Press(1993).
- [192] Elsherbeni, A. Z. and Demir, V., [The Finite Difference Time Domain Method for Electromagnetics: With MATLAB Simulations], SciTech, Raleigh, NC, (2009).
- [193] <http://www.lumerical.com>.
- [194] Pepper, D. W. and Heinrich, J. C., [The finite element method: basic concepts and applications], Taylor & Francis(1992).
- [195] Zimmerman, W., [Multiphysics modeling with finite element methods], World Scientific Publishing(2006).
- [196] Yang, X., [A first course in finite element analysis], Luniver Press(2007).
- [197] Argyris, J. and Kelsey, S., [Energy theorems and structural analysis], Butterworth, London, (1960).
- [198] Turner, M. J., Clough, R. W., Martin, H. C. and Topp, L. J., "Stiffness and deflection analysis of complex structures," *Aeronautical Sciences* 23(9), 805-824 (1956).
- [199] Reddy, J. N., [An introduction to the finite element method (2nd Edn)], McGrawHill, New York, (1993).
- [200] <http://www.comsol.com>.
- [201] McMahon, J. M., Henzie, J., Odom, T. W., Schatz, G. C. and Gray, S. K., "Tailoring the sensing capabilities of nanohole arrays in gold films with

- Rayleigh anomaly-surface plasmon polaritons," *Optics Express* 15(26), 18119-18129 (2007).
- [202] Dhawan, A., Muth, J. F., Leonard, D. N., Gerhold, M. D., Gleeson, J., Vo-Dinh, T. and Russell, P. E., "Focused ion beam fabrication of metallic nanostructures on end faces of optical fibers for chemical sensing applications," *Journal of Vacuum Science and Technology B: Microelectronics and Nanometer Structures* 26(6), 2168-2173 (2008).
- [203] Russell, P. E., Dhawan, A. and Gleeson, J., "FIB fabrication of metallic nanostructures on end-faces of cleaved optical fibers for chemical sensing applications," *Microscopy and Microanalysis* 14, 988-989 (2008).
- [204] Okamoto, T., "Near-field spectral analysis of metallic beads," in *Near-field optics and surface plasmon polaritons*, Vol. 81 of *Topics in applied physics*, S. Kawata, M. Ohtsu, and M. Irie eds. Springer New York, 97-123 (2001).
- [205] Henzie, J., Lee, M. H. and Odom, T. W., "Multiscale patterning of plasmonic metamaterials," *Nature Nanotechnology* 2, 549-554 (2007).
- [206] <http://www.thermionics.com>.
- [207] <http://www.fei.com/>.
- [208] Volkert, C. A. and Minor, A. M., "Focused ion beam microscopy and micromachining," *MRS Bulletin* 32(5), 389-395 (2007).
- [209] Company, FEI, "xT Nova NanoLab User's Manual," pp 5-8 (2007).
- [210] Morgan, M. D., Horne, W. E. and Sundaram, V., "Application of optical filters fabricated by masked ion beam lithography," *Journal of Vacuum Science and Technology B* 14(6), 3903-3906 (1996).
- [211] Cui, B., "Ultrafast fabrication of metal nanostructures using pulsed laser melting," Chapter in *Lithography*, Intech(2011).

- [212] Chu, K.-H., Xiao, R. and Wang, E. N., "Uni-directional liquid spreading on asymmetric nanostructured surfaces," *Nature Materials* 9(5), 413-417 (2010).
- [213] Zhou, M., Li, J., Yan, F., Fan, X. and Cai, L., "A Facile "Air-Molding" Method for Nanofabrication," *Langmuir* 16(18), 14889-14893 (2010).
- [214] Huang, M., Yanik, A. A., Chang, T.-Y. and Altug, H., "Sub-wavelength nanofluidics in photonic crystal sensors," *Optical Society of America* 17(26), 24224-24233 (2009).
- [215] Chanda, D., Shigeta, K., Truong, T., Liu, E., Mihi, A., Schulmerich, M., Braun, P. V., Bhargava, R. and Rogers, J. A., "Coupling of plasmonic and optical cavity modes in quasi-three-dimensional plasmonic crystals," *Nature Communications* 2, 1-7 (2011).
- [216] Juan, M. L., Righini, M. and Quidant, R., "Plasmon nano-optical tweezers," *Nature Photonics* 5, 349-356 (2011).
- [217] Liu, N., Tang, M. L., Hentschel, M., Giessen, H. and Alivisatos, A. P., "Nanoantenna-enhanced gas sensing in a single tailored nanofocus," *Nature Materials* 10, 631-631 (2011).